

Copyright is owned by the Author of the thesis. Permission is given for a copy to be downloaded by an individual for the purpose of research and private study only. The thesis may not be reproduced elsewhere without the permission of the Author.

# **Hybrid Organic-Inorganic Layered Electronic Materials**

A thesis presented in partial fulfilment of the requirements for the degree of

**Doctor of Philosophy**

**in**

**Physics**

at Massey University, Manawatu Campus

New Zealand.

**Islah-u-din**

**2012**

## Abstract

Hybrid organic-inorganic materials combine distinct features of organic and inorganic components into single molecular frameworks that exhibit tunable electronic, optical and magnetic properties. An extending layered network is formed by covalently bound layers of inorganic materials that are electronically coupled by organic components. A control on the stacking orientation of these layers can help tailor the structural, physical and chemical properties of resulting compounds.

This thesis presents an investigation of the synthesis, characterization and effects of doping, primarily by ion-implantation, on structural, chemical and physical properties of transition-metal oxide based organic-inorganic hybrid materials. These materials were synthesized and characterized by a variety of experimental techniques. The crystal structures of these compounds were probed by powder and single-crystal X-ray diffraction while various other techniques such as Raman spectroscopy, X-ray photoelectron spectroscopy, magnetic and resistivity measurements were applied to examine the chemical and physical properties of these materials. The crystal structure of these materials consists of infinite layers of transition metal oxides interlinked by organic ligands. The organic-ligands are aligned so as to define small cages within these structures, potentially, to accommodate metal ions. Intercalation of alkali-metal atoms within these cages brings about important alterations in the structural, chemical and physical properties of these materials. The presence of intercalated species was confirmed by single-crystal X-ray diffraction and X-ray photoelectron spectroscopy while spectral changes observed from Raman measurements and a significant reduction in electrical resistance of implanted materials refer to charge carrier-injection into the conduction band.

Significant changes in structure and physical properties of these materials were observed by increasing the number of atoms in ligand tethers while introduction of additional metal atoms, by in-situ doping, in the inorganic oxide layers, leads to strong antiferromagnetic interactions in otherwise diamagnetic materials. These results demonstrate the possibilities of exploiting the self-assembly of organic and inorganic precursors to realize the potential applications these materials have to offer.

## Preface

Some of the results described in this thesis have been published in the following international journal articles. Few other articles are in preparation.

1. Islah-u-din, S. V. Chong, S. G. Telfer, J. Kennedy, G. B. Jameson, M. R. Waterland and J. L. Tallon, “Influence of Doping on Hybrid Organic-Inorganic  $\text{WO}_3(4,4'$ -bipyridyl) $_{0.5}$ Materials”, *The Journal of Physical Chemistry C*, 2012, 116, 3787-3792.
2. Islah-u-din, M. R. Fox, H. Martin, G. J. Gainsford, J. Kennedy, A. Markwitz, S. G. Telfer, G. B. Jameson and J. L. Tallon, “Synthesis and Structure of  $\text{Na}^+$ -intercalated  $\text{WO}_3(4,4'$ -bipyridyl) $_{0.5}$ ”, *Chemical Communications*, 2010, 46, 4261-4263.

These results were also presented at the following conferences

1. 2<sup>nd</sup> International Advances in Applied Physics and Materials Science, Antalya, Turkey, April 26 – 29, 2012. [Oral presentation]
2. JAIST International School on Emerging Nanotechnologies, Kanazawa, Japan, March 26 – 29, 2012. [Poster presentation]
3. New Zealand Institute of Physics Conference, Wellington, New Zealand, October 17 – 19, 2011. [Oral presentation]
4. Hybrid Materials: 2<sup>nd</sup> International Conference on Multifunctional, Hybrid and Nanomaterials, Strasbourg, France, March 6 – 10, 2011. [Poster presentation]

## **Acknowledgements**

I must thank my supervisors Dr. Mark R. Waterland, Dr. Shane G. Telfer and Dr. Jeffery L. Tallon for all their support and guidance towards completion of this study.

I am very grateful to Prof. Geoffrey B. Jameson for his untiring efforts in teaching me X-ray crystallography and for all his help in solving very complex crystal structures. Despite his very busy schedule he has always been very kind to spare time for thoughtful discussions on different aspects of this project. I really appreciate his cooperation.

Thanks a lot to Dr. Shen V. Chong (Industrial Research Ltd.) for his help with so many experiments, especially for doing magnetic measurements.

Many thanks to Dr. John V. Kennedy and Dr. Vivian Fang (GNS Science, Lower Hutt) for organising ion-implantation experiments.

I am indebted to Higher Education Commission, Pakistan for providing me a doctoral scholarship to study in New Zealand. I would never have imagined doing a PhD without this scholarship. I am also very thankful to MacDiarmid Institute of Nanotechnology for providing partial financial support and access to numerous experimental facilities across the New Zealand. Many Thanks to Institute of Fundamental Sciences for providing financial support towards conference travel.

A big thanks to Pakistani community in Palmerston North, especially Dr. Zulfiqar H. Butt for their support during last five years. Many thanks to all my friends and well wishers for their great company.

Finally, I am very thankful to all my family who have to live all these years without me.

# Contents

<b>Abstract</b> .....	ii
<b>Preface</b> .....	iii
<b>Acknowledgements</b> .....	iv
<b>Contents</b> .....	v
<b>List of Figures</b> .....	viii
<b>List of Tables</b> .....	xvi
<b>1 Introduction</b> .....	1
1.1 Electron Physics in Correlated Oxide Systems.....	2
1.1.1 Jahn-Teller Effect.....	4
1.1.2 Mott Insulators .....	5
1.1.3 Colossal Magnetoresistance.....	6
1.1.4 High Temperature Superconductivity.....	7
1.2 Hybrid Organic-Inorganic Layered Electronic Materials .....	10
1.2.1 Definition: Hybrid Materials.....	10
1.2.2 Origins of Hybrid Materials.....	11
1.2.3 Properties and Applications of Hybrid Materials .....	13
1.2.4. Classification of Hybrid Materials.....	19
1.3 Aims and objectives.....	27
<b>2 Experimental Techniques</b> .....	29
2.1 Hydrothermal Synthesis.....	29
2.2 Ion-Implantation .....	31
2.2.1 Ion Implantation Process.....	32
2.2.2 Ion-Implantation Applications .....	35
2.3 Characterization Techniques.....	36
2.3.1 X-ray Diffraction .....	36

2.3.2 X-ray Photoelectron Spectroscopy .....	41
2.3.3 Raman Spectroscopy.....	44
2.3.4. Magnetic Measurements .....	47
<b>3 Synthesis, structure and physical properties of Na<sup>+</sup> -intercalated WO<sub>3</sub> (4,4'-bipyridyl)<sub>0.5</sub> hybrid material .....</b>	<b>50</b>
3.1 Introduction.....	50
3.2 Experimental Details.....	52
3.2.1 Synthesis .....	52
3.2.2 Ion-Implantation .....	53
3.2.3 Characterization .....	53
3.3 X-ray Diffraction .....	54
3.4 Magnetic Measurements .....	63
3.5 Raman Measurements.....	65
3.6 Summary .....	69
<b>4 Influence of doping on hybrid organic-inorganic WO<sub>3</sub>(4, 4'-bipyridyl)<sub>0.5</sub> materials .....</b>	<b>71</b>
4.1 Introduction.....	71
4.2 Experimental Details.....	72
4.2.1 Synthesis .....	72
4.2.2 Ion-Implantation .....	75
4.2.3 Characterization .....	75
4.3 Thick-film structure .....	76
4.4 Single-crystal X-ray Diffraction Studies .....	79
4.5 Raman Spectroscopy.....	82
4.6 X-Ray Photoelectron Spectroscopy .....	84
4.7 Resistivity Measurements .....	88
4.8 Summary .....	89

<b>5 Synthesis and characterization of novel single and bimetallic layered organic-inorganic hybrid materials</b> .....	90
5.1 Introduction.....	90
5.2 Experimental Details.....	92
5.2.1 Synthesis .....	92
5.2.2 Characterization .....	93
5.3 Single Crystal X-ray Diffraction.....	93
5.3.1 WO <sub>3</sub> -phen and MoO <sub>3</sub> -phen.....	93
5.3.2 CuMoO <sub>4</sub> -phen.....	97
5.3.3 Cu <sub>3</sub> Cr <sub>2</sub> O <sub>10</sub> -phen.....	99
5.4 Powder X-ray Diffraction .....	103
5.5 Raman Spectroscopy.....	106
5.6 Magnetic Measurements .....	111
5.7 Summary .....	114
<b>6 Summary and Future Directions</b> .....	115
6.1 Summary .....	115
6.2 Future prospects.....	118
<b>A Bond Valence Sum Calculations</b> .....	120
<b>B Unsuccessful Synthesis</b> .....	124
<b>C X-ray Crystal Structure Data</b> .....	136
<b>References</b> .....	137

## List of Figures

<b>Figure 1.1</b> (a) Octahedral representation of transition metal oxide. (b) Different orientations for 3d orbitals in transition metal oxides where fivefold degeneracy is lifted to two $e_g$ [ $(x^2 - y^2)$ and $(z^2)$ ] orbitals and three $t_{2g}$ orbitals [(xy), (yz), and (zx)]. (c) Crystal field splitting. ....	4
<b>Figure 1.2</b> Silicic skeleton of a diatom, showing complex and finely carved morphology in scanning electron microscopy.....	12
<b>Figure 1.3</b> Computer enhanced Mayan warrior from Bonampak. ....	12
<b>Figure 1.4</b> Organic-inorganic hybrid materials containing organic chromophores. ....	15
<b>Figure 1.5</b> (a) A core-shell silica microcapsule for carrying potent chemicals. (b) Commercial Sunscreen SPF 20.....	16
<b>Figure 1.6</b> Artificial hydrophobic coatings inspired by lily leaves.....	17
<b>Figure 1.7</b> (a) High quality optical appearance of crystal glass. (b) Easy to recycle coloured glass bottles coated with hybrid organic-inorganic materials.....	17
<b>Figure 1.8</b> ORMOCER waveguides where the hybrid coating is deposited on a flexible foil	18
<b>Figure 1.9</b> (a) Pentium MCM-L/D manufactured in ORMOCER. (b) Electro-optical o/e MCM manufactured in ORMOCER.....	18
<b>Figure 1.10</b> Layered structure of manganese phosphite stacking along <i>c</i> -axis with alkyldiammonium ions filling the interlayer space.....	20
<b>Figure 1.11</b> A layered perovskite material.....	20
<b>Figure 1.12</b> Layered structure of $KCa_2Nb_3O_{10}$ where Ca atoms (small circles) occupy the interlayer space formed by corner shared $NbO_6$ octahedra. ....	21
<b>Figure 1.13</b> Octahedral symmetries as demonstrated by perovskite tungsten bronze unit cell. ....	22

<b>Figure 1.14</b> Tungsten oxide octahedra arranged in corner-sharing configuration to form monoclinic $\text{WO}_3$ (above) and two layers of octahedral tungsten oxide stacked so as to reveal vacant tunnels along the z-direction (below). .....	23
<b>Figure 1.15</b> Edge-sharing arrangement of $\text{WO}_6$ octahedra leads to formation of substiochiometric $\text{WO}_{3-x}$ . .....	24
<b>Figure 1.16</b> Crystal structure of $[[\text{Ni}(2,2'\text{-bipyridyl})_2]_2\text{Mo}_4\text{O}_{14}]$ . .....	26
<b>Figure 2.1</b> A stainless steel Teflon-lined autoclave used for synthesizing hybrid materials. 30	
<b>Figure 2.2</b> Schematics of a typical ion-implanter. ....	33
<b>Figure 2.3</b> A low energy ion-implanter at GNS Sciences, Lower Hutt was used for doping metal atoms into single crystals and thick films. ....	35
<b>Figure 2.4</b> A simplified sketch of the X-ray diffractometer. ....	37
<b>Figure 2.5</b> A pictorial illustration of Bragg's law. ....	37
<b>Figure 2.6</b> The Rigaku spider diffractometer at Massey University, Palmerston North that was used for structural characterization of crystalline materials. ....	39
<b>Figure 2.7</b> A powder X-ray diffractometer at Industrial Research, Lower Hutt was used for preliminary structural characterization of polycrystalline hybrid materials. ....	41
<b>Figure 2.8</b> An explanation of basic principle of XPS. ....	42
<b>Figure 2.9</b> The Kratos Axis UltraDLD surface-analyzing chamber at the University of Auckland that was used for XPS measurements. ....	43
<b>Figure 2.10</b> Different light scattering techniques. ....	44
<b>Figure 2.11</b> The LabRam instrument at Victoria University, Wellington was used for solid-state Raman measurements. ....	46
<b>Figure 2.12</b> A simplified schematic representation of DC SQUID operation. Green stripes represent Josephson junctions. ....	47

<b>Figure 2.13</b> A Quantum Design MPMS XL SQUID at Industrial Research Ltd. was used for magnetic characterization. ....	49
<b>Figure 3.1</b> Crystal structure of WO <sub>3</sub> -bpy. <sup>71</sup> Layers of corner-shared tungsten oxide octahedra are bridged by bpy ligands defining open structure channels. Tungsten atoms are shown in green, oxygen in red, nitrogen in blue and carbon in grey. Hydrogen atoms are omitted for clarity. ( <i>c</i> -axis is horizontal). ....	51
<b>Figure 3.2</b> Polymer bound thick film of WO <sub>3</sub> -bpy coated on ITO glass substrate. ....	53
<b>Figure 3.3</b> A high-resolution snapshot of WO <sub>3</sub> bpy single crystal before (left) and after (right) Na <sup>+</sup> ion-implantation. ....	54
<b>Figure 3.4</b> Powder XRD patterns demonstrate strong <i>00l</i> reflections which indicate the formation of layered structures for both forms of WO <sub>3</sub> -bpy: black = pattern calculated from single-crystal XRD, red = experimental pattern of WO <sub>3</sub> -bpy. The diffraction angle is for Co K $\alpha$ radiation. For comparison, the wavelength was changed to Co K $\alpha$ in the pattern calculated from single crystal structure of WO <sub>3</sub> -bpy, which was determined with Cu K $\alpha$ radiation. Intensity is measured in arbitrary units and Bragg angle in degrees. ....	55
<b>Figure 3.5</b> A comparison of XRD patterns obtained from WO <sub>3</sub> -bpy pellets annealed at different temperatures. A notable decrease in intensity of all the peaks is observable as temperature increases. Beyond 460 °C, this decrease in intensity becomes significant with a clear broadening in (006) and (0012) peaks suggesting the disintegration of layered structure. Intensity is measured in arbitrary units and Bragg angle in degrees. ....	56
<b>Figure 3.6</b> A comparison of XRD patterns obtained from WO <sub>3</sub> -bpy polymer bound films before and after ion-implantation. Intensity is measured in arbitrary units and Bragg angle in degrees. ....	57
<b>Figure 3.7</b> Structural repeat unit for Na <sub>x</sub> WO <sub>3</sub> -bpy showing two WO <sub>5</sub> N octahedra linked via the nitrogens on the bpy. Tungsten atoms are shown in green, oxygens in red, nitrogens in blue, carbons in grey and hydrogens in white. ( <i>c</i> -axis is horizontal). Graphics using MERCURY. ....	60

<b>Figure 3.8</b> The crystal structure of $\text{WO}_3$ -bpy consists of layers of corner-shared octahedral tungsten oxide bridged by bpy ligands. The colour scheme is similar to Fig. 3.7. ( <i>c</i> -axis is horizontal).Graphics using DSViewPro.....	60
<b>Figure 3.9</b> (a) Structural repeat unit for $\text{Na}_x\text{WO}_3$ -bpy showing two $\text{WO}_5\text{N}$ octahedra linked via the nitrogens (blue) on the bpy. The intercalated $\text{Na}^+$ ions (yellow) are bimodally located in the cage bounded along the <i>c</i> -axis by the axial oxygens (red), as depicted in (b). A cage structure is formed by the alternating alignment of the bpy planes. The display style is changed in (b) for convenience. The colour scheme is the same for both. ( <i>c</i> -axis is horizontal.) Graphics using MERCURY. ....	61
<b>Figure 3.10</b> The crystallographic structure of $\text{Na}_x\text{WO}_3$ -bpy showing the inorganic $\text{WO}_3\text{N}$ framework layers and one organic cage housing the $\text{Na}^+$ intercalant. Atoms are coloured as in Fig. 3.7. (Graphics using PLATON and POV-RAY). ....	62
<b>Figure 3.11</b> ZFC magnetic measurements of $\text{WO}_3$ -bpy films measured at $2 \times 10^{-4}$ Tesla. ....	64
<b>Figure 3.12</b> Temperature-dependence of ZFC magnetic moment for unimplanted and $\text{Na}^+$ -implanted polymer-bound $\text{WO}_3$ -bpy films. ....	65
<b>Figure 3.13</b> Raman spectra of pure $\text{Na}_2\text{WO}_4 \cdot 2\text{H}_2\text{O}$ . Intensity is measured in arbitrary units. ....	66
<b>Figure 3.14</b> Raman spectra of pure bpy. Data was collected over two spectral windows ( $330\text{--}1050 \text{ cm}^{-1}$ to $1050\text{--}1800 \text{ cm}^{-1}$ ). Intensity is measured in arbitrary units. ....	66
<b>Figure 3.15</b> Raman spectra of powdered $\text{WO}_3$ -bpy. Intensity is measured in arbitrary units. ....	68
<b>Figure 3.16</b> Raman spectra of doped and undoped polymer bound films. Intensity is measured in arbitrary units.....	69
<b>Figure 4.1</b> A possible structural model for multilayer thin films of $\text{WO}_3$ -bpy. ....	73
<b>Figure 4.2</b> A simplified sketch of modified layer-by-layer scheme for deposition of $\text{WO}_3$ -bpy on ITO. ....	74
<b>Figure 4.3</b> An SEM image of $\text{WO}_3$ -bpy coated ITO using SEM reveals the formation of intergrown microcrystals. ....	76

**Figure 4.4** Powder X-ray diffractograms of WO<sub>3</sub>-bpy. The diffraction angle is for Co K $\alpha$  radiation. Evidence for the same layered structure for all the forms of WO<sub>3</sub>-bpy: black = pattern calculated from the single-crystal structure, red = experimental pattern of bulk WO<sub>3</sub>-bpy, blue = experimental pattern of ITO-bound WO<sub>3</sub>-bpy. For comparison, wavelength was changed to Co K $\alpha$  in the pattern calculated from single crystal structure of WO<sub>3</sub>-bpy, which was determined with Cu K $\alpha$  radiation. Intensity is measured in arbitrary units and Bragg angle in degrees.....77

**Figure 4.5** A comparison of powder XRD patterns obtained from WO<sub>3</sub>-bpy films before and after ion-implantation. Intensities were enlarged in both figures. The diffraction wavelength is of Co K $\alpha$ . Intensity is measured in arbitrary units and Bragg angle in degrees..... 78

**Figure 4.6** A comparison of powder XRD patterns calculated from single crystal XRD measurements of WO<sub>3</sub>-bpy materials before and after ion-implantation. The diffraction wavelength is of Cu K $\alpha$ . Intensity is measured in arbitrary units and Bragg angle in degrees. .... 78

**Figure 4.7** Crystal structures of WO<sub>3</sub>-bpy before (left) and after implantation (centre, Ca<sup>2+</sup> and right, K<sup>+</sup>). Tungsten atoms are shown in green, oxygens in red, nitrogens in blue. Yellow colour represents the sites attributed to implantation of Ca<sup>2+</sup> (centre) and K<sup>+</sup> (right) ions. Like Na<sup>+</sup>, Ca<sup>2+</sup> resides disordered over two sites away from the inversion centre in the centre of the cage, while K<sup>+</sup> resides at the cage centre on a crystallographic centre of inversion. Graphics using PLATON and POV-RAY..... 80

**Figure 4.8** Raman spectra of WO<sub>3</sub>-bpy before and after ion-implantation. (a) Bulk crystalline WO<sub>3</sub>-bpy material, (b) WO<sub>3</sub>-bpy film before implantation, (c) Na<sup>+</sup>-implanted WO<sub>3</sub>-bpy film, (d) Ca<sup>2+</sup>-implanted WO<sub>3</sub>-bpy film (e) K<sup>+</sup>-implanted WO<sub>3</sub>-bpy film. .... 82

**Figure 4.9** XPS scans of WO<sub>3</sub>-bpy films before and after ion-implantation. .... 86

**Figure 4.10** Deconvolution of XPS peaks C 1s (left) and O 1s (right) for non-implanted and implanted thick films of WO<sub>3</sub>-bpy..... 86

**Figure 4.11** Evolution of the W 4f XPS peaks upon ion-implantation. The arrows indicate the position of tungstate species with respect to the W 4f<sub>7/2</sub> peak. .... 87

<b>Figure 4.12</b> Intercalated species were detected by XPS for Ca 2 <i>p</i> , K 2 <i>p</i> and Na 1 <i>s</i> in ion-implanted WO <sub>3</sub> -bpy films. ....	87
<b>Figure 4.13</b> Temperature dependence of the resistance of WO <sub>3</sub> -bpy films before and after Ca <sup>2+</sup> implantation. The inset shows the corresponding V-I curves measured at room temperature. The displayed resistances are calculated from dotted lines in the respective V-I curves. ....	89
<b>Figure 5.1</b> A comparison of 1,10-phenanthroline (left) and 3,8-phenanthroline (right) structures. ....	91
<b>Figure 5.2</b> Crystal repeat unit for MO <sub>3</sub> -phen (where M = W or Mo). O <sub>2</sub> and O <sub>3</sub> have 50% occupancy for both structures making metal-oxide ratio to 1:3. Hydrogen atoms are omitted for clarity. ....	93
<b>Figure 5.3</b> A comparison of ligand-packing for WO <sub>3</sub> -bpy (left) and WO <sub>3</sub> -phen (right) structures. It can be noted that the cavity between apical oxygens is much smaller for WO <sub>3</sub> -phen as compared to that of WO <sub>3</sub> -bpy. Colour scheme is similar to Fig.5.2. ....	96
<b>Figure 5.4</b> Crystal structure of CuMoO <sub>4</sub> -phen. A structural motif (left) and a complete structure (right) is generated by bimetallic layers of edge-shared copper oxide octahedra and corner shared molybdenum oxide tetrahedra in the <i>ab</i> -plane while ligands interconnect the inorganic layers to form a 3D covalent framework. Hydrogen atoms are omitted for clarity. Copper is displayed in cyan, molybdenum in pink, oxygen in red, nitrogen in blue and carbon in grey. ....	97
<b>Figure 5.5</b> Coordination geometries for Mo (left) and Cu (right) sites. Both Cu(3) and Cu(4) have similar six coordination. Although both Mo(1) and Mo(2) are four coordinated, the coordination at Mo(1) is defined by four bridging oxo while for Mo(2) it is composed of three bridging oxo and a terminal group. Colour scheme similar to Fig. 5.4. ....	98
<b>Figure 5.6</b> Crystal repeat unit of Cu <sub>3</sub> Cr <sub>2</sub> O <sub>10</sub> -phen (left) and complete structure (right). Colour scheme is same in both figures. Hydrogens and disordered carbon atoms are removed from right side figure for clarity. ....	99

<b>Figure 5.7</b> A metal-oxide inorganic layer of $\text{Cu}_3\text{Cr}_2\text{O}_{10}$ -phen demonstrating coordination geometries of the three metal ion sites.....	101
<b>Figure 5.8</b> Powder X-ray diffractograms for $\text{WO}_3$ -phen, $\text{MoO}_3$ -phen, $\text{CuMoO}_4$ -phen and $\text{Cu}_3\text{Cr}_2\text{O}_{10}$ -phen. The diffraction angle is for Co $K\alpha$ radiation. The intensities were scaled in both figures for better comparison. Intensity is measured in arbitrary units and Bragg angle in degrees. ....	104
<b>Figure 5.9</b> A comparison of experimental and calculated powder X-ray patterns for $\text{WO}_3$ -phen. For comparison, the wavelength was changed to Co $K\alpha$ in the pattern calculated from the single crystal structure of $\text{WO}_3$ -phen, which was determined with Cu $K\alpha$ radiation. Intensity is measured in arbitrary units and Bragg angle in degrees. ....	104
<b>Figure 5.10</b> A comparison of experimental and calculated powder X-ray patterns for $\text{MoO}_3$ -phen. For comparison, the wavelength was changed to Co $K\alpha$ in the pattern calculated from the single crystal structure of $\text{MoO}_3$ -phen, which was determined with Cu $K\alpha$ radiation. Intensity is measured in arbitrary units and Bragg angle in degrees. ....	105
<b>Figure 5.11</b> A comparison of experimental and calculated powder X-ray patterns for $\text{CuMoO}_4$ -phen. For comparison, the wavelength was changed to Co $K\alpha$ in the pattern calculated from the single crystal structure of $\text{CuMoO}_4$ -phen, which was determined with Cu $K\alpha$ radiation. Intensity is measured in arbitrary units and Bragg angle in degrees. ....	105
<b>Figure 5.12</b> A comparison of experimental and calculated powder X-ray patterns for $\text{Cu}_3\text{Cr}_2\text{O}_{10}$ -phen. For comparison, the wavelength was changed to Co $K\alpha$ in the pattern calculated from the single crystal structure of $\text{Cu}_3\text{Cr}_2\text{O}_{10}$ -phen, which was determined with Cu $K\alpha$ radiation. Intensity is measured in arbitrary units and Bragg angle in degrees. ....	106
<b>Figure 5.13</b> A comparison of Raman spectra of $\text{WO}_3$ -phen and $\text{WO}_3$ -bpy. Intensity is measured in arbitrary units.....	107
<b>Figure 5.14</b> Experimental and calculated Raman spectra of 1,10-phenanthroline. Experimental spectrum was recorded in solid state with 633 nm excitation. Intensity is measured in arbitrary units.....	108
<b>Figure 5.15</b> Theoretical spectrum of phen calculated using Gaussian09. Figure was generated using GaussView 5. Intensity is measured in arbitrary units.....	108

<b>Figure 5.16</b> Raman spectra of MoO <sub>3</sub> -phen and MoO <sub>3</sub> -bpy. Intensity is measured in arbitrary units.....	109
<b>Figure 5.17</b> A comparison of Raman spectra obtained from CuMoO <sub>4</sub> , CuMoO <sub>4</sub> -bpy and CuMoO <sub>4</sub> -phen. Despite the different nature of ligands, the position of 929 cm <sup>-1</sup> remains unchanged in all three compounds which reflects the strong influence of terminal oxo groups. Intensity is measured in arbitrary units. ....	110
<b>Figure 5.18</b> Temperature-dependent volume susceptibility measurements recorded at different applied fields for WO <sub>3</sub> -phen (left) and MoO <sub>3</sub> -phen (right). ....	112
<b>Figure 5.19</b> Volume magnetic susceptibility of CuMoO <sub>4</sub> -phen measured at different applied fields.....	113
<b>Figure 5.20</b> Curie-Weiss Fitting to high-temperature susceptibility data of CuMoO <sub>4</sub> -phen. ....	113
<b>Figure 5.21</b> Temperature-dependent $\chi T$ plots for CuMoO <sub>4</sub> -phen recorded at different applied fields.....	114

## List of Tables

<b>Table 3.1</b> Selected X-ray crystallography details for WO <sub>3</sub> -bpy.....	59
<b>Table 4.1</b> Selected single-crystal X-ray diffraction data collection and refinement details of implanted and non-implanted WO <sub>3</sub> -bpy . .....	81
<b>Table 5.1</b> Selected crystallographic and refinement details for WO <sub>3</sub> -phen and MoO <sub>3</sub> -phen hybrids.....	95
<b>Table 5.2</b> Selected crystallographic and refinement details for CuMoO <sub>4</sub> -phen and Cu <sub>3</sub> Cr <sub>2</sub> O <sub>10</sub> -phen hybrids.....	102
<b>Table A1:</b> Selected Cu(2)–O bond distances. Mathematical transformations used to generate symmetrically equivalent atoms: $g = 1-x,-y,-z$ .....	121
<b>Table A2:</b> Selected Cu(1)–O bond distances. Mathematical transformations used to generate symmetrically equivalent atoms: $a = -1+x,y,z$ ; $b = -1+x,1+y,-1+z$ ; $e = -x,-y,-z$ . .....	122
<b>Table A3:</b> Selected Cr(3)–O bond distances.....	123
<b>Table B1</b> Details of unsuccessful synthesis. ....	125

# Chapter 1

## Introduction

The continuous demand for smart materials and a race towards more and more reduction in device size have triggered a great amount of interest in synthesis of materials with unique properties. Hybrid organic-inorganic materials represent an alternative to present materials as they promise improved properties by combining organic and inorganic components together. This thesis describes the synthesis and characterization of novel hybrid organic-inorganic layered electronic materials and the influence of doping, primarily by ion-implantation on their structural, chemical and physical properties. These hybrids have pillared layered structures which consist of infinite layers of transition metal oxides electronically coupled with organic ligands thus defining cages, potentially to accommodate metal ions. Synthesis of novel organic-inorganic layered electronic hybrid materials, their characterization and effect of ion-implantation on structural, chemical and physical properties of these hybrid materials will be discussed in detail.

The first chapter discusses some basic physics behind the functional properties exhibited by correlated oxide systems. In section two, recent progress in the broad field of hybrid organic-inorganic materials is reviewed with some discussion on different methods to synthesize these materials. Aims and objectives of the present work are laid out in section three.

Chapter two describes underlying principles of experimental techniques that were used during the course of this study. Section one describes the details of a synthetic method for preparing crystalline hybrid materials. The second section contains the necessary details from ion-implantation of the hybrids and the experimental techniques used to characterize these materials are discussed in the final section.

Synthesis and detailed structural analysis of  $\text{WO}_3(4,4'\text{-bipyridyl})_{0.5}$  is described in chapter three. The influence of  $\text{Na}^+$ -ion implantation on the structure of these materials will also be discussed in detail. Moreover, the fabrication of polymer bound-films and their characterization before and after ion-implantation are also discussed.

Chapter four describes the influence of implanting the  $\text{WO}_3(4,4'\text{-bipyridyl})_{0.5}$  with  $\text{Ca}^{2+}$  and  $\text{K}^+$  ions. A novel method for fabricating thick polycrystalline films of these hybrids has been developed to study the physical properties of these materials. After establishing the structural correlations between the crystalline material and thick films, in-depth characterization of surface-bound materials before and after ion-implantation have been performed.

Chapter five covers the synthesis and structural analysis of some other novel single and double-layer hybrids. Physical properties of these materials are examined by magnetic and Raman measurements.

Finally, conclusions and some ideas for future work are presented in chapter six.

## **1.1 Electron Physics in Correlated Oxide Systems**

According to wave-particle theory, an electron, like any other quantum particle, exhibits both wave-like and particle-like characteristics. However, it is the interaction of an electron with its neighbours that determines the dominating aspect of this wave-particle duality at a particular instance. For example, the Bloch Theorem states that an electron placed in a periodic lattice behaves like an extended plane wave. However, when the number of free electrons in a solid becomes comparable to the number of the constituent atoms and the mutual electron-electron interaction becomes strong, electrons may lose their mobility and their behaviour can no longer be described in terms of non-interacting entities. Such systems are known as strongly-correlated systems. Most, if not all, transition metal oxides belong to such a class where electron interactions strongly determine the electronic properties and the dual nature of electrons becomes most apparent. Typically, such transition-metal oxides have partially filled *d*-electron shells and are expected to be good conductors while strong Coulomb repulsion (a “correlation effect”) tends to localize individual electrons at atomic lattice sites thus favouring an insulating state. Thus the electronic structures of these materials are neither free-electron-like nor simply ionic but somehow intermediate. This subtle balance between two states makes many of the transition-metal oxides excellent resources for studying and exploiting the metal-insulator transition with often accompanying dramatic changes in the system’s electronic properties.<sup>1</sup>

There exists no unified theory for interpreting the electronic structure of transition metal oxides, however a basic understanding can be obtained by studying the interaction between three fundamental attributes (charge (-e), spin ( $\pm 1/2$ ), and orbital symmetry) that determine the behaviour of electrons when they are bound to atomic nuclei by attractive Coulomb forces. An orbital represents the electron's probability-density distribution and can be imagined as the shape of an electron cloud in a solid. Each orbital has its own set of quantum numbers such as energy, angular momentum and projection of angular momentum. Depending upon the coordination geometry, these orbitals can adopt different shapes. For example, consider a transition-metal atom with octahedral coordination (Fig. 1.1 (a)) where anisotropic-shaped  $d$  orbital electrons are bound by Coulomb forces to the atomic nucleus. There is a slight electrostatic perturbation of transition metal  $d$  orbitals by surrounding oxygen ions,  $O^{2-}$ , which lowers the degeneracy of orbitals and gives rise to crystal field splitting of the  $d$  orbitals. As a result the five  $d$  orbitals are divided into two sets: two orbitals pointing directly towards near-neighbour oxygen ions have higher energies as compared to three orbitals which are directed between them.<sup>2</sup> The orbitals  $x^2 - y^2$  and  $z^2$  are called  $e_g$  orbitals, whereas latter,  $xz$ ,  $yz$  and  $xy$  are called  $t_{2g}$  orbitals (Fig. 1.1).

When electrons are placed into  $e_g$  and  $t_{2g}$  orbitals, filling is carried out in accordance with the Pauli exclusion principle: No two electrons with parallel spins can occupy the same orbital. The ground state is determined by the semiempirical Hund's rule which states that the electron-electron repulsion can be reduced by placing them in different orbitals further apart from each other with parallel spins. This gives rise to the so-called spin-orbit interaction.

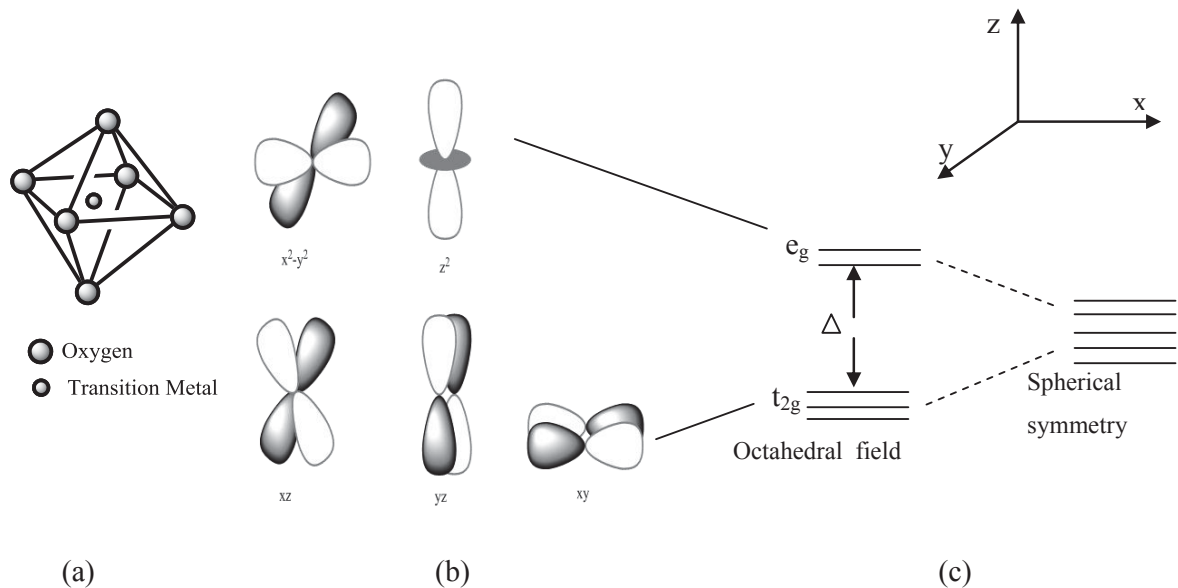


**Figure 1.1** (a) Octahedral representation of transition metal oxide. (b) Different orientations for 3d orbitals in transition metal oxides where fivefold degeneracy is lifted to two  $e_g$  [ $(x^2 - y^2)$  and  $(z^2)$ ] orbitals and three  $t_{2g}$  orbitals [( $xy$ ), ( $yz$ ), and ( $zx$ )]. (c) Crystal field splitting.

Therefore it is plausible that orbital degeneracy and strong correlations in transition metal oxides have profound effects on their physical and chemical properties. The interplay of  $d$  and  $f$  electrons' internal degrees of freedom (charge, spin and orbital angular momentum) makes strongly-correlated electron systems extremely sensitive to small changes in external parameters such as temperature, pressure or doping. This leads to a fascinating richness of spin-charge-orbital-ordered phases in transition metal oxides giving birth to some remarkable phenomena. Several of these are discussed as below.

### 1.1.1 Jahn-Teller Effect

As noted above, the transition metal oxide complexes can adopt various electron configurations and consequently can undergo certain geometrical distortions. In 1937, H. A. Jahn and E. Teller explained some of the geometrical distortions observed in transition metal oxides in the famous Jahn-Teller theorem which states that any non-linear molecule in an electronically degenerate state will distort to remove degeneracy by lowering the symmetry and energy.<sup>2</sup> In an electronically degenerate state, the orbitals are asymmetrically

occupied because of the fact that more than one orbital is available for an electron which results in an increased energy of the orbitals. Therefore, the system lowers the energy by lowering symmetry, splitting the degenerate energy levels and occupying the lower-energy orbitals. These changes in symmetry lead to geometrical distortions. These distortions are known as Jahn-Teller distortions and are most often encountered in octahedral transition metal oxides when an odd number of electrons occupy  $e_g$  orbitals. In this case, these complexes have doubly-degenerate electronic ground states and since  $e_g$  orbitals always point directly at ligands, the distortion can result in a large energetic stabilization. As a result there is a significant increase in the metal-oxide bond length and a reduction in symmetry from octahedral to tetragonal field.

The Jahn-Teller theorem should also strictly apply to the systems where  $t_{2g}$  orbitals are incompletely occupied. However, since  $t_{2g}$  orbitals point away from ligands the stabilization energy obtained by distortion is smaller.<sup>3</sup> This makes the Jahn-Teller effect less pronounced in such systems.

### **1.1.2 Mott Insulators**

Insulating and metallic states of a material can be successfully distinguished by the band theory of solids which states that if there is a non-zero electron density at the Fermi level then the material will behave as a conductor while a zero electron density at the Fermi level would mean the system is insulating. Conductors have partially-filled bands with the Fermi level lying within these bands and usually the system has an odd number of electrons per unit cell. Since the electron density at the Fermi level vanishes for insulators, the Fermi level lies between completely filled and completely empty bands. Thus these systems should have even number of electrons per unit cell.

Although band theory successfully describes various electrical properties of different materials, there is a class of insulating transition metal oxide systems which according to band theory should be conductors.<sup>4</sup> These insulators are known as Mott Insulators, named after Neville Mott who first explained this anomaly in 1937.<sup>4</sup> In Mott insulators conductivity approaches zero as temperature is lowered even though band theory would predict them to be metallic. The most important difference between Mott insulators and conventional band insulators is very fundamental: the Pauli exclusion principle prohibits conductivity in band insulators while it is the electron-electron repulsion that blocks the charge flow in Mott insulators. Generally, in Mott insulators the highest occupied band contains one electron per

unit cell in which case the electron flow would require creation of a doubly-occupied site. If the electron-electron repulsion is strong enough, the amount of charge per unit cell becomes fixed and this electron flow will be blocked, leaving only the electron spin on each site to fluctuate. One way of viewing this is that by forming an antiferromagnetic ground state, the unit cell doubles in size so that there is now an even number of electrons per unit cell – in band theory a recipe for an insulator. Doping can restore electrical conductivity by creating vacant sites to which electrons can jump without incurring a cost in Coulomb repulsion energy.<sup>1</sup>

However, in reality, when carriers are doped into Mott insulators, the charge transfer from dopant species introduces additional degrees of freedom that further complicate the electronic phase. Despite the fact that the basic crystal structure remains the same after doping, there are some drastic changes caused by the partial substitution of one chemical element for another in the host network. Ideally, it is expected that minimal doping of electrons or holes would trigger the metal-insulator transition but usually a critical doping level is required to destroy the various long-range charge, spin and orbital order. Often, the material remains electrically insulating or marginally metallic over a broad range of band filling where holes or electrons accumulate to form a periodic array, including charge density waves, spin density waves or both.<sup>1</sup>

Based on the above discussion it can be concluded that Mott insulators have the following three characteristic features (i) non-metallic character suggesting the presence of band gap (ii) magnetic properties showing the existence of unpaired electrons and (iii) crystal field transitions characteristics of open shell  $d^9$  ions.<sup>2</sup>

Mott insulators are of growing interest in physics research and they have applications in switches, field-effect transistors, and high-temperature superconductivity. Representative examples include NiO and CoO. Superconductivity in high- $T_c$  cuprates persists in CuO planes which are Mott insulators in the undoped state.

### **1.1.3 Colossal Magnetoresistance**

Colossal magnetoresistance (CMR) is a property of some materials that, at certain temperatures, enables them to dramatically increase or decrease their electrical resistance by many orders of magnitude when a relatively small magnetic field is applied.<sup>5</sup> CMR was initially discovered in manganese based perovskite oxides in 1950 where it was observed that

a small external magnetic field aligns the spins on Mn sites, and that alignment influences the conduction of electrons through adjacent oxygen atoms.<sup>6</sup> This effect transforms the material from a charge-ordered/orbital-ordered (COOO) insulator into a ferromagnetic metal, with a dramatic change in resistivity.<sup>1</sup> A full quantitative understanding of the CMR mechanism is elusive but it is believed that near the magnetic transition, switching on a magnetic field helps align the neighbouring spins thus facilitating the hopping from Mn(III) to Mn(IV) sites and causing dramatic changes in resistivity. A typical example is a perovskite material  $\text{LaMnO}_3$  where 20-40% hole doping (substitution of La with Ca or Sr) leads to an insulator to metal transition.<sup>6</sup> A large magnetoresistance is observed near this phase transition which has possible applications in magnetic recording. Large magnetoresistance has also been observed in Cr chalcogenide spinels and  $\text{Tl}_2\text{Mn}_2\text{O}_7$  systems.<sup>6</sup>

Magnetoresistance can be an intrinsic or extrinsic property depending on the composition of materials. Intrinsic magnetoresistance arises due to intrinsic interactions in the materials and is maximum near the ferro-paramagnetic transition. Magnetoresistance can also arise due to extrinsic properties, for example, grain boundary in polycrystalline samples and external barriers where low magnetic fields can lower the resistance in a wide range of temperatures below  $T_c$ .

#### **1.1.4 High Temperature Superconductivity**

Superconductivity is one of the most fascinating and challenging fields of modern physics. H. Kammerlingh Onnes successfully liquefied helium in 1908 which started a new era of materials characterization at very low temperatures. In 1911, Onnes investigated the low-temperature resistivity properties of mercury and observed that resistivity of mercury fell abruptly to zero at 4.2 K. After repeating the measurements several times he proposed that mercury enters a novel physical state when cooled below 4.2 K. He named the phenomenon as superconductivity and the temperature at which it occurred as transition temperature,  $T_c$ .<sup>7</sup>  $T_c$  can be defined as the midpoint of resistive transition and it gives information about best continuous superconducting path that percolates through the superconductor. However, it does not reflect the actual volume properties of superconducting materials. Discontinuous or even isolated superconducting phases within a sample can better be revealed by magnetic susceptibility measurements but these measurements may lead to slightly lower values of  $T_c$ , possibly, because of partial suppression of superconductivity by penetrating magnetic field. Initially superconductivity was considered as a state of zero electrical resistance. However, in

1933 Meissner and Ochsenfeld discovered that superconductors are not merely perfect conductors of electricity but they also exhibit very interesting magnetic properties such as perfect diamagnetism. They observed that when a superconductor is placed in an external magnetic field and cooled below its transition temperature, the magnetic field lines are ejected.<sup>8</sup> The applied magnetic field produces a magnetic flux density inside the superconductor but the diamagnetic superconducting screening current produces a flux density equal and opposite to the magnetic flux density thus cancelling the net magnetic field to zero. At this point the superconductor is said to be entered the Meissner state which breaks down when applied magnetic field becomes too large. After the Meissner effect another major attempt to explain the phenomenon of superconductivity was made by Vitaly Lazarevich Ginzburg and Lev Landau in 1950. They put forward the so-called “phenomenological” theory which models superconductivity using classical thermodynamic arguments. The most important findings of the theory were the prediction of two characteristic lengths within superconductors: (i) the coherence length,  $\xi$ , which describes the length scale for thermodynamic fluctuations in a superconductor, and (ii) the penetration depth,  $\lambda$ , which defines the maximum depth to which an applied magnetic field can penetrate in a sample.<sup>9</sup> This theory only examines macroscopic properties of superconductors without explaining the underlying microscopic mechanism. In 1957, Bardeen, Cooper and Schrieffer proposed the so-called “BCS” theory of superconductivity that explains, using advanced ideas of quantum mechanics, the underlying microscopic phenomena of superconductivity. According to BCS theory, the supercurrent within the superconductor is carried by Cooper pairs instead of the individual electrons that are responsible for current flow in normal conductors.<sup>10,11</sup> Cooper pairs are formed when two electrons with opposite spins link-up through lattice vibrations – the phonons. Since electrons are fermions (spin-1/2), the paired electrons form boson like quasi-particles which all occupy the lowest-level energy states and are phase coherent as they pass through the entire sample in unison without any scattering and hence without any resistance. However, these Cooper pairs have a very small binding energy of  $10^{-3}$  eV, so small that even thermal fluctuations at room temperature are sufficient to break up the pairing. Therefore, only at very low temperature can a significant number of electrons in a metal form Cooper pairs and it was believed that BCS – like superconductivity would be highly unlikely above 30 K. However, in 1986, Bednorz and Muller made an important breakthrough by discovering superconductivity in layered copper oxide system ( $\text{Ba}_x\text{La}_{5-x}\text{Cu}_5\text{O}_{5-y}$ ) at 35 K, which won them a Noble prize in 1987.<sup>12</sup> This was the birth of high-temperature superconductivity. The main feature of these high- $T_c$  superconducting

cuprates is that the superconductivity occurs within two-dimensional CuO<sub>2</sub> planes separated by charge-reservoir oxide layers.<sup>13</sup> The crystal structure of high- $T_c$  superconducting cuprates consists of distorted, oxygen deficient, multi-layers of CuO<sub>2</sub> planes which are separated from each other by planes of various other oxides while all the available theoretical and practical knowledge suggests that superconductivity and charge transport are confined to CuO<sub>2</sub> planes. The electron conduction is highly anisotropic due to the layered structure which is believed (though not proved) to be essential for high- $T_c$  superconductivity. The most important debating point concerning the origin of high- $T_c$  superconductivity is the relationship between the superconductivity and structural anisotropy as a consequence of layered structure of these materials.<sup>13</sup> Despite a vast quantity of ongoing research and many applications being promised by high- $T_c$  superconductivity, an exact explanation of the phenomena has so far eluded scientists.<sup>13</sup> Many theories were presented over the years to explain the possible mechanism for high- $T_c$  superconductivity.<sup>13-15</sup>

According to (WHA) model<sup>15</sup> the superconducting transition temperature  $T_c$  of a layered cuprate superconductor is expressed in terms of

$$\lambda = \lambda_0 + \lambda_1$$

where  $\lambda_0$  is the interlayer coupling between the nearest CuO<sub>2</sub> planes (intra block coupling) and  $\lambda_1$  is the interlayer coupling between the next nearest planes (inter block coupling).<sup>15</sup> A close correlation between transition temperature and two-dimensional carrier density ( $n_s/m^*$ , where  $n_s$  is the superconducting carrier density and  $m^*$  is the effective mass) has also been suggested as a signature of unconventional Bose-Einstein condensation in the layered high- $T_c$  superconductors.<sup>13</sup> More detailed studies based on muon-spin relaxation show that  $T_c$  does not correlate universally with  $n_s/m^*$ .<sup>16</sup> These issues remain controversial and exact understanding of the origin of superconductivity in high- $T_c$  superconductors is still a major problem of theoretical condensed matter physics.<sup>17</sup>

Despite the apparent lack in exact understanding of nature high- $T_c$  superconductivity, technical research is focused on preparing high- $T_c$  superconductors. Since the discovery of high- $T_c$  superconductors many cuprate oxides with superconducting transition temperatures as high as 135 K at ambient pressure and 163 K at high pressure have been discovered.<sup>18,19</sup> More recently, the discovery of superconductivity in iron arsenides, doped tungsten oxides and organic-inorganic hybrids has broadened not only the spectrum of materials that could be

high- $T_c$  superconducting but also the methods that could be used to induce superconductivity.<sup>20-22</sup>

Based on the above discussion we can conclude that there are three essential conditions to achieve superconductivity: (i) The materials are quasi-two-dimensional (ii) High- $T_c$  is created by doping a Mott insulator (iii) The close proximity of an insulating phase and low dimensionality would cause a new material to exhibit fundamentally new behaviour.

We shall now review some progress in the field of hybrid organic-inorganic layered electronic materials.

## **1.2 Hybrid Organic-Inorganic Layered Electronic Materials**

With technological breakthroughs increasingly happening around the globe the need for novel materials which are cost effective, light weight and energy efficient is increasing as ever. Scientists and engineers realised that many well-established materials, like plastics, ceramics or metals cannot fulfil the technological needs required for various new applications and found that the combination of certain materials to form hybrids can show extraordinary properties when compared with their original components<sup>23</sup>. Most of the resulting materials show improved mechanical properties and one well-known example is inorganic fibre-reinforced polymers.<sup>23</sup> The main motivation behind creating a hybrid material is to utilize the electrical, mechanical, thermal and structural properties of the inorganic material and flexibility, functionality and templating ability of the organic material.<sup>24</sup> Organic-inorganic hybrid materials are not only useful for the design of new compounds for academic research but their unusual features and versatile characteristics open up promising applications in many fields such as electronics, optics, optoelectronics, mechanics, environment, medicine and biology.<sup>25</sup> Before going into the operational details of these hybrid materials it's worth understanding what exactly these materials are and how they originated.

### **1.2.1 Definition: Hybrid Materials**

The term “ Hybrid material” is used very broadly and has been applied to different systems such as metal-organic frameworks, highly-ordered polymers, sol-gel compounds and macrostructural inorganic particles in an organic matrix.<sup>26,27</sup> A general definition can be made as following: a material obtained by mixing two different moieties together is known as a hybrid material where, in most cases, one part of the resulting material is organic and the

other one is inorganic in nature.<sup>23</sup> These materials could also be defined as molecular or nano-composites with organic (or bio) and inorganic components, intimately mixed where at least one component's domain has dimensions ranging from a few angstroms to few nanometres.<sup>27</sup> Consequently, these materials appear biphasic in nature with organic and inorganic materials mixed together at very small scale and generally structurally ordered. But it is obvious that the hybrid material is not just a physical mixture of the two different kinds of materials resulting from the individual contributions of two phases, rather the role of the inner interfaces could also be very important and it is the nature of interface which grossly divides the hybrid materials into two important classes.<sup>28</sup> Class I hybrid materials are those in which organic and inorganic compounds are linked together by weak bonds (van der Waals, hydrogen and ionic bonds) while strong bonds (covalent or ionic-covalent bonds) enjoin organic and inorganic species to give class II hybrid materials.<sup>14</sup> Because of the potential for gradual change in the strength of chemical interactions it becomes clear that there is potentially a range of hybrid materials that are intermediate between these weak and strong limits.<sup>23</sup>

### **1.2.2 Origins of Hybrid Materials**

Far before human beings were able to combine the strength of inorganic materials and flexibility of organic materials into one unique compound hybrid materials were present in nature. The most basic example is bone or nacre where one third contains organic materials (collagen) and the remainder consists of inorganic mineral (hydroxyapatite).<sup>29</sup> Another of nature's remarkable features is its ability to combine at the nanoscale organic and inorganic components allowing the construction of smart natural materials that found a compromise between different properties or functions (mechanics, density, permeability, colour, hydrophobia, etc.) thus producing beautifully carved structures found in radiolarian or diatoms (Fig.1.2), crustacean carapaces or mollusc shells and teeth tissues in vertebrates.<sup>30</sup>

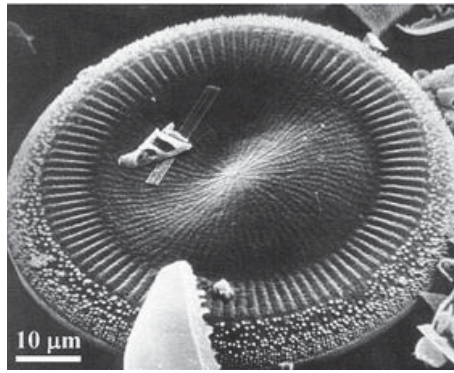


**Figure 1.2** Silicic skeleton of a diatom, showing complex and finely carved morphology in scanning electron microscopy.<sup>31</sup>

The possibility of synthetically combining organic and inorganic materials to produce state-of-the-art materials was not considered until the start of the industrial era, where scientists of those times used to produce paints by suspending inorganic pigments ( $\text{TiO}_2$ , etc) in organic mixtures (solvents, etc).<sup>25</sup> Adobe, which consisted of clay and straw, is another example of man-made hybrids and it was used to construct buildings in ancient times.<sup>32</sup> Maya blue is a beautiful example of man-made hybrid materials that combines the colour of an organic pigment such as blue indigo and the resistance of an inorganic host such as palygorskite to maintain its brightness for twelve centuries (Fig. 1.3).<sup>30</sup> Apart from its beauty and resistance to biodegradation, Maya blue shows unprecedented stability when exposed to dilute acids, alkalis, organic solvents, oxidants and reductants.<sup>33</sup>



**Figure 1.3** Computer enhanced Mayan warrior from Bonampak.<sup>30</sup>

The modern concept of “hybrid organic-inorganic materials” emerged very recently when research turned towards the higher added-value applications where organic and inorganic compounds interact with each other at the molecular level.<sup>25</sup> Paints are a good link between Mayans and modern applications of hybrid materials while the widespread work on hybrid organic-inorganic materials was pursued with the development of the polymer industry where inorganic fillers (minerals, clays, etc) were added to polymers in order to improve their properties.<sup>30</sup> The development of organic-inorganic hybrid materials exploded in 1980’s mainly due to the development of soft inorganic chemistry processes, especially sol-gel processes, where mild synthetic conditions allow versatile access to chemically-designed combinations of inorganic domains obtained via inorganic polymerization reactions with fragile entities such as organic or even bioactive molecules.<sup>34</sup> Since then the study of hybrid materials became an expanding field of investigation yielding advanced innovative materials that promise a wide range of possibilities to elaborate tailor-made materials in terms of chemical and physical properties<sup>34</sup>. The potential offered by the hybrid materials is now becoming reality with many hybrids entering the markets that aim to have higher levels of sophistication, miniaturization, recyclability, and respect to the environment and less energy consumption.

### **1.2.3 Properties and Applications of Hybrid Materials**

The properties of hybrid organic-inorganic materials have been investigated with regard to their applications over the years, resulting in a huge development in advanced multi-functional materials which will impact on future applications in fields like, electronics, optics, optoelectronics, biology, mechanics, electrochemistry, medicine and environment.<sup>18-31</sup>

The characteristics of existing hybrid materials include tunable magnetic, superconducting, optical and mechanical properties, improved membrane based or catalytic properties, excellent laser efficiencies, good photo stability, very fast photochromic response and very high and stable second-order and non-linear optical response.<sup>18-35</sup> While these characteristics of hybrid organic-inorganic materials are useful for their role in a large number of practical applications, it is beyond the scope of this work to discuss all these properties and applications. However, a brief account of the phenomena of superconductivity in hybrid materials is discussed here followed by their applications in various scientific areas.

### 1.2.3.1 Superconductivity in Hybrid Materials

The basic difference between a superconductor and normal conductor is that in the former the current carriers are pairs of electrons (Cooper pairs), while in the latter, to a first approximation, the electrons move independently. The Coulomb repulsion between electrons is nullified by the attractive potential created because of the interaction between electrons and lattice vibrations. However, the presence of a magnetic field can overcome the pairing energy and return the superconductor to the normal state. Thus, superconductors are characterized by a critical field,  $H_c$  as well as a critical temperature,  $T_c$ .<sup>36</sup>

An exact understanding of possible mechanism for high- $T_c$  is still elusive. However, technical research is focused on preparing high- $T_c$  superconductors materials by optimizing their properties in relation to their applications. One way to optimize the properties is to insert guest species into the two-dimensional host lattices; this is expected to be a cost effective route to prepare layered structures of hybrid organic-inorganic materials with superconducting properties in high- $T_c$  domain.<sup>17</sup> The use of hybrid materials for making high- $T_c$  superconductors has multi-purposes; investigating the high- $T_c$  superconducting mechanism at a fundamental level, developing new high- $T_c$  superconductors and using these materials for practical applications.<sup>13</sup> Many examples of organic-inorganic heterostructures with superconducting properties can be found in the literature.<sup>13,14,17,22,37-39</sup> For example, TaS<sub>2</sub> is a superconductor with a  $T_c$  of 0.7 K, however, intercalation of pyridine between inorganic layers increases  $T_c$  to 3.5 K in the resultant material TaS<sub>2</sub>(pyridine)<sub>0.5</sub>.<sup>40</sup> More recently, a slight increase in  $T_c$  (from 78 K to 82 K) has been observed after incorporating a neutral pyridine ligand into the HgI<sub>2</sub> preintercalated high- $T_c$  Bi<sub>2</sub>Sr<sub>2</sub>CaCu<sub>2</sub>O<sub>y</sub> superconductor.<sup>22</sup>

### 1.2.3.2 Optical Systems

Hybrid organic-inorganic materials have excellent optical properties that can be exploited to achieve next-generation materials. Some remarkable examples based on optical properties of hybrid materials are presented here.

#### Organic Chromophores in Sol-Gel Matrices

Due to their thermal instability organic molecules could not be incorporated into inorganic matrices until the emergence of sol-gel derived glass films which allow incorporating large amounts of organic and inorganic materials during the process of glass formation.<sup>41</sup> Many

organic dyes are now incorporated into silica or aluminosilicate based materials thus producing transparent films of excellent optical quality and great mechanical strength.<sup>35</sup>

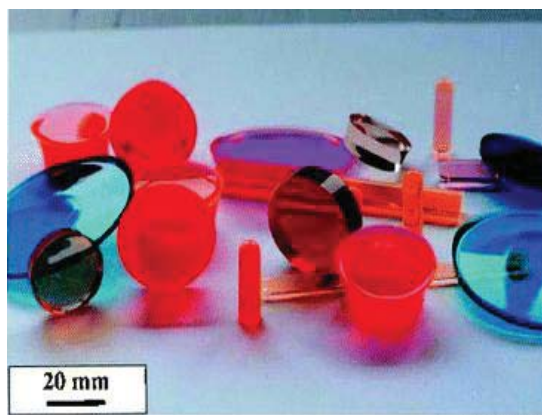


**Figure 1.4** Organic-inorganic hybrid materials containing organic chromophores.<sup>30</sup>

### **Photochromic Hybrid Materials**

Photochromic materials are those materials which reversibly change colour upon changing the light intensity. Photochromic hybrid materials can be used for designing various devices such as privacy shields, optical switches, optical data storage devices, energy-conserving coatings and eye-protection glasses depending upon the rate of optical transformation. Fast optical transformations are required for optical switches and optical data storage devices work with slow transformations.<sup>42</sup> Concerning photochromic devices, transition between strong and fast photochromic coloration and a very fast thermal fading is needed which can be obtained by careful adjustment of the interface experienced by the dye.<sup>43</sup>

### **Solid-State Dye Laser Hybrid Materials**

Dye lasers have been used for many years because they provide an optical medium with excellent transparency, good slope efficiency, high output energy pumping, sufficient thermal conductivity and a long life-time. These excellent features can be achieved in hybrid materials by optimizing the dye/matrix system. Solid-state dye lasers employing luminescent dye-doped sol-gel matrices have already been demonstrated.<sup>44</sup> Hybrid solid-state dye lasers can operate at about 1 mJ output energy at 20 Hz with a single sample lasting for several months forecasting these tunable solid-state dye lasers as a possible substitute for liquid dye laser systems in several applications.<sup>35</sup>

## Hybrid Optical Sensors

Attractive optical properties, ease of processing, tunability of physical properties, high mechanical, thermal and photochemical stability, chemical inertness and negligible swelling in both organic and inorganic solvents have characterized organic-inorganic sol-gel derived hybrid materials for sensor applications.<sup>35</sup> In the field of hybrid optical sensors, much attention has been devoted to sensing the acidity, air moisture, traces of hydrogen peroxide, hydrazine etc.<sup>45-46</sup> Hybrid optical sensors which are used to discriminate the emission of benzene and toluene contaminants into the atmosphere have also been prepared.<sup>47</sup>

### 1.2.3.3 Bioactive Hybrid Materials

Bioactive hybrid materials find applications in the field of biotechnology because of their remarkable aerodynamic, hydrodynamic, wetting and adhesive properties. The resulting applications include biosensors and bioreactors, surface coatings and also cosmetic products. Hybrid materials can be used to prepare high Sun Protection Factors (SPF) by encapsulating the organic UV filters (80 % w/w of final product) in silica microcapsules thus producing biocompatible sunscreens (Fig. 1.5) which markedly reduces undesirable skin alterations and melanomas by sun-induced premature skin aging.<sup>48</sup>

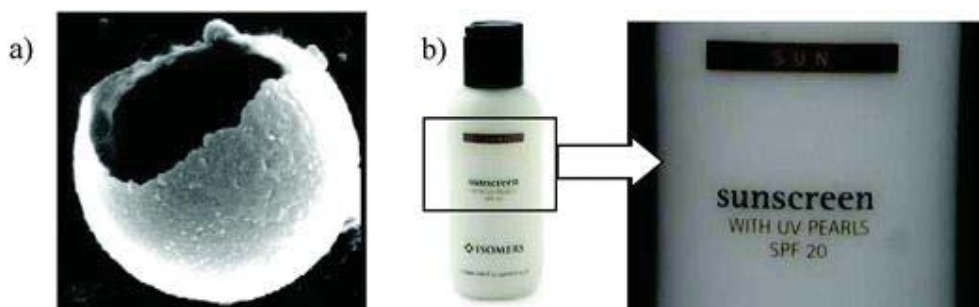


**Figure 1.5** (a) A core-shell silica microcapsule for carrying potent chemicals. (b) Commercial Sunscreen SPF 20.<sup>48</sup>

There are many other applications of bio-hybrids which include anti-body-based affinity biosensors used for the detection of various chemicals, hybrid sol-gel immune sensors used to analyse pesticides, super hydrophobic or super hydrophilic coatings inspired by lily leaves and much more (Fig. 1.6).<sup>30,49</sup>

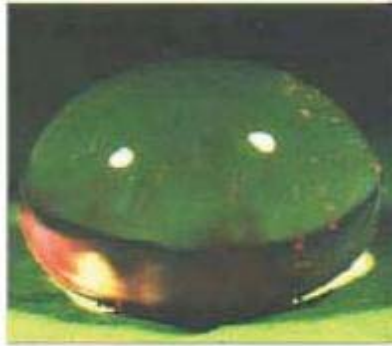


**Figure 1.6** Artificial hydrophobic coatings inspired by lily leaves.<sup>30</sup>

#### 1.2.3.4 Hybrid Materials for Protective Coatings

Hybrid materials which are used for protective and decorative coatings are among the earliest in their class to enter the commercial market. The examples are one million television sets sold annually by Toshiba, the screens of which are coated with hybrid materials made of indigo dyes embedded in a silica/zirconia matrix,<sup>50</sup> glassware coated with dye coloured hybrid coatings (Fig. 1.7 a),<sup>30,47</sup> and easy to recycle coloured glass bottles coated with hybrid organic-inorganic materials (Fig. 1.7 b).<sup>30</sup> These coatings not only provide access to a variety of colour combinations, thus attracting consumers, but are also of greater mechanical strength and are easy to recycle as uncoloured glass.<sup>23</sup>

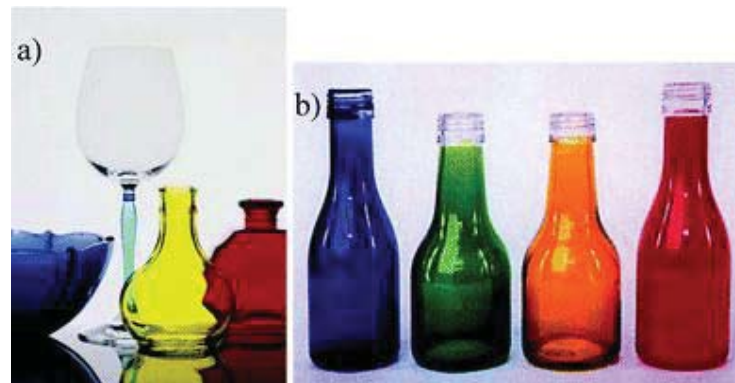


**Figure 1.7** (a) High quality optical appearance of crystal glass. (b) Easy to recycle coloured glass bottles coated with hybrid organic-inorganic materials.<sup>30</sup>

### 1.2.3.5 Hybrid Materials for Microelectronics

Hybrid materials also find their way in electronics industry and are useful in electrical component coatings such as resistors and moulding compounds, as well as spin-on dielectrics in microelectronic interlayer and multilayer dielectric and planarization applications.<sup>30</sup> The advantage of tuning the hybrid's flexibility and adhesion properties allow their use on flexible substrates such as waveguides (Fig. 1.8).<sup>51</sup>



**Figure 1.8** ORMOCER waveguides where the hybrid coating is deposited on a flexible foil.<sup>51</sup>

Hybrid organic-inorganic materials also find applications in optoelectronics due to their high optical transmission. One example is photopatternable organic-inorganic copolymers with negative resistance that have been developed as thin-film materials using ORMOCER (ORganically MODified CERamics) technology for optoelectronic packaging purposes e.g. MCM-L/D or o/e MCM packaging (Fig. 1.9)<sup>52,53</sup>

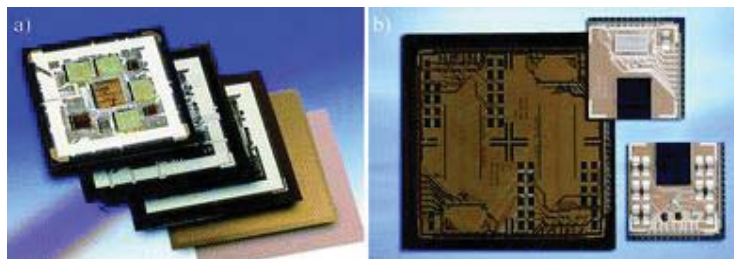


**Figure 1.9** (a) Pentium MCM-L/D manufactured in ORMOCER. (b) Electro-optical o/e MCM manufactured in ORMOCER.<sup>30</sup>

### 1.2.4. Classification of Hybrid Materials

Hybrid organic-inorganic layered electronic materials can be classified into different categories on the basis of their applications (as discussed above), on their chemical nature or on the basis of their synthesis type. A classification of hybrid materials based on the nature of their chemical bonding has already been reported.<sup>25</sup> There are numerous methods to synthesize hybrid organic-inorganic layered electronic materials, including: slow crystallization from solution, hydro or solvothermal synthesis, *chimi douce* (soft chemistry) methods, gas-phase reactions, polymerization of organic materials into inorganic host lattices, electrochemical crystal growth and solid-state reaction.<sup>54</sup> The hybrid organic-inorganic layered materials prepared by using these methods can be further separated into following major categories.

#### 1.2.4.1 Silicon-Alkoxides-Based Hybrid Organic-Inorganic Materials

Hybrid organic-inorganic materials obtained from organically-modified silicon alkoxides are prepared by sequential synthesis. It is a two step process in which both the organic and inorganic networks are prepared sequentially, where polycondensation of a silicon alkoxide creates an inorganic network followed by organic polymerization to complete the process.<sup>55</sup> The hybrid materials formed in this way are usually known as ORMOSILs (ORganically MODified SILanes) or ORMOCERs (ORganically MODified CERamics).<sup>56</sup> Polyfunctional alkoxy silanes are organic units (R') to which two or more trialkoxysilane groups  $\text{Si}(\text{OR})_3$  are linked through Si-C bonds giving a generic formula  $(\text{RO})_3\text{Si}-\text{R}'-\text{Si}(\text{RO})_3$ . A further polycondensation of the trialkoxy group leads to the formation of the hybrid organic-inorganic materials.<sup>57</sup>

#### 1.2.4.2 Phosphate-Based Hybrid Organic-Inorganic Materials

Phosphate-based hybrid organic-inorganic materials are prepared by hydrothermal or solvothermal synthesis forming layered structures involving 1, 2 or 3 dimensional networks.<sup>58</sup> In most cases the metal atoms are linked to the oxygen atoms of  $\text{PO}_4^{3-}$  tetrahedra in order to form a hybrid structure.<sup>59</sup> Aluminophosphates, along with their isomorphous substituted forms, belong to the most studied class of tetrahedral-framework-forming compounds.<sup>59</sup> The most common intercalates are aminoalkane cations which are used to occupy the interlayer space (Fig. 1.10). Recently, some phosphate-based hybrid materials were reported which do not require the need of an external structural agent to form the hybrid structure.<sup>60</sup>

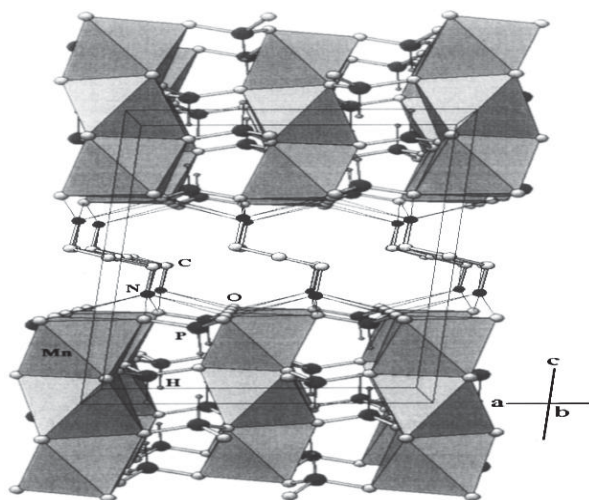


**Figure 1.10** Layered structure of manganese phosphite stacking along  $c$ -axis with alkyldiammonium ions filling the interlayer space.<sup>59</sup>

### 1.2.4.3 Perovskite Based Hybrid Organic-Inorganic Materials

Perovskite materials can be described schematically as  $ABX_3$ , where A cations and X anions together form a close packed array, while B cations are located within the octahedral voids created by the X anions of adjacent layers (Fig. 1.11).<sup>61</sup>

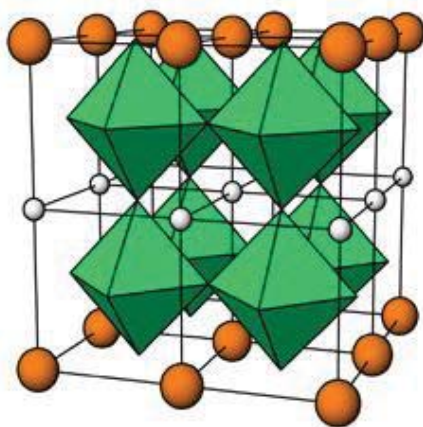


**Figure 1.11** A layered perovskite material.<sup>61</sup>

Over the years many perovskite layered hybrid organic-inorganic materials have been prepared using soft chemistry methods. Layered oxide structures  $K[Ca_2Na_{n-3}Nb_nO_{3n+1}]$  ( $3 \leq n \leq 7$ ) were synthesized as a pioneering work in the field of perovskite-related hybrid materials (Fig. 1.12).<sup>62</sup>

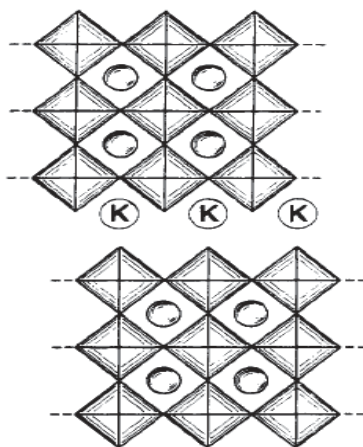


**Figure 1.12** Layered structure of  $KCa_2Nb_3O_{10}$  where Ca atoms (small circles) occupy the interlayer space formed by corner shared  $NbO_6$  octahedra.<sup>62</sup>

Aurivillius phases, generally formulated as  $(M_m[A_{n-1}B_nO_{3n+1}])$ , are ion-exchangeable layered perovskites where  $[A_{n-1}B_nO_{3n+1}]$  form a layered structure and  $M_m$  works as interlayer cations.<sup>63</sup>

#### 1.2.4.4 Transition-Metal Oxide Based Hybrid Organic-Inorganic Layered Materials

Transition metal oxide (TMO) based organic-inorganic layered materials can be synthesized by hydrothermal reactions of parent metal alkoxide compounds with organic ligands. The organic ligands modify the basic metal oxide structures by taking into account the charge and number of coordination sites of organic groups in order to rationalize the final structure. Excellent functionality and structural diversity offered by transition metal oxides has resulted in synthesis of a huge number of functional organic-inorganic materials which offer promising applications in the fields of electrochromic materials, microelectronics, optoelectronics and even novel superconductors. In order to fully understand different physical and chemical properties exhibited by these state-of-art TMOs it is worthwhile to first understand their structural features before exploring the synthesis of various hybrid materials which are made of these materials.

Tungsten and molybdenum oxides have analogous structures and sharing configurations that are almost identical to each other.<sup>64</sup> Consider tungsten oxide which is a rather complex system because of having large number of phases where  $\text{WO}_6$  octahedra can be arranged in various sharing configurations – corners, edges, planes.<sup>65</sup> These different structural phases have a slightly different position of the W atom within the octahedra and small variations in W–O bond lengths, often associated with valence charge. At room temperature the most stable of different tungsten oxide phases is monoclinic  $\text{WO}_3$  which has a perovskite structure where each W occupies corners of the primitive cell and O ions are present at the centre of edges (Fig. 1.13). The central atom, which is absent in the parent phase, enables intercalation of metal ions which can be either of the Li, Na, Mg etc., depending on the type of the final compound – tungsten bronze.<sup>66</sup> The doping levels can be varied to achieve the requisite properties that a particular tungsten bronze exhibits. The  $\text{ReO}_3$  type structure of a  $\text{WO}_3$  can be described in terms of infinite arrays of corner sharing octahedra which are held together by covalent or ionic (or both) interactions (Fig. 1.14). Stacking these layers along the z- direction leads to the formation of small extended tunnels which enable intercalation and possible ionic transport within the structure (Fig. 1.14). Edge sharing arrangement of  $\text{WO}_6$  octahedra leads to formation of reduced tungsten trioxide species ( $\text{WO}_{3-x}$ ). Similar to the  $\text{ReO}_3$  structures, edge-sharing of these octahedra results in the formation of vacant tunnels as well (Fig. 1.15)<sup>65</sup>. Edge-sharing arrangement also compensates oxygen deficiency in substoichiometric tungsten oxides such as  $\text{W}_{18}\text{O}_{49}$  ( $\text{WO}_{2.72}$ ) and  $\text{W}_{20}\text{O}_{58}$  ( $\text{WO}_{2.90}$ ).<sup>67</sup>

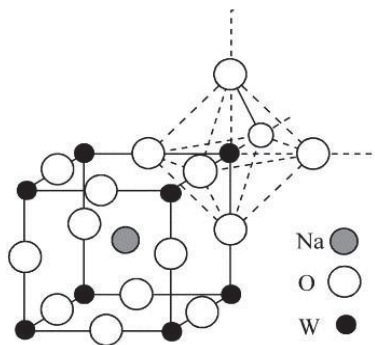


**Figure 1.13** Octahedral symmetries as demonstrated by perovskite tungsten bronze unit cell.<sup>68</sup>

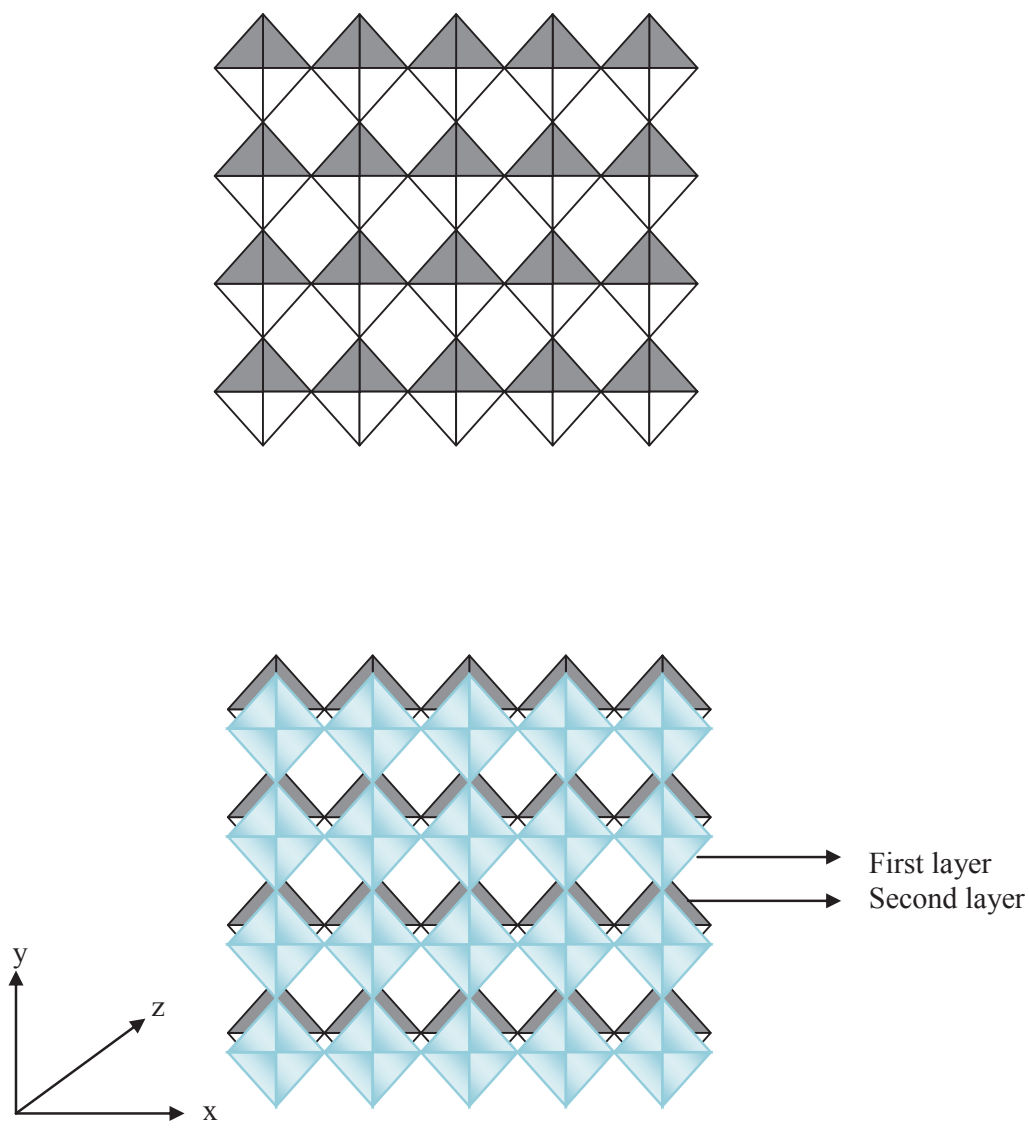


**Figure 1.14** Tungsten oxide octahedra arranged in corner-sharing configuration to form monoclinic  $\text{WO}_3$  (above) and two layers of octahedral tungsten oxide stacked so as to reveal vacant tunnels along the z-direction (below).

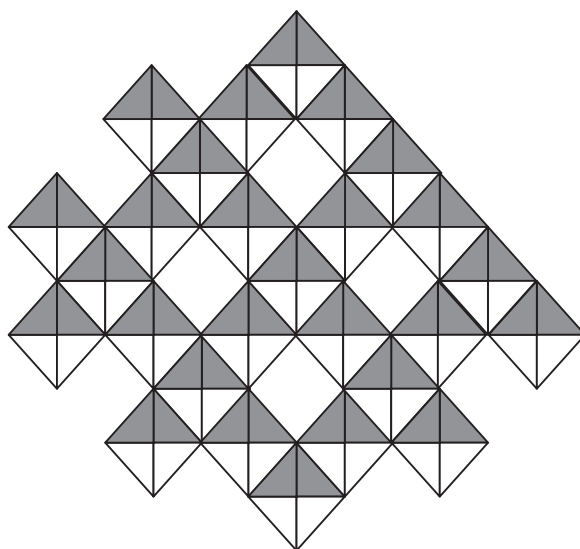


**Figure 1.15** Edge-sharing arrangement of  $\text{WO}_6$  octahedra leads to formation of substoichiometric  $\text{WO}_{3-x}$ .

Now we discuss different types of organic-inorganic hybrid materials that involve transition metal oxides. The structural diversity of TMOs can be greatly enhanced by introduction of organic ligands in order to make one, two or three dimensional hybrid materials. Different reaction parameters such as pH, temperature, heating/cooling rate, length of organic ligand and nature of terminal group provide the control for engineering the physical and chemical properties of the final product. Basically, TMO-based hybrid materials can be divided into three types according to the structural configurations of TMOs and their interaction with the organic ligands. Hagrman *et. al.* provided an excellent review that describes the synthesis of such materials with a particular focus on how very small changes in reaction conditions lead to the evolution of new structures.<sup>69</sup> For example, hydrothermal reactions of tungsten or molybdenum oxide with 4,4'-bipyridyl (herein “bpy”) have been reported to form a three-dimensional covalently bonded framework which consists of octahedral layers of  $\text{MO}_5\text{N}$  (where  $\text{M} = \text{W}$  or  $\text{Mo}$ ) interlinked together by bpy ligands.<sup>70,71</sup> These materials are characterized by direct bonding between organic and inorganic components of the hybrid system. The dimensionality of such coordinated systems can be reduced by simply changing the positions of terminal nitrogen on bpy in order to obtain 1D chains of corner-shared  $\text{MO}_4\text{N}_2$  octahedra.<sup>69,72</sup>

The strong covalent bonding that supports the layered structure in the above materials can be removed by slightly lowering the pH value while keeping the remaining synthesis conditions fixed. Because a slightly lower pH would trigger the protonation of organic

molecules resulting in the formation of one dimensional chains of TMOs separated by organic ligands without any direct bonding between ligand and inorganic material. For example, the synthesis of  $\text{MoO}_3(\text{bpy})_{0.5}$  and  $\text{Mo}_7\text{O}_{22}(\text{bpy})\text{H}_2$  involves similar reagents but a lower pH value of the final mixture for the latter results into the formation of 1D stepped motifs of edge- and corner-shared molybdenum oxide octahedra as compared with a covalently bonded 3D network for the former.<sup>73</sup> Similarly, by lowering the pH, it is possible to obtain different hybrid materials consisting of decatungstate species interspersed with organic molecules without any direct bonding between organic and inorganic components.<sup>73</sup> In fact, this type of hybrid materials where there is very weak bonding between inorganic layers and organic ligands are simplest among the TMO-based hybrid materials. In these compounds organic ligands act as charge-compensating cations and can be used to control the spacing between inorganic layers. For example, the synthesis of two-dimensional layered frameworks of tungsten oxide hybrids with diaminoalkanes as organic ligands has been reported to exhibit interesting structural and physical properties upon changing the length of alkane chains.<sup>74</sup>

The chemical and structural properties of TMOs based organic-inorganic hybrid materials can be optimized by introduction of heterometals. The heterometal-containing tungsten or molybdenum oxide hybrids can be classified into different categories according to sharing configurations and dimensionality of the hybrid system. We first consider hybrid systems that consist of discrete tungsten or molybdenum oxide clusters interlinked by heterometal-organic molecule coordination. These materials can be prepared in chain-, layer- and three-dimensional frameworks according to the nature of bonding between the TMO clusters and organic ligands. Examples include the chain structure of  $[[\text{Co}(\text{H}_2\text{O})_4]_2(\text{H}_2\text{W}_{12}\text{O}_{42})]$  which consists of alpha-keggin-type molecules joined by W–O–links<sup>75</sup>, the two-dimensional supramolecular network,  $[\text{Ce}(\text{H}_2\text{O})(\text{DMF})_6(\text{W}_{10}\text{O}_{32})](\text{DMF})(\text{CH}_3\text{CH}_2\text{OH})$  which comprises 1D helical chains combining decatungstate with cerium ions<sup>76</sup>, and three-dimensional network that is constructed from the six-supported  $[\text{BW}_{12}\text{O}_{40}]^{5-}$  polyoxoanions and  $[\text{Cu}^{\text{I}}(\text{bpy})]$  and  $[\text{Cu}^{\text{II}}(\text{bpy})]$  groups to give the novel 3D framework  $\text{C}_{40}\text{H}_{36}\text{BCu}_3\text{N}_8\text{O}_{42}\text{W}_{12}$ <sup>77</sup>. Similar examples are available in the literature for molybdenum oxide based hybrids. One particularly simple and interesting compound is a two dimensional ring-structure layered hybrid  $[[\text{Ni}(2,2'\text{-bipyridyl})_2]_2\text{Mo}_4\text{O}_{14}]$  where two  $[\text{Mo}_2\text{O}_7]^{2-}$  units are interlinked by two  $[\text{Ni}(2,2'\text{-bipyridyl})_2]$  groups into a cluster with a  $[\text{Mo}_4\text{Ni}_2\text{O}_6]$  ring core (Fig. 1.16).<sup>78</sup>

However, as structural complexity of the heterometal-ligand interface increases, more exotic structures are observed, e.g.  $[[\text{Cu}(\text{bpy})_4\text{Mo}_8\text{O}_{26}]^{79}$ . In this compound the linear chains of  $[\text{Cu}(\text{bpy})]$  are arranged diagonally so as to provide cavities that accommodate octamolybdate  $[\text{Mo}_8\text{O}_{26}]^{4-}$  clusters. A closely isomorphous structure with slightly different cell parameters can be obtained by replacing bpy with bispyridylethylene.<sup>80</sup>

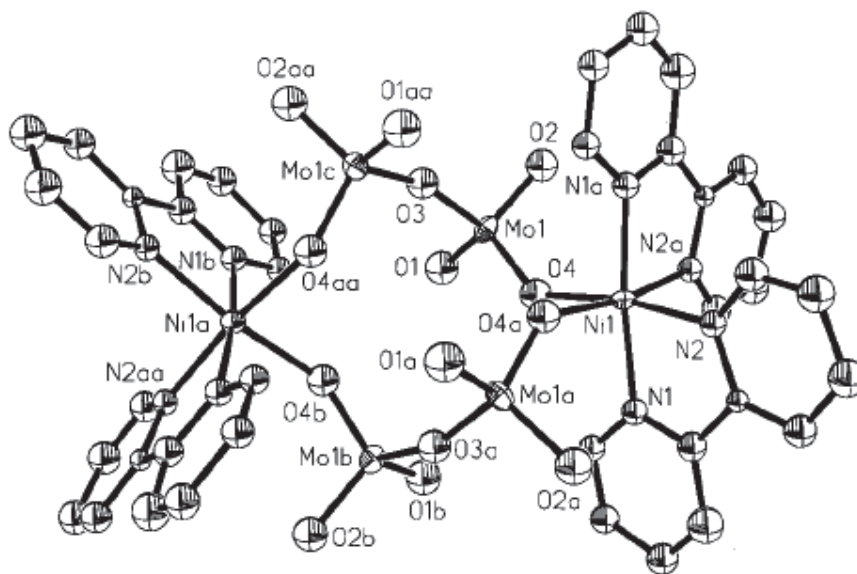


**Figure 1.16** Crystal structure of  $[[\text{Ni}(2,2'\text{-bipyridyl})_2]_2\text{Mo}_4\text{O}_{14}]^{78}$ .

Double-layer hybrids make an interesting case in heterometals-containing hybrid materials where structure propagation occurs through  $\text{M}'\text{-O-M}$  bridging instead of  $\text{M-O-M}$  ( $\text{M} = \text{W}$  or  $\text{Mo}$ ,  $\text{M}' = \text{Cu}$ ,  $\text{Cr}$ ,  $\text{Fe}$  etc). For example,  $[\text{Cu}(\text{o-phenyl})\text{MoO}_4]$  where one-dimensional chain structure is formed by interlinking molybdenum oxide tetrahedra and copper oxide square pyramids through  $\text{Cu-O-Mo}$  bridges.<sup>69</sup> Interesting sharing configurations are observed between copper and molybdenum when the organic ligand is replaced with a small pyrazine molecule to form  $[\text{Cu}(\text{pyrazine})\text{MoO}_4]$  which forms a three dimensional covalently bonded framework where the channels between bimetallic oxides are occupied by pyrazine.<sup>81</sup>

The current interest in studying the diverse structural and physical properties of tungsten and molybdenum oxides has resulted in the synthesis of a large number of functional hybrid materials. It is possible to extend the family of hybrid organic-inorganic layered

electronic materials by careful investigation of certain reaction parameters such as role of organic ligands, metal coordination geometries, pH value, heating/cooling temperature while the optimization of physical and structural features of the existing and emerging materials can be achieved by introduction of metal atoms by unique doping techniques such as ion-implantation. These are the subjects of this thesis and will be discussed in following chapters.

### 1.3 Aims and objectives

Hybrid organic-inorganic materials represent a broad field involving different types of materials, they also provide access to a class of low-dimensional materials where the inorganic component forms an extending layer framework bound by covalent or ionic (or both) interactions while the organic component provides electronic coupling between inorganic layers thus tailoring the electronic properties of the inorganic framework. One class of these hybrid materials is based on single or multiple two-dimensional layers of tungsten (or molybdenum) oxide separated by organic molecules which either ionically or covalently bind the layers together.<sup>66,70</sup> The insertion of group I or II cations into  $\text{WO}_3$  and  $\text{WO}_3 \cdot n\text{H}_2\text{O}$  leads to an insulator to metal transition, produces the intense colour and metallic luster of tungsten bronzes, and induces bulk superconductivity in, for example,  $\text{Na}_x \text{WO}_3$  with  $T_c = 3$  K for  $x = 0.2$ .<sup>82</sup> Diffusion of Na into single crystals of  $\text{WO}_3$  has even led to the formation of a granular superconducting phase around  $T_c = 91$  K.<sup>83</sup>

This work focuses on a class of hybrid materials comprising layers of octahedral tungsten oxide separated by organic spacer molecules. An example is bipyridyl tungstate comprising planes of corner-shared  $\text{WO}_5\text{N}$  octahedral linked together by bpy (i.e.  $\text{NC}_5\text{H}_4\text{-H}_4\text{C}_5\text{N}$ ). Bipyridyls form open structure channels thus giving a hint of interlayer activity. Preliminary studies show that  $\text{Na}^+$  can be incorporated by aqueous electrochemistry resulting in an increase in conductivity and appearance of  $\text{W}^{5+}$  species as evidenced by X-ray Photoelectron Spectroscopy.<sup>84</sup>

In the present work, different layered hybrid materials have been synthesized then doped by ion implantation. Detailed characterizations have been made to elucidate the evolution of important structural, electronic and physical features upon ion-implantation.

In general, the research aims focus on the following questions:

- Can it be possible to synthesize crystalline transition-metal based layered organic-inorganic hybrid materials with useful electronic properties?
- Can single-crystals of such hybrids be doped with alkali-metal atoms using ion-implantation and would it be possible to locate the intercalants using single-crystal X-ray diffraction?
- Does the vibrational-modes of host material change with doping and can this be related to the electronic properties of the materials?
- Does ion-implantation effect the physical properties of such hybrids as well?
- What would be the effects of introducing different transition-metal atoms within the inorganic oxide layer on the structure, chemical and physical properties of overall hybrid framework?
- Does changing the organic ligands affect the physical, chemical and structural properties of the material?
- Would it be possible to synthesize mixed-valent hybrid materials at ambient pressure?

Various experiments were performed to answer the above questions. The following work presents the results of these experiments.

## Chapter 2

### Experimental Techniques

This chapter describes the basic fundamentals of the experimental techniques that were employed to prepare and characterize materials involved during this study. The first section describes the synthesis technique that was used to prepare crystalline hybrid materials. Section two comprises basic details of ion-implantation that was used as a doping technique. Different experimental techniques that were used to characterize these materials comprise remainder of the chapter.

#### 2.1 Hydrothermal Synthesis

Hydrothermal synthesis is a well-established technique for crystallizing various substances at moderate temperature and high pressure.<sup>85</sup> The term “hydrothermal” generally refers to the presence of aqueous solvents under high temperature and pressure conditions in a heterogeneous reaction.<sup>86</sup> More specifically, hydrothermal synthesis can be defined as a method to prepare single crystals by dissolving the reaction precursors, which are insoluble under ordinary conditions, in aqueous media under moderate temperature and pressure.<sup>86</sup> Hydrothermal synthesis can be used to form novel structures from relatively insoluble and unreactive precursors. Hydrothermal reactions are combined in varying molar-ratios and fill volumes, and are typically carried out under autogenous pressure in teflon-lined steel autoclaves (Fig. 2.1) at temperature range 120-240 °C. Under these conditions, there is a considerable decrease in the viscosity of water which enhances the diffusion process and exploits the self-assembly of soluble precursors thus favouring the crystals growth.<sup>70</sup>



**Figure 2.1** A stainless steel Teflon-lined autoclave used for synthesizing hybrid materials.

Depending on the nature of reaction precursors three methods are commonly employed for crystallization using hydrothermal techniques.<sup>85</sup> First one is temperature-difference method which is most extensively used in hydrothermal synthesis for crystal growing. In this method, autoclaves are filled with a specific amount of solvents while precursors lie in the lower part of the vessel. Heating creates two temperature zones within the autoclave where precursors are dissolved in the hotter zone and are transported to the upper part by convection while cooler solution in the upper part of autoclave descends. This makes the solution supersaturated and sets up crystallization. Temperature gradient is not required in growing crystals by temperature-reduction technique. In this method, supersaturation is achieved by a gradual decrease in the temperature of solution in autoclave. This method provides a control on the crystal size where larger sized crystals can be obtained by slow decrease in temperature. Third method is known as metastable-phase technique and is used for crystallization when there is a difference in solubility between the phase of starting materials and phase to be grown. The starting materials are generally thermodynamically unstable which results in a solubility difference between stable and metastable phases and crystallization sets in after the dissolution of metastable phase.

Hydrothermal synthesis was initially used for crystallization of inorganic compounds. First example of hydrothermally synthesized single-crystals comes from Robert Bunson in

1839 when he grew barium and strontium carbonate single-crystals at 200 °C and at pressure above 100 bar.<sup>85</sup> Other early reports of hydrothermal growth of single-crystals involve production of microscopic and macroscopic crystals by de Sénarmont (1851) and G. Spezzia (1905) respectively, synthesis of large quartz single-crystals by Nacken (1946) and hydrothermal synthesis of zeolites by Barrer (1961).<sup>87-89</sup> More recently, hydrothermal synthesis has become a well established technique for preparing single-crystals of different types of materials such as fluorides, chlorides, transition metal oxides, polyoxometalates and hybrid organic-inorganic materials.<sup>69,84,90,91</sup> In addition to preparing single-crystals, hydrothermal synthesis can also be used to prepare thick/thin films in temperature range 25-200 °C and pressure <1.5 MP.<sup>92</sup> Few advantages of hydrothermal synthesis as compared to other synthetic techniques for preparation of single-crystals are listed below<sup>92</sup>

- Due to mild reaction conditions, hydrothermal synthesis is considered as environment friendlier as compared to other synthetic techniques that require elevated temperatures and higher/lower pressures to take place.
- Gels, powders, single-crystals, coatings, thick and thin films can be prepared using hydrothermal conditions.
- Hydrothermal synthesis allows in-situ fabrication of different ceramic materials and provides excellent control on chemical composition, stoichiometry, rate and uniformity of nucleation and crystal dimensions.
- Hydrothermal synthesis incurs lower costs as compared to other synthetic procedures.
- Hydrothermal synthesis can be combined with other chemical processes such as electrochemical, mechanical and microwave techniques.

## **2.2 Ion-Implantation**

Chemical reactions are carried out to prepare new materials and even to optimize chemical and physical properties of existing materials. But sometimes these reactions are accompanied by undesirable effects arising from diffusion, precipitation, segregation and solid solubility which hamper some of the properties of the materials. These limitations can be overcome by ion implantation which is one of the simplest and most direct methods of controlling the structural, electronic and physical properties by injecting ions into a material.<sup>93</sup> Ion-implantation is a process where electrostatically accelerated ions with high energies, typically between 10 keV to 500 keV, are bombarded onto a target material. Implanted ions lose their

energy as a result of collisions with atoms of the host material and come to complete rest within few femtoseconds.<sup>94</sup> The penetration depth of implanted species can be determined by the energy and fluence (ions/cm<sup>2</sup>) of the incident beam, and the nature of target material. The average penetration depth can be between 0.1-1.0  $\mu\text{m}$ .<sup>95</sup> This makes ion implantation especially useful for modifying surface properties of a material. With modern state-of-the-art instruments, it is possible to dope almost any element of the periodic table with great precision. Major advantages of ion implantation include very precise control of the concentration of implanted ions, almost no constraints on choice of the implanted ions, control of the penetration of implanted species, possibilities of implanting different ions at different depths without perturbing other impurities and choice of selected area doping by masking the rest of material.<sup>94</sup> In order to better understand the physics behind ion-implantation, it is important to know the design of the ion-implanter and general principle of ion implantation.

### 2.2.1 Ion Implantation Process

A typical ion-implanter consists of a vacuum chamber, a low pressure plasma ion source, bending magnets and a target chamber as shown in Fig. 2.2. Ions generated from a plasma source are passed through a mass-analysing magnet which selects the ions of the desired mass. Ion selection is based on the simple concept of centrifugal force  $\mathbf{F}$  acting on a particle, having mass  $m$  and charge  $q$ , moving with velocity  $\mathbf{v}$  in a magnetic field  $\mathbf{B}$

$$|\mathbf{F}| = |q(\mathbf{v} \times \mathbf{B})| = m|\mathbf{v}^2| = qV$$

Thus ions of desired charge and mass can be selected by adjusting the magnetic field. These ions are then accelerated and directed towards the target.<sup>96</sup>

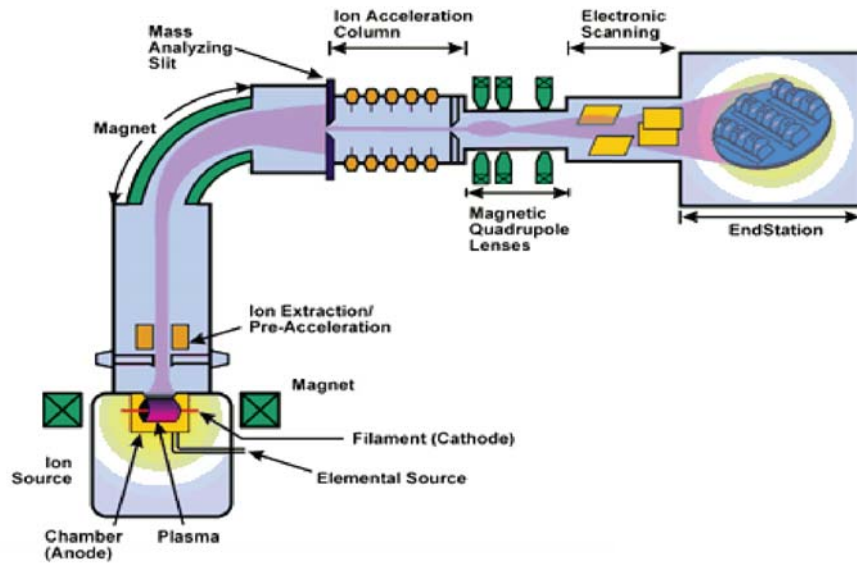


Figure 2.2 Schematics of a typical ion-implanter.<sup>97</sup>

When highly energetic ions are incident on target surface there is rapid energy transfer between the incident ions and the atoms of target material. The resulting interaction between implanted species and host atoms could be of three types: disorder in the original structure known as radiation damage, removal of the target atoms by ion-bombardment known as sputtering, and deposition of implanted species known as doping.<sup>94</sup> The energy transfer occurs by two mechanisms: nuclear stopping where incident ions are decelerated as they collide with the lattice atoms and electronic stopping where incident ions slow down and eventually come to stop as a result of the interaction with an electron cloud. Therefore the stopping power  $S$ , which corresponds to energy loss per unit ion path can be defined as

$$S = \left(\frac{dE}{dx}\right)_{nuclear} + \left(\frac{dE}{dx}\right)_{electronic} = S_n + S_e$$

The Linhard solution to nuclear stopping for an ion with atomic number  $Z_1$  and mass  $M_1$  colliding with a target material of atomic number  $Z_2$  and mass  $M_2$  can be approximated as

$$S = 2.8 \times 10^{-12} \frac{Z_1 Z_2}{Z} \frac{M_1}{(M_1 + M_2)} eV cm^2$$

Where  $Z$  is the reduced atomic number,  $Z = (Z_1^{2/3} + Z_2^{2/3})^{3/2}$ .

Thus energy loss due to nuclear collision is independent of energy of incident ions. While electronic stopping is directly proportional to the square root of energy and can be approximated as<sup>96</sup>

$$S_e = 3.3 \times 10^{-17} (Z_1 + Z_2) \sqrt{\frac{E}{M_1}} eV cm^2$$

Many theoretical models have been proposed in recent years to understand the ion/target-collision processes and hence predict the ion distribution in the target, the distribution of radiation damage and lateral spreading of ion beam. The full description of these models involves complex mathematical expressions. The derivation of these numerical expressions is in the literature.<sup>98</sup>

Ion implantation processes can be simulated by semi-analytical and Monte-Carlo (MC) methods. However, increasing requirements of accuracy due to continued downscaling of device dimensions has made MC methods a preferred choice for simulating ion-implantation. MC simulations have many advantages over analytical methods in a sense that they can accurately predict ion ranges, doping profiles for complex devices, and radiation damage.<sup>96</sup> There are many groups of computer programmes that are used as MC simulators for ion implantation. SRIM (The Stopping and Range of Ions in Matter) is one of the most widely used groups of computer programmes that are based on MC simulation method.<sup>99</sup> SRIM uses quantum mechanical treatments such as binary collision approximation (ion-atom collision) to calculate stopping range and range of ions that are introduced to a target material during ion-implantation process.<sup>100</sup> The input for TRIM (the Transport of Ions in Matter), which makes the core of SRIM, includes target orientation (which could be complex targets of up to eight layers each of different materials), ion species, dopant concentration and energy of incident ion beam. With TRIM, it is possible to calculate almost all the kinetic phenomena associated with ion implantation such as 3D distribution of ions, target damage and sputtering.<sup>100</sup>



**Figure 2.3** A low energy ion-implanter at GNS Sciences, Lower Hutt was used for doping metal atoms into single crystals and thick films.

### **2.2.2 Ion-Implantation Applications**

Ion implantation has been used to modify the physical and electrical properties of semiconductors since 1960s.<sup>101</sup> Different reviews have been written that demonstrate the progress in ion-implantation following the first successful low-dose doping of CMOS (Complementary Metal–Oxide–Semiconductor).<sup>102,103</sup> Developments in the ion-implantation technology lead to high-dose doping and device fabrication. One particular early example is the synthesis of MOST (Metal–Oxide–Semiconductor–Transistor) that demonstrates the advantage of concentration and depth control of the impurities.<sup>104</sup> The ability of ion-implantation to form high concentration of impurities with very thin layers has contributed to the development of integrated circuit design such that very abrupt termination of the dopant region minimizes the accumulation of minority carriers. Reference (104) is a detailed review summarising the role of ion-implantation in integrated circuit technology.<sup>105</sup> Ion implantation is also used to dope different metal ions in the compound semiconductors. Numerous successful devices based on compound semiconductors such as III-V and II-VI have been fabricated using ion-implantation.<sup>106,107</sup>

For metals, the use of ion-implantation has been directed towards solving problems such as corrosion, wear, friction etc.<sup>94</sup> However, more recently, metal (Fe, Au, Ni etc.)-carbon nanocomposite thin films have been prepared by ion beam deposition.<sup>108</sup> These systems demonstrate excellent magnetic properties that can be modified by ion beam sputtering. It is also possible to synthesize magnetic nanoclusters of suitable metal nanoparticles into a suitable host lattice. For example, when Fe was implanted into a ZnO host matrix, formation of magnetic nanoassemblies with Curie temperature below room temperature were observed.<sup>109</sup>

Ion implantation also finds applications in superconductors where it is possible to induce superconductivity in covalently bonded semiconductors by low-energy ion implantation.<sup>110</sup> Pioneering examples include boron-doped synthetic diamond with a superconducting transition temperature  $T_c = 4$  K, heavily-doped (nearly 8 %) Si with a much lower transition temperature of  $T_c = 0.4$  K, and boron-doped SiC with a similar transition temperature.<sup>111-113</sup> More recently surface superconductivity has been reported in SrFe<sub>2</sub>As<sub>2</sub> systems after Ca<sup>2+</sup> and K<sup>+</sup> ion implantation.<sup>114</sup>

## 2.3 Characterization Techniques

### 2.3.1 X-ray Diffraction

X-ray diffraction (herein “XRD”) is an analytical technique that is used to structurally characterize powdered or crystalline samples. XRD was discovered in 1912 by Max von Laue when he demonstrated that crystalline substances can act as three dimensional gratings for X-rays.<sup>115,116</sup> Typical in-house X-ray diffractometers consist of three basic components: an X-ray generator, a sample holder and a detector (Fig. 2.4). In a rotating anode X-ray generator, electrons are accelerated by high electric fields and directed towards the metal anode (Cu, Co or Mo). When electrons bombarding the target gain sufficient energy of about 10,000 eV (threshold potentials) they become capable of dislodging electrons from the innermost (K) shell.<sup>115</sup> The vacancy thus created in the K shell is filled by the descent of an electron from a higher energy (L) or (M) shell. The decrease in potential energy in going from higher to lower shell appears as radiation known as X-rays. After passing through a monochromator the resulting radiation is restricted to radiation of a single wavelength. These X-rays are then collimated and directed onto the sample.<sup>115</sup>

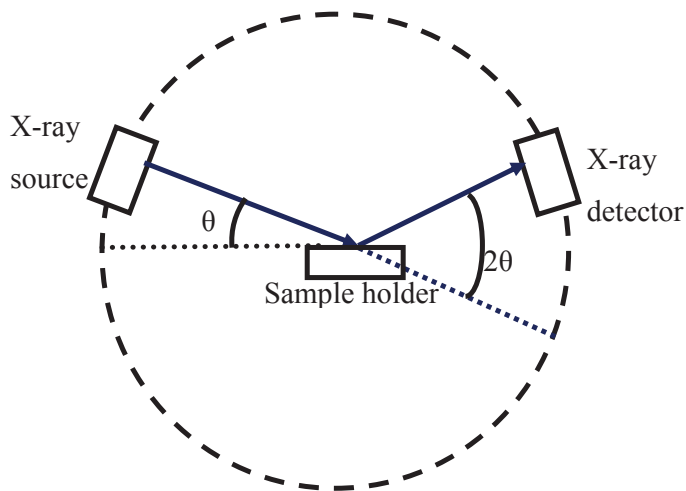


**Figure 2.4** A simplified sketch of the X-ray diffractometer.

When an X-ray beam interacts with a crystalline sample (regular arrays of atoms), a part of it is transmitted and a part of it is scattered by electrons. Since the wavelength and frequency of these scattered X-rays are identical to those of the incident beam, the electrons are therefore considered as secondary sources emitting X-rays.<sup>116</sup> In general, the scattered X-rays travel in all directions but in certain directions the scattered waves recombine in phase to produce a wave with larger amplitude – constructive interference. Now to visualize the situation consider two parallel X-rays from a monochromatic source are scattered from the two adjacent planes of atoms within a crystal (Fig. 2.5).

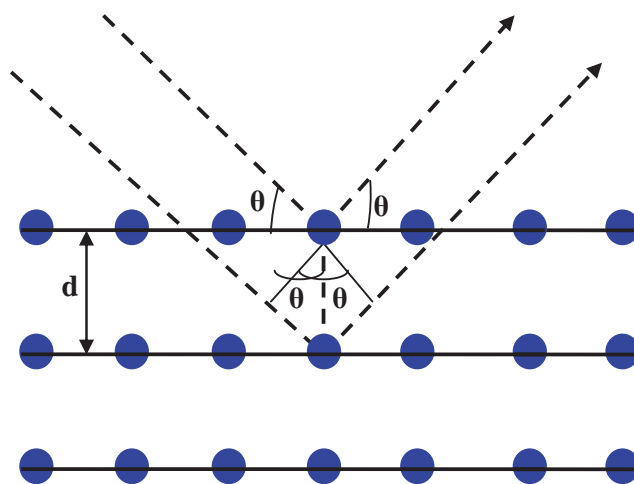


**Figure 2.5** A pictorial illustration of Bragg's law.

Constructive interference will only occur when the total path difference between the scattered waves is an integral multiple of wavelengths.

$$\text{Total path difference} = 2d\sin\theta \quad (2.1)$$

For constructive interference

$$n\lambda = 2d\sin\theta \quad (2.2)$$

Where  $d$  is the spacing between atomic planes,  $\theta$  is the glancing angle,  $n$  is an integer and  $\lambda$  is wavelength. Eq. (2.2) is known as Bragg's law.

It's noteworthy that in the derivation of Bragg's law, electron density is assumed to be lying in the planes. However, in actual crystal structures electron density doesn't lie on fixed planes and is distributed throughout the unit cell. Now since it can be shown that waves scattered from electron density may be added to give a resultant as if reflected from the plane, the derivation of Bragg's law remains valid.<sup>115</sup>

Depending on the sample state (powder, crystalline or polycrystalline) and information needed, following two types of XRD is practiced for structural characterization.

### **Single-crystal X-ray Diffraction**

Single-crystal XRD provides simplest demonstration of Bragg's law. In single-crystal XRD two types of experiments can be performed

- Wavelength is fixed and crystal is rotated to obtain  $d$  – Bragg monochromatic diffraction.
- Crystal is fixed and wavelength is varied to obtain  $d$  – Laue polychromatic diffraction.

Laue diffraction is a one-shot experiment and requires only few seconds of X-ray exposure to obtain the complete dataset. This method works best for protein crystallography. However it comes with the problems of intensity corrections.

Bragg diffraction is more commonly used because the diffraction patterns are easy to interpret but data collection takes much longer time than Laue diffraction. At first, a crystal is centred in the X-ray beam and preliminary rotational images are collected for screening the sample quality. Once a suitable crystal is found, an automated collection routine is set for unit cell determination. The resulting reflections are auto-indexed to obtain the reduced cell which

is refined using least-square methods to obtain appropriate crystal system and Bravais lattice. Depending upon the sample quality and primitive unit cell, a scan incremental method is used for intensity data collection where the frame increments and exposure times determine the duration of data collection. For high symmetric molecules, data collection time can be reduced by applying symmetry constrains. Once the data collection is completed, integration process is applied to reduce the raw frame data to a smaller set of integrated intensities. Solution of phase-problem is then obtained by applying least-square methods. This leads to preliminary electron density map where elements can be assigned – higher elements are associated to higher intensities. Structure solution is completed by assigning the distances and angles between intensity centres to the most likely coordination. In order to obtain a fit between observed and calculated crystal structure, solved structure is refined using least-square methods.

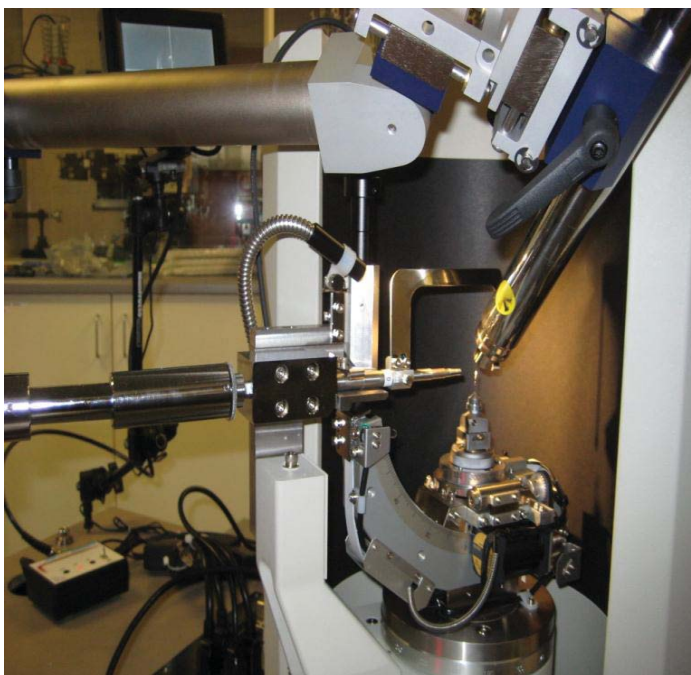


**Figure 2.6** The Rigaku spider diffractometer at Massey University, Palmerston North that was used for structural characterization of crystalline materials.

### **Advantages**

- Non-destructive
- Gives detailed information about the crystal structure including bond lengths and angles, and unit cell dimensions

- Possible to obtain crystal structures of high-temperature/high-pressure phases
- Powder patterns can be calculated

### **Limitations**

- Requires a single crystal
- Long times required for data collection (1–72 hours)

### **Powder X-ray Diffraction**

Powder XRD is primarily used for determining average bulk composition and phase identification of powdered samples.<sup>117</sup> It can also provide information about unit cell dimensions. In single-crystal XRD there is only one crystal that is used for data collection therefore only few reflections are recorded in the diffraction pattern. Powder XRD is performed on polycrystalline samples that offer nearly all the possible orientations of crystals thus resulting in diffraction rings rather than spots. Results from the data collection are commonly represented in the form of a plot containing peak positions ( $2\theta$ ) and X-ray counts (intensity). The position of a diffraction peak is completely independent of the position of atoms within the unit cell and is determined by the symmetry and size of unit cell. Each peak represents a certain lattice plane and is characterized by Miller indices – a notation system representing atomic planes in the crystals. In order to determine the unit cell, all the peaks in the diffraction pattern must be indexed with specific Miller indices.

### **Advantages**

- Rapid data collections times
- Can be used to identify unknown material.
- Minimal sample preparation is required.

### **Limitations**

- Homogenous sample is required for good results.
- Identification/quantification of multiphase materials can be difficult.



**Figure 2.7** A powder X-ray diffractometer at Industrial Research, Lower Hutt was used for preliminary structural characterization of polycrystalline hybrid materials.

### 2.3.2 X-ray Photoelectron Spectroscopy

X-ray photoelectron spectroscopy (herein “XPS”) is a quantitative surface analysis technique that is used to determine surface chemical composition, empirical formula and electronic states of elements present in the sample.<sup>118</sup> In XPS, a sample is bombarded with photons with low energies (1.5 keV) to initiate the photoelectric effect. The emitted photoelectrons are detected by a high resolution spectrometer. XPS is a very sensitive technique and can probe only few nanometres (1-10 nm) within the surface. Therefore, XPS requires high vacuum ( $1.33 \times 10^{-8}$  Pa) for sample analysis which is crucial not only for the transmission of photoelectrons to the analyzing chamber but also avoids contamination of the sample.

In 1907, the first XPS spectrum was recorded by P.D. Innes who used photographic plates to record the broad bands of electrons (as a function of velocity) that were emitted as a consequence of their absorption of X-ray radiation.<sup>119</sup> Different scientists worked through 1910–1930 to seek a detailed explanation of these broad bands.<sup>120,121</sup> The first high resolution

XPS spectra was recorded by K. Siegbahn in 1954, who later in 1967 brought electron spectroscopy for chemical analysis (ESCA) to recognition.<sup>122</sup>

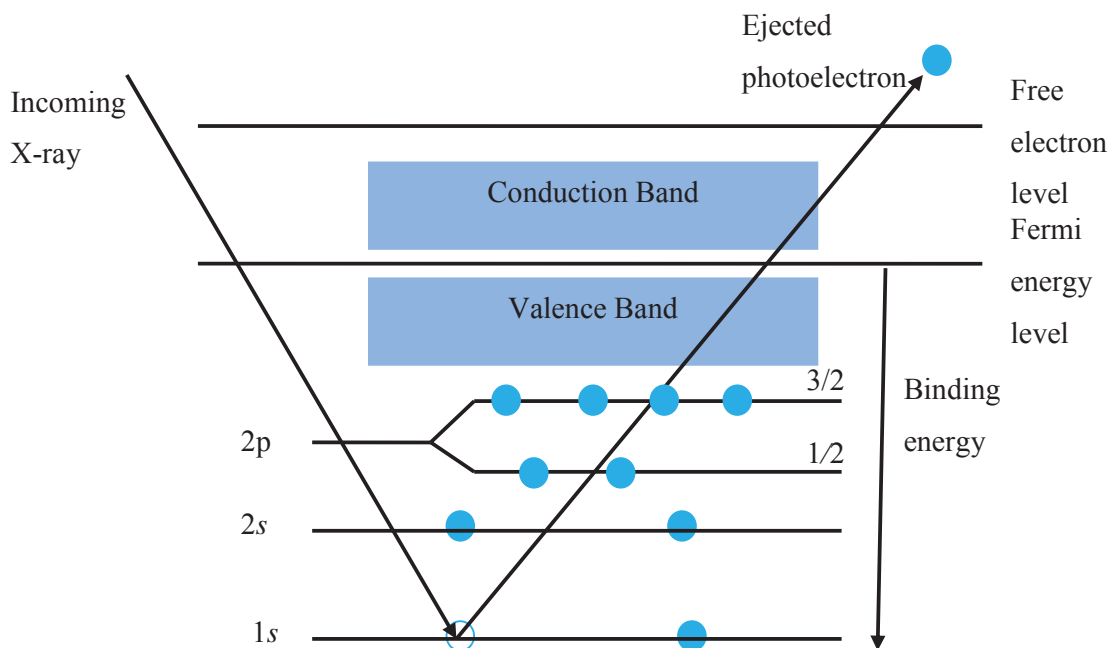


**Figure 2.8** An explanation of basic principle of XPS.

The basic principle of XPS is derived from photoelectric phenomena, where a sample surface is bombarded with X-ray photons ( $h\nu$ ).<sup>118</sup> These photons are absorbed by the atoms (with initial energy  $E_i$ ) and result in the subsequent emission of electrons. The total energy of the system after this process is a sum of kinetic energy of emitted photon ( $E_k$ ) and energy of target atom in the final state ( $E_f$ ).

$$h\nu + E_i = E_k + E_f \quad (2.3)$$

$$h\nu - E_k = E_f - E_i \quad (2.4)$$

The difference in energy between the initial and final state of target atom is known as binding energy of emitted electrons and it is characteristic of the element that it originates from. A plot between binding energies of photoelectrons and electron count makes a typical XPS spectrum. The XPS spectrum is dominated by a characteristic set of peaks that correspond to electrons originating from different orbitals within the atoms of the sample

material. Since the area under each peak is directly related to the amount of material present on the irradiated volume, therefore, before quantification of data is performed each XPS signal must be corrected by a relative sensitivity factor and normalised over all the detected elements.<sup>123</sup> Generally, two types of XPS spectra are recorded: survey scans are recorded with the largest pass energy where the resulting spectrum displays XPS peaks corresponding to all the materials present on the surface. Individual chemical shifts can be determined from high-resolution scans that are recorded with very low energies (10-20 eV).<sup>118</sup> Over the years XPS has been used for the following tasks:

- Detection of unknown elements on surface of material being analysed. XPS can detect all the elements except H or Li ( $Z=2$ ).
- Determination of empirical formulae.
- Detection of dopant species even in very small quantities.
- Determining the electronic and chemical states of surface elements.



**Figure 2.9** The Kratos Axis UltraDLD surface-analyzing chamber at the University of Auckland that was used for XPS measurements.

### 2.3.3 Raman Spectroscopy

Raman spectroscopy is an inelastic scattering technique that uses monochromatic light to study rotational, vibrational and other low frequency modes in a system.<sup>124</sup> The technique was discovered in 1928 by C.V. Raman who used a telescope and a specific arrangement of lenses to converge and focus the sunlight to a liquid sample.<sup>125</sup> A system of optical filters was used to show the presence of scattered radiation with altered frequency.

In Raman scattering a sample is illuminated by laser light which distorts electron clouds to form short-lived states known as virtual states. Now if only the deformation of electron clouds occurs then owing to the small mass of electrons photons will be scattered with very small change of frequency (or a no change at all) – Rayleigh scattering.<sup>126</sup> However, if a change in molecular polarization potential takes place then energy will be either transferred from photon to the molecule or vice versa. This leads to inelastic scattering of light – Raman scattering.<sup>124-126</sup> Raman scattering is a very weak process and the intensity of a strong Raman signal is only about one thousandth of the intensity of Rayleigh scattering.<sup>124</sup> The basic process is shown in Fig. 2.10.

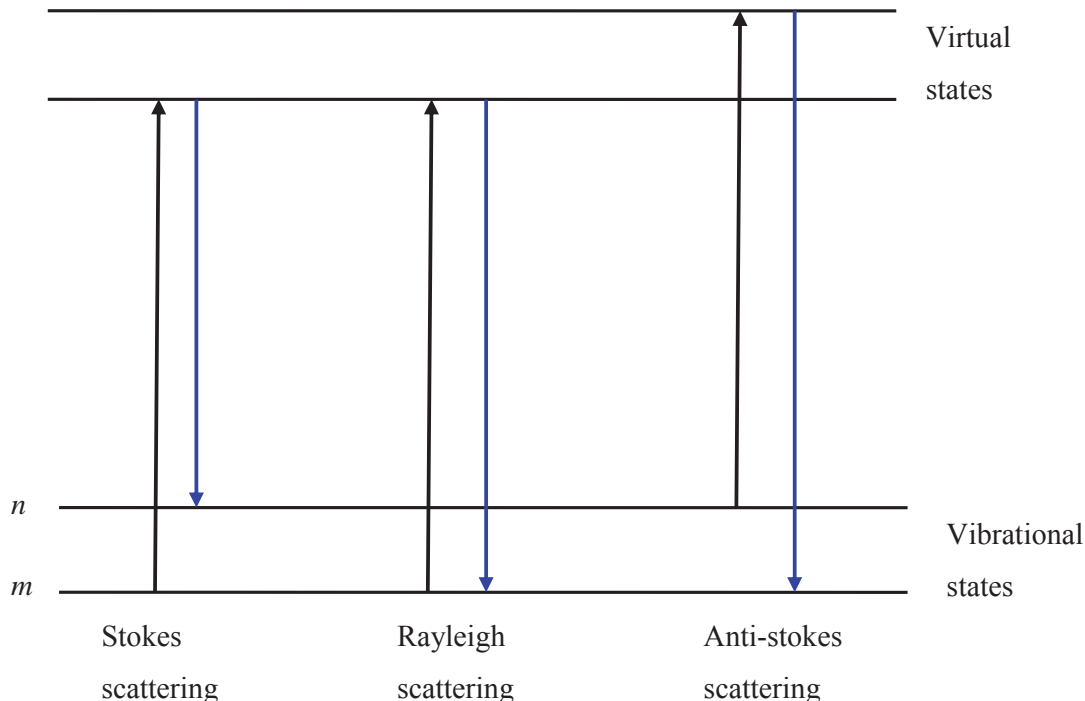


**Figure 2.10** Different light scattering techniques.

The Raman effect can be explained by a simple classical treatment as follows:<sup>126</sup>  
 Consider a photon beam with frequency  $\nu_0$  accompanied by an oscillating electric field E:

$$E = E_0 \cos 2\pi\nu_0 t \quad (2.3)$$

which interacts with an electron cloud to induce a dipole

$$P = \alpha E \quad (2.4)$$

where  $\alpha$  is the polarizability of the molecule. An interaction between polarizability and normal vibrational modes (Q) will lead to the Raman effect. For a non-linear molecule with N atoms there will be 3N-6 vibrational modes. Normal modes are defined as:

$$Q = Q_j^0 \cos 2\pi\nu_j t \quad (2.5)$$

where  $\nu_j$  is the harmonic frequency of the jth normal mode.

For a vibrating molecule, the polarizability term is given by the following Taylor expansion

$$\alpha = \alpha_0 + \frac{1}{2} \left[ \frac{\partial \alpha}{\partial Q_j} \right] + Q_j + \dots \quad (2.6)$$

Substituting (2.3), (2.5) and (2.6) in (2.4) will get to

$$P = \alpha_0 E_0 \cos 2\pi\nu_0 t + \frac{1}{2} \left[ \frac{\partial \alpha}{\partial Q_j} \right] E_0 Q_j^0 [\cos\{2\pi(\nu_0 + \nu_j)t\} + \cos\{2\pi(\nu_0 - \nu_j)t\}] \quad (2.7)$$

The first term in the above equation represents Rayleigh scattering and it has same frequency as the incident radiation. The second  $(\nu_0 + \nu_j)$  and third  $(\nu_0 - \nu_j)$  terms represents anti-stokes and stokes Raman scattering respectively.<sup>126</sup> Stokes scattering occurs when the energy absorbed by a molecule from its ground vibrational state  $m$  lifts it to the higher energy state  $n$ . The photon emitted by the molecule on its descent from the excited state will therefore have less energy than the absorbed one. Due to thermal agitation, some molecules already reside in the excited state  $n$  and scattering from this state to the lower energy state  $m$  is known as anti-stokes scattering. In this case the emitted photon will have a higher energy than the absorbed photon.<sup>127</sup> The intensities of stokes and anti-stokes scattering

differ but depend on the initial state of the molecule. In case of thermal equilibrium where most of the molecules are at low energy levels Stokes scattering will be dominant.

Whenever there is an interaction between matter and energy there are certain transitions between atomic or molecular level that take place. The possibility of occurring any transition depends upon physical structure of the molecule and many other properties. These transitions are governed by selection rules and each spectrum has its own selection rule. A specific transition will be Raman active only if there is a change in polarizability of molecule upon interaction with light while a transition will be Infrared active if there is a change in dipole moment of the molecule upon interaction with light.<sup>128</sup>

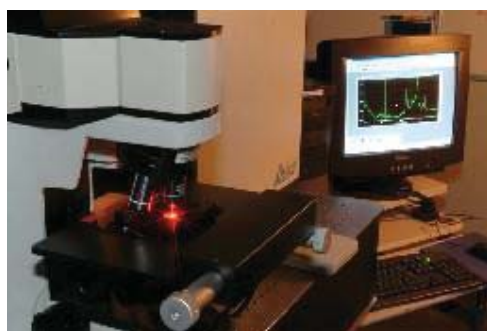


**Figure 2.11** The LabRam instrument at Victoria University, Wellington was used for solid-state Raman measurements.

Raman spectroscopy can be applied to investigate the bulk structure of hybrid materials and can provide very useful information about the chemical and physical properties of the reaction components and products. In the past, Raman spectroscopy has been used to identify the purity of transition metal oxides as well as to determine the influence of incorporating ligands, with different lengths and bonding preferences, on overall structure of the hybrid organic-inorganic frameworks.<sup>74</sup> The effect of doping hybrid materials with metal atoms can also be investigated by Raman measurements where a difference in the Raman peak shape and/or new phonon-modes in the spectra of intercalated materials can appear as a result of doping.<sup>91,129</sup> A literature review suggests that Raman spectroscopy should provide information about the following three aspects of ligand-metal interaction within the hybrid framework:<sup>74,126,127,130-136</sup> (1) the presence of organic ligands in the structure, (2) the extent of structural modifications that occur when different ligands are incorporated in similar frameworks, (3) the existence of different

coordination environments offered by inorganic molecules for ligand attachment.

### 2.3.4. Magnetic Measurements

For magnetic characterization superconducting quantum interference device (SQUID) is used. SQUID is a very sensitive magnetometer and can detect magnetic fields as low as  $5 \times 10^{-18}$  T.<sup>137</sup> The basic principle of SQUID is derived from Josephson effect named after Brian Josephson who, in 1962, predicted the tunnelling of Cooper-pairs from superconductors through a thin insulating junction. The effect was later confirmed and it led to the manufacturing of Josephson junctions – essential components of most of the present magnetic characterization devices.<sup>138</sup> There are two types of SQUIDs: DC SQUID and RF SQUID. DC SQUID was invented in 1964 and is basically a ring of a ceramic superconducting material (niobium, lead alloy, nickel or even high-temperature superconductors) containing two Josephson junctions known as weak links.<sup>139-141</sup> The device is biased with a dc current and is read out at low frequencies. When a current is made to flow through a superconducting loop in the absence of an external magnetic field, electrons tunnel through the two junctions. As a result input current splits equally in two parts. Now when a small magnetic field is applied, it creates a phase difference between electrons and affects the current flow through the loop. The resulting magnetic flux induces a current around the loop. This affects the current through the loop because the net current through each junction is no longer the same. This creates a potential difference around the loop which can be measured.<sup>140-143</sup>

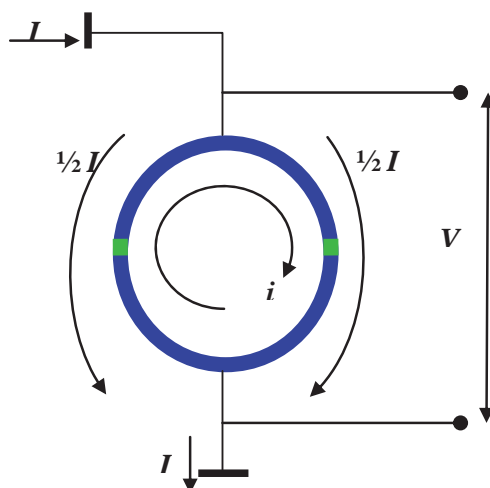


**Figure 2.12** A simplified schematic representation of DC SQUID operation. Green stripes represent Josephson junctions.

RF SQUID, also known as AC SQUID, was invented in 1965 and incorporates one Josephson junction. It is biased with a radiofrequency current and is read out at high frequencies.<sup>140</sup>

The precision and sensitivity of SQUID finds applications in many scientific fields.<sup>143</sup> For example, several groups have reported the use of SQUID to determine the presence of antigens labelled with magnetic markers. Microstrip SQUID amplifiers are used as intermediate frequency amplifiers to follow a superconductor-insulator-superconductor mixer for radio astronomy. The high sensitivity of SQUIDS to magnetic fields has been exploited by various other experimental techniques such as NMR (nuclear magnetic resonance), MRI (magnetic resonance imaging) and scanning SQUID microscopes. However, perhaps the most common commercial use of SQUID is in magnetic property measurement system (MPMS) which are used for physical characterization of magnetic materials. These instruments were first introduced in 1983 and are capable of measuring magnetic fields of up to 7 T.<sup>144</sup> The model MPMS systems are used to detect magnetic moment of a sample from which magnetic susceptibility and magnetization can be determined. Major components of these systems include

**Temperature Control System** – Provides precise control for sample temperature in the range 2 K to 400 K. Such a low sample temperature is achieved by immersing sample into a vacuum-sealed container of liquid helium.

**Magnetic Control System** – Magnetic fields in the range -7 to +7 T are provided by current from a power supply.

**Sample Holding System** – Capable of rotating the sample through detection coils with without transmitting undue mechanical vibrations to SQUID.

**Computer Operating System** – Provides automated diagnostic controls to almost all the features of MPMS.

**Superconducting SQUID Amplifier System** – The heart of the MPMS. It is used for magnetic moment detection and provides reset circuitry, second-derivative sample-coil array and auto-ranging capability.

Although the sensitivity of a SQUID to magnetic fields is remarkable, in MPMS systems it doesn't directly detect magnetic fields but rather works as an efficient current-to-voltage converter. A sample is moved through superconducting detection coils which are located outside the sample chamber and are connected to the SQUID by superconducting

wires. The movement of sample induces electric current which is detected by SQUID sensor.

The SQUID electronics then produce output voltage which is directly proportional to the current flowing in the input coil. When a system is fully calibrated, variations in the current detection coils produce corresponding variations in the output voltage which are directly proportional to the magnetic moment. <sup>144</sup>



**Figure 2.13** A Quantum Design MPMS XL SQUID at Industrial Research Ltd. was used for magnetic characterization.

## Chapter 3

### **Synthesis, structure and physical properties of Na<sup>+</sup> - intercalated WO<sub>3</sub> (4,4'-bipyridyl)<sub>0.5</sub> hybrid material**

This chapter describes the synthesis, structure and physical properties of WO<sub>3</sub>(4,4'-bipyridyl)<sub>0.5</sub> (here in “WO<sub>3</sub>-bpy”) layered hybrid materials. A detailed structural analysis of these materials before and after ion-implantation is presented. Fabrication of thick polymer-bound films of WO<sub>3</sub>-bpy is also presented followed by results from Raman and magnetic measurements.

#### **3.1 Introduction**

Organic-inorganic hybrid materials offer a rich variety of structures and electronic properties with the attractive feature of synthesis at near-ambient conditions. They can also provide access to a class of low-dimensional electronic materials where the inorganic component forms an extended layer framework bound by covalent or ionic (or both) interactions while the organic component provides electronic coupling between inorganic layers thus tailoring the electronic properties of the inorganic framework.<sup>145</sup> One class of these materials is based on simple two-dimensional layers of tungsten (or molybdenum) oxide separated by organic molecules which either ionically or covalently bind the layers together.<sup>70,74,84,146</sup> The structure of the tungsten oxide systems (oxo-, polyoxo-, and metastable tungsten oxides ) is based on corner-and/or edge-sharing WO<sub>6</sub> octahedra. The insertion of group I or II cations into (or deoxygenation of) WO<sub>3</sub> and WO<sub>3</sub>·nH<sub>2</sub>O leads to an insulator-to-metal transition, produces the intense colour and metallic lustre of the tungsten bronzes, and induces bulk superconductivity in, for example, Na<sub>x</sub>WO<sub>3</sub> with  $T_c = 3$  K for  $x=0.2$ .<sup>65</sup> Diffusion of Na into single crystals of WO<sub>3</sub> has even led to signatures of surface superconductivity around 91 K.<sup>83</sup> All this points towards the fact that the electronic properties of tungsten oxide based systems are quite diverse. The varied structural phases, electronic, physical and optical properties of these systems have been the subject of much research over past few decades.<sup>66,69,147</sup>

Recently a related layered hybrid material  $\text{WO}_3\text{-bpy}$  was reported<sup>71</sup>. This consists of layers of single planes of corner-shared  $\text{WO}_5\text{N}$  octahedra with the axial organo-nitrogen (bpy) and oxo ligands of each  $\text{WO}_5\text{N}$  octahedron alternating in direction, thereby binding the layers together (Fig. 3.1). The bipyridyls were reported to align along the  $[110]$  direction thus defining open structural channels in this direction.

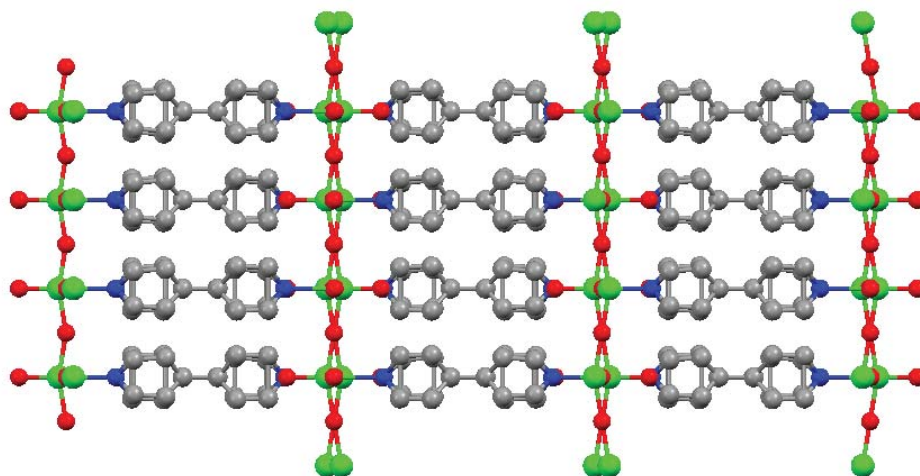


**Figure 3.1** Crystal structure of  $\text{WO}_3\text{-bpy}$ .<sup>71</sup> Layers of corner-shared tungsten oxide octahedra are bridged by bpy ligands defining open structure channels. Tungsten atoms are shown in green, oxygen in red, nitrogen in blue and carbon in grey. Hydrogen atoms are omitted for clarity. (*c*-axis is horizontal).

In a preliminary study  $\text{Na}^+$  was incorporated by aqueous electrochemistry resulting in an increase in conductivity and the appearance of  $\text{W}^{5+}$  species as evidenced by XPS.<sup>84</sup> But it was not possible (with XPS) to establish whether  $\text{Na}^+$  was incorporated in the bulk or merely at the surface. Moreover, using powder XRD no change in lattice parameter was detected, possibly suggesting the latter. To undertake single-crystal structural studies it requires an intercalation technique that allows structural determination before and after incorporation of  $\text{Na}^+$ . In an attempt to answer these questions ion-implantation is employed as a novel technique for intercalating metal atoms into single-crystals and polymer bound thick films of  $\text{WO}_3\text{-bpy}$  hybrid materials. Specifically, this chapter describes the synthesis and structural characterization of crystalline  $\text{Na}_x\text{WO}_3\text{-bpy}$  where the  $\text{Na}^+$  ions are intercalated by ion-implantation. For an in-depth understanding of the physical properties of intercalated hybrid network thick polymer bound films of  $\text{WO}_3\text{-bpy}$  were prepared and characterized by Raman and magnetic measurements.

## 3.2 Experimental Details

### 3.2.1 Synthesis

Single crystals of  $\text{WO}_3\text{-bpy}$  were synthesized via a hydrothermal reaction of  $\text{Na}_2\text{WO}_4 \cdot 2\text{H}_2\text{O}$ , bpy and  $\text{H}_2\text{O}$  using a molar ratio of 1:0.7:960 with 0.2 mL of conc. HCl per 20 ml of reactant. The reactants were kept in a sealed Teflon-lined stainless-steel autoclave reactor at  $160^\circ\text{C}$  for five days. After the autoclave was cooled for five hours to room temperature the hybrid material (in the form of fine yellow crystallites) was filtered and washed with ethanol and dried under vacuum. Crystals could even be prepared under ambient conditions but the crystallite size was smaller. The above conditions reflect the best quality of sample.

In order to measure electronic transport properties, thick films of hybrid material were coated on indium titanium oxide (herein "ITO") substrates as follows:

At first, a substrate was placed directly in the autoclave along with the reactants and heated for  $160^\circ\text{C}$  for 120 hours. This resulted in nothing but the formation of some coating on the substrate which disintegrated upon washing with ethanol. Since dissolution of coordination compounds results in the break-up of original structure of the parent material, therefore chemical solution deposition was avoided for depositing films of  $\text{WO}_3\text{-bpy}$ . At this stage, it appeared that the use of some organic binder is the only viable way of coating the substrate with hybrid material. Several polymers including polymethylmethacrylate, silver paint, polyethylene glycol, propylene carbonate, and polypropylene carbonate, *etc.* were tried in order to find the best binder. Polypropylene carbonate (ppc or QPAC) was found best for this purpose. In order to prepare the organic-binder solution many solvents were tried such as: amyl acetate, dichloromethane, ethyl acetate, THF, cyclohexane, propylene carbonate and cyclohexanone. Different concentrations of these solvents were tried at different temperatures for different amounts of time. Polypropylene carbonate was dissolved in cyclohexanone by stirring the mixtures over short intervals of time (this was done to avoid heating which results in evaporation of cyclohexanone) for a couple of days. The best coating slurry was prepared by mixing an appropriate amount of finely ground powder of hybrid material with the organic-binder solution. Thick films were then prepared by spreading the slurry with a blade spreader onto the substrate followed by vacuum drying for 30 minutes. The resulting coating is displayed in Fig. 3.2.



**Figure 3.2** Polymer bound thick film of WO<sub>3</sub>-bpy coated on ITO glass substrate.

### 3.2.2 Ion-Implantation

Sodium ions, Na<sup>+</sup>, were implanted into both faces of selected single crystals at 30 KeV using a lab-built low-energy ion implanter<sup>11</sup>. Crystal sizes were typically ~ (10-50)×(10-50)×(0.1-0.3) μm<sup>3</sup>. Samples were implanted with Na<sup>+</sup> at estimated levels of 2% and 4% of the total number of atoms in the host material based on Monte-Carlo calculations using the TRIM-DYNAMIC package.<sup>148</sup> The calculations also indicated that most of the Na<sup>+</sup> ions resided in the top 120 nm of each surface and hence have penetrated the entire sample, though a bimodal concentration profile is likely. The pale yellow crystals darken to a green hue on ion implantation (Fig. 3.3). Polymer bound films were separately implanted with Li<sup>+</sup>, Na<sup>+</sup>, K<sup>+</sup> and Ca<sup>2+</sup> ions under similar conditions to those of single crystals. Since introducing an ion would create a charge imbalance therefore it must be noted, here and elsewhere, that an electron is simultaneously injected into the original material for charge balancing purposes.

### 3.2.3 Characterization

Powder X-ray diffraction (XRD) measurements were performed with a Philips PW 1700 series powder diffractometer with Co Kα (λ = 1.789 Å) radiation. Diffraction patterns were recorded at an angle of (2θ =) 4-80°, with a total scan time of 25 minutes. Single crystal XRD patterns were recorded with a Rigaku-Spider X-ray diffractometer with wrap-around image-plate detector and three-axis kappa goniostat. A number of single crystals were selected for size and quality, polyimide microloops or micromounts, characterised by single-crystal XRD, then implanted while still mounted on the fibres and re-characterised by single-

crystal XRD. A Quantum Design MPMS XL SQUID magnetometer was used for magnetic measurements of polymer bound films. Raman measurements were performed on bulk materials using approximately 25 mW of focused 514.5 nm excitation from an Argon ion laser and a single-stage spectrograph / CCD detection system with Raman edge filters for rejection of Rayleigh scattering. The powdered samples were encapsulated in a glass vial for data collection. Raman spectra for as-prepared implanted and unimplanted films were recorded with a Jobin-Yvon LabRam Raman microscope system using excitation of 633 nm and 2–3 mW at the sample.

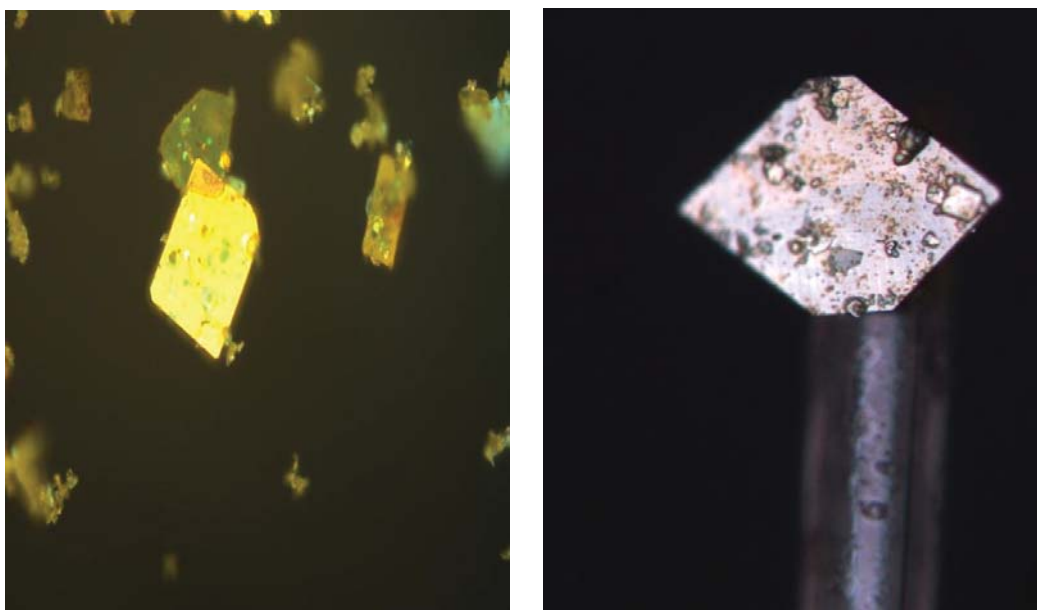


**Figure 3.3** A high-resolution snapshot of  $\text{WO}_3\text{-bpy}$  single crystal before (left) and after (right)  $\text{Na}^+$  ion-implantation.

### 3.3 X-ray Diffraction

Powder XRD was used as a preliminary tool to investigate the structure of  $\text{WO}_3\text{-bpy}$ . Measurements were performed on powdered samples as well as implanted and un-implanted thick films. Powder XRD patterns of bulk  $\text{WO}_3\text{-bpy}$  material consist of sharp  $(00l)$  reflections, where  $l = 2, 4, 6, 8, 10, 12, 14$  which are characteristic of the formation of a layered structured material (Fig. 3.4). The observed powder XRD pattern is very similar to the one calculated from single-crystal XRD measurements.

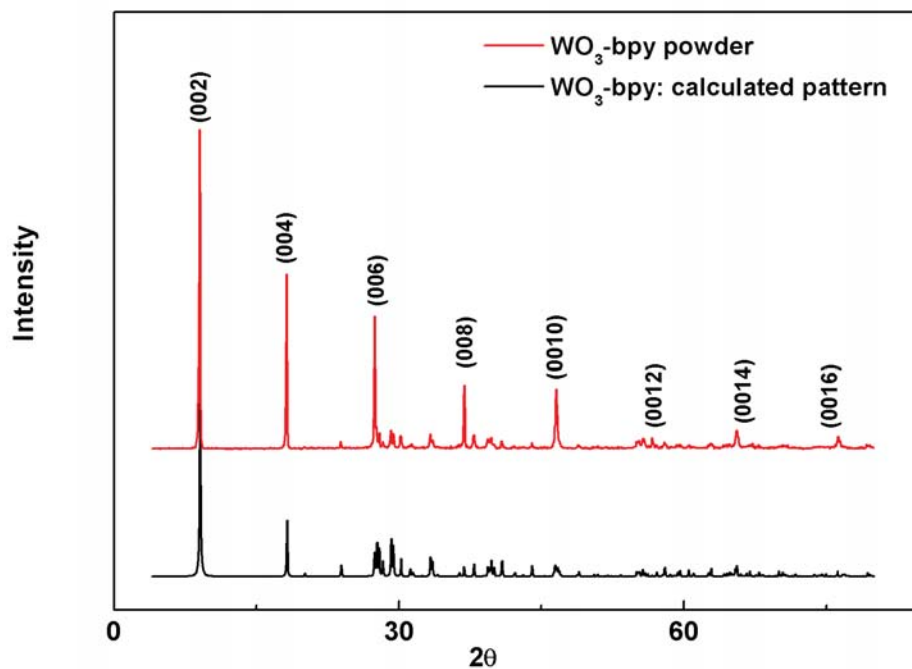


**Figure 3.4** Powder XRD patterns demonstrate strong  $00l$  reflections which indicate the formation of layered structures for both forms of  $\text{WO}_3\text{-bpy}$ : black = pattern calculated from single-crystal XRD, red = experimental pattern of  $\text{WO}_3\text{-bpy}$ . The diffraction angle is for Co  $K\alpha$  radiation. For comparison, the wavelength was changed to Co  $K\alpha$  in the pattern calculated from single crystal structure of  $\text{WO}_3\text{-bpy}$ , which was determined with Cu  $K\alpha$  radiation.

Intensity is measured in arbitrary units and Bragg angle in degrees.

Powder XRD was also used to study the stability of the layered structure over a specific temperature range. For this purpose pellets of  $\text{WO}_3\text{-bpy}$  were annealed in argon at temperatures ranging from 300 °C–540 °C at regular intervals while for cross-comparison XRD was performed after every annealing cycle. Fig 3.5 shows that powder XRD patterns remain the same for temperatures as high as 460 °C suggesting that the layered structure remains intact up to these temperatures. However, beyond 460 °C, as is obvious from XRD patterns, the layered structures start disintegrating and eventually at 540 °C only tungsten oxide species remain in the compound without any organic spacer molecule or any layered network.

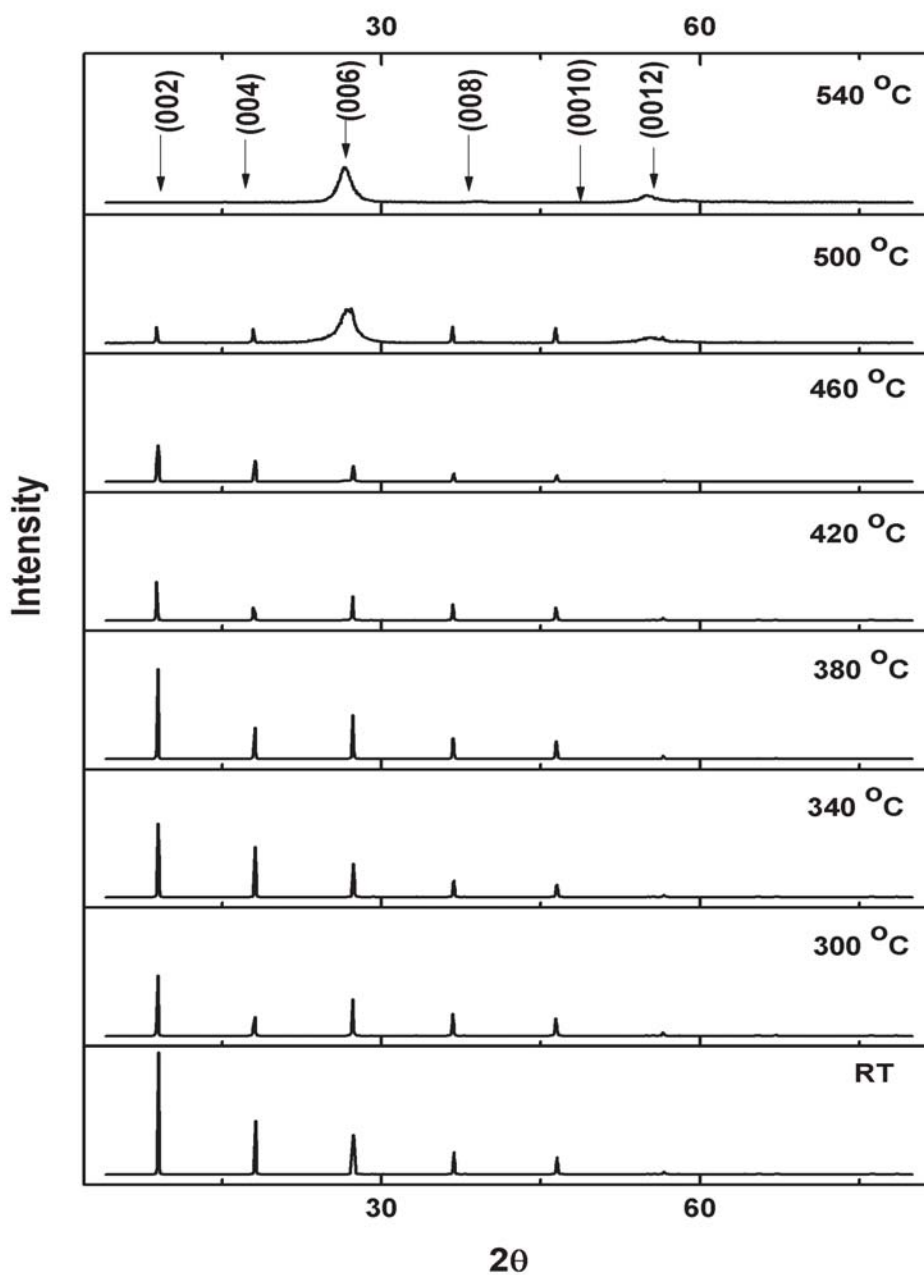


**Figure 3.5** A comparison of XRD patterns obtained from WO<sub>3</sub>-bpy pellets annealed at different temperatures. A notable decrease in intensity of all the peaks is observable as temperature increases. Beyond 460 °C, this decrease in intensity becomes significant with a clear broadening in (006) and (0012) peaks suggesting the disintegration of layered structure. Intensity is measured in arbitrary units and Bragg angle in degrees.

In order to understand the effect of ion-implantation on the  $\text{WO}_3$ -bpy structure, powder XRD was performed on polymer-bound films of  $\text{WO}_3$ -bpy before and after ion-implantation. Powder XRD has been used in the past to investigate the structural modifications induced by electrochemical insertion of ions in  $\text{WO}_3$  systems where XRD patterns change significantly after doping.<sup>84,149</sup> However, in our samples, apart from very little irregular shift in certain peak positions, no considerable change in intensity or positions of the diffraction peaks were observed after ion-implantation of  $\text{WO}_3$ -bpy thick films (Fig. 3.6). This is probably due to the fact that the implantation is contained to a depth of 150 nm only while the films are approximately 50 microns thick so that the implantation volume is effectively negligible in the powder XRD measurement. Thus, despite demonstrating that the overall structure and crystallinity of the hybrid network remains intact after ion-implantation, powder XRD patterns didn't provide conclusive evidence of intercalation of metal ions, therefore making the use of single-crystal XRD essential to determine the precise crystal structure in this particular case.

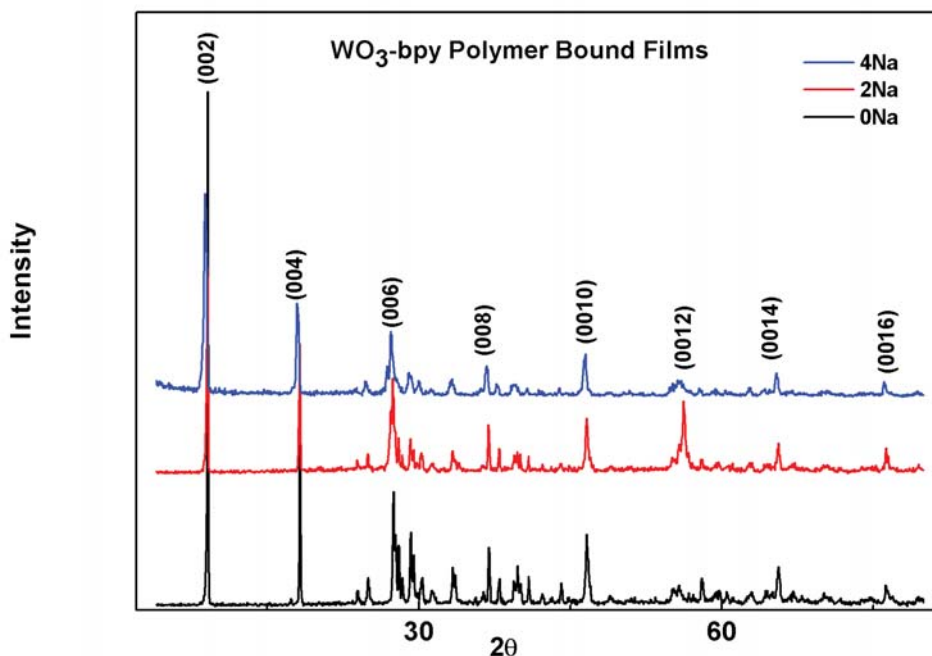


**Figure 3.6** A comparison of XRD patterns obtained from  $\text{WO}_3$ -bpy polymer bound films before and after ion-implantation. Intensity is measured in arbitrary units and Bragg angle in degrees.

In order to determine the crystal structure of  $\text{WO}_3\text{-bpy}$ , single-crystal XRD was performed before and after ion-implantation for selected single crystals thin enough to ensure complete implantation. Diffraction data for both un-implanted and implanted samples were collected at room temperature and low temperature. Since earlier data collections had established the negligible changes in crystal properties on cooling, therefore, for simplicity, detailed structural comparisons are made among the low-temperature structures (100 K) for unimplanted and 2 % implanted samples (same crystal) and the room-temperature ( $20 \pm 0.2$  °C) structure for the 4 % implanted sample (different crystal). A problem with cryo-cooling device prevented the data collection at low T for 4 % implanted sample. Key crystal and refinement parameters are summarised in Table 3.1.

Unimplanted and  $\text{Na}^+$ -implanted crystals at 293 and 100 K are isomorphous. The asymmetric unit comprises a W atom, two equatorial oxygen atoms, an axial oxygen atom and one ring of the bpy group (Fig. 3.7). Centres of inversion at the midpoint of the  $\text{C}_4\text{-C}_4'$  bond of the bpy,  $2_1$  screw axes (parallel to  $b$ ) and  $c$  glide planes generate the complete crystal structure, which comprises layers of corner-shared  $\text{WO}_6$  octahedra in the  $ab$  [001] plane, separated by bpy groups that coordinate axially to the W atoms and whose long axes are aligned approximately parallel to the  $c$  axis (Fig. 3.8). Approximately octahedral coordination of the W atoms is completed by oxo groups.

At room temperature (20 °C) and relative to unimplanted crystals,  $\text{Na}^+$  implantation led to small increases in the  $b$  and  $c$  axes and to a 0.8 % increase in unit cell volume. For the unimplanted crystal, no significant changes in unit cell dimensions and volume ( $< 0.2\%$ ) were observed between 293 K and 100 K, but for the 2%  $\text{Na}^+$ -implanted crystal, there were decreases of 0.4 % and 0.6 % in the  $a$  and  $c$  axes respectively, leading to a decrease of 0.9 % in the unit cell volume.

The axial  $\text{W}=\text{O}(\text{oxo})$  and  $\text{W}-\text{N}$  bonds of the  $\text{WO}_5\text{N}$  octahedra alternate in direction in both the  $a$  and  $b$  directions, leading to a  $\text{WO}_4$  plane which undulates in the  $ab$  plane. The bpy group and the axial oxygen atom are well ordered. The equatorial oxygen atoms are, however, stochastically disordered either side of the line joining pairs of W atoms. Residual electron density was concentrated near W atoms indicating possible unresolved disorder, concomitant with the disorder of equatorial O atoms, or a missed superstructure. No missing weak reflections were found upon close inspection of data frames, however, no attempts were made to model this disorder.

**Table 3.1** Selected X-ray crystallography details for WO<sub>3</sub>-bpy.

Parameter	(1)0 % Na <sup>+</sup>	(1)2 % Na <sup>+</sup>	(1)4 % Na <sup>+</sup>
Temperature/K	100	100	293
<i>a</i> (Å)	7.477709(13)	7.4683(3)	7.48501(14)
<i>b</i> (Å)	7.38736(13)	7.3910(3)	7.40943(15)
<i>c</i> (Å)	22.5625(4)	22.5781(6)	22.6257(4)
$\alpha, \beta, \gamma$ (°)	90, 90, 90	90, 90, 90	90, 90, 90
<i>V</i> (Å <sup>3</sup> )	1245.97(5)	1246.27(8)	1254.81(4)
Crystal system	Orthorhom.	Orthorhom.	Orthorhom.
Space group	<i>Pbca</i>	<i>Pbca</i>	<i>Pbca</i>
Data range (Å)	20-0.81	20-0.81	20-0.81
Completeness (%)	94.8 (79.8) <sup>a</sup>	96.3 (83.7) <sup>a</sup>	97.4 (85.9) <sup>a</sup>
Redundancy	5.8 (1.9) <sup>a</sup>	5.3 (1.8) <sup>a</sup>	5.6 (1.9) <sup>a</sup>
<i>R</i> <sub>int</sub> , <i>R</i> <sub>sigma</sub> (%)	7.1, 5.6	9.4, 7.9	2.6, 9.7
Asymm. unit	WO <sub>3</sub> C <sub>5</sub> H <sub>4</sub> N(1)	(1)Na <sub>0.125</sub> <sup>b</sup>	(1)Na <sub>0.125</sub> <sup>c</sup>
<i>R</i> <sub>1</sub> (obs), #data <i>I</i> >2σ( <i>I</i> )	0.037, 1070	0.054, 1015	0.053, 1018
<i>R</i> <sub>1</sub> (all), #data	0.038, 1120	0.057, 1125	0.061, 1192
<i>wR</i> <sub>2</sub> (all data)	0.091	0.128	0.131
Resid. density (e <sup>-</sup> /Å <sup>3</sup> )	+3.9, -2.4	+3.3, -3.2	+4.5, -2.2

<sup>a</sup> Highest resolution bin (8.84-0.81 Å).  
<sup>b</sup> Refined *U* = 0.18 Å. <sup>c</sup> Refined *U* = 0.13 Å.

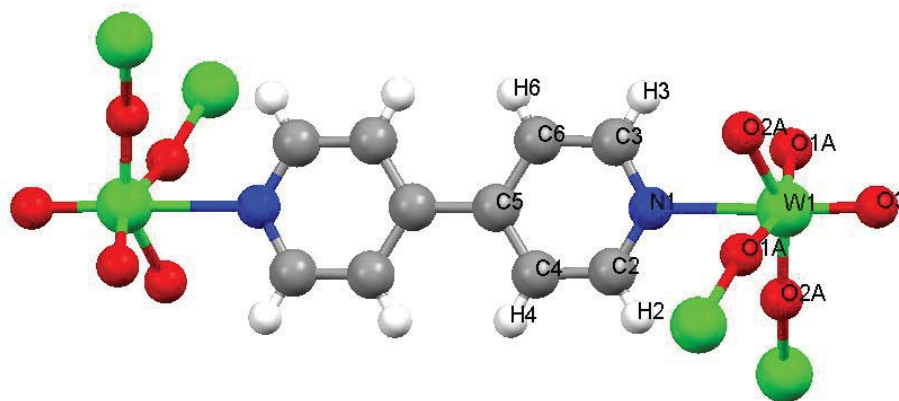


**Figure 3.7** Structural repeat unit for  $\text{Na}_x\text{WO}_3\text{-bpy}$  showing two  $\text{WO}_5\text{N}$  octahedra linked via the nitrogens on the bpy. Tungsten atoms are shown in green, oxygens in red, nitrogens in blue, carbons in grey and hydrogens in white. (*c*-axis is horizontal). Graphics using MERCURY<sup>150</sup>.

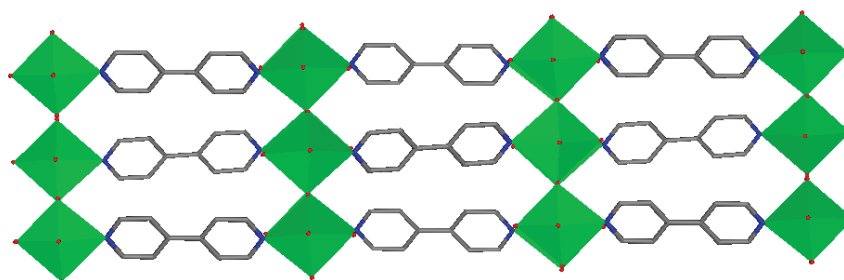


**Figure 3.8** The crystal structure of  $\text{WO}_3\text{-bpy}$  consists of layers of corner-shared octahedral tungsten oxide bridged by bpy ligands. The colour scheme is similar to Fig. 3.7. (*c*-axis is horizontal). Graphics using DSViewPro.<sup>151</sup>

In both the 2 % and 4%  $\text{Na}^+$ -implanted samples, electron density, absent in the unimplanted structure, lying on the  $\text{W}=\text{O}$  line approximately 3.0 Å from the axial oxygen atom and disordered about a centre of inversion, was evident. This was assigned to the implanted  $\text{Na}^+$  ion. The resulting structural unit is shown in Fig. 3.9.

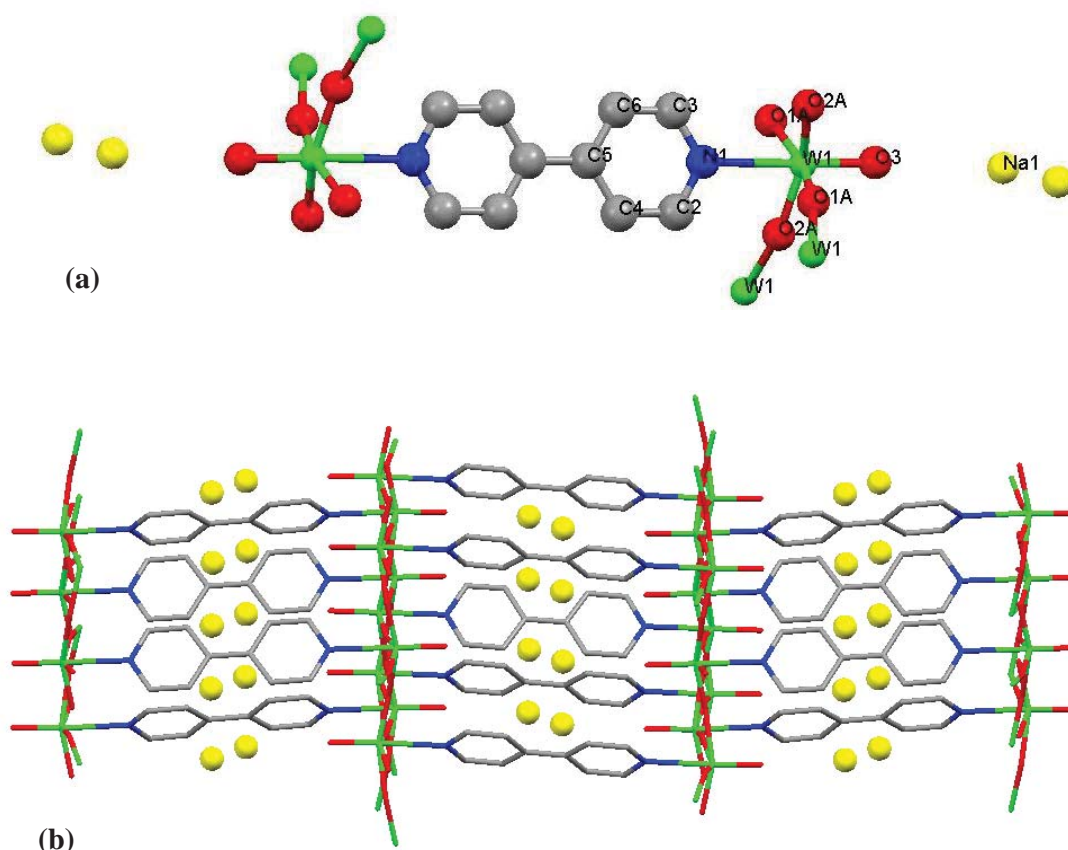


**Figure 3.9** (a) Structural repeat unit for  $\text{Na}_x\text{WO}_3\text{-bpy}$  showing two  $\text{WO}_5\text{N}$  octahedra linked via the nitrogens (blue) on the bpy. The intercalated  $\text{Na}^+$  ions (yellow) are bimodally located in the cage bounded along the  $c$ -axis by the axial oxygens (red), as depicted in (b). A cage structure is formed by the alternating alignment of the bpy planes. The display style is changed in (b) for convenience. The colour scheme is the same for both. ( $c$ -axis is horizontal.) Graphics using MERCURY<sup>150</sup>.

The consequences of ion implantation are mainly apparent in small changes in the slippage of one  $\text{WO}_4$  layer relative to the next and in the displacement of the W atom from the plane of the pyridyl ring. The effect of this slippage is to leave the W atoms slightly displaced from the plane of the pyridyl ring. The disposition of the  $\text{Na}^+$  ions in the staggered cages formed by the bpy is shown in Fig. 3.9 (b).

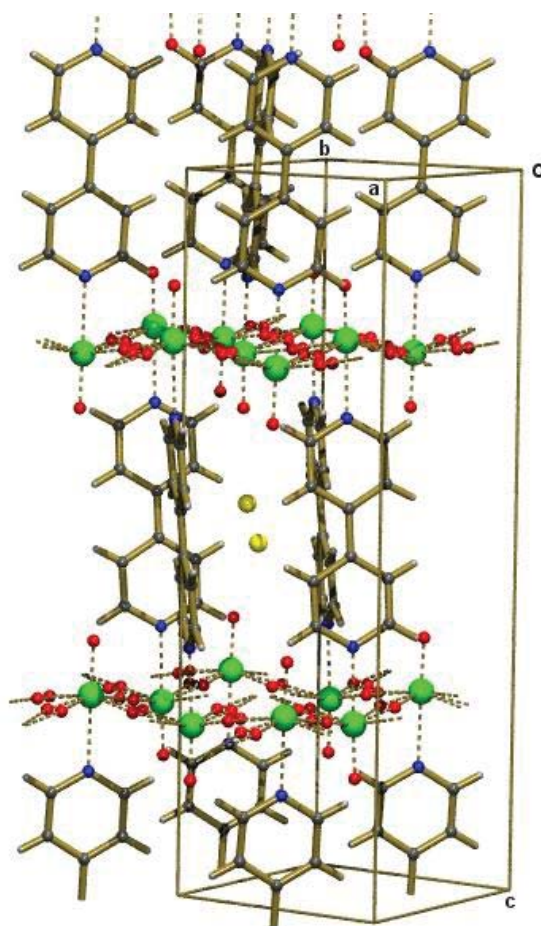


**Figure 3.10** The crystallographic structure of  $\text{Na}_x\text{WO}_3\text{-bpy}$  showing the inorganic  $\text{WO}_3\text{N}$  framework layers and one organic cage housing the  $\text{Na}^+$  intercalant. Atoms are coloured as in Fig. 3.7. (Graphics using PLATON<sup>152</sup> and POV-RAY<sup>153</sup>).

The synthetic method used to prepare  $\text{WO}_3\text{-bpy}$  was that of Yan *et al.*<sup>71</sup>, who reported the characterisation of their material in space group *Cmca*. However, in the present case, the unit cell was same as that of Yan *et al.*<sup>71</sup>, but instead systematic absences uniquely consistent with space group *Pbca* were observed. It was found that the bpy rings, which lie parallel to (110), are in fact disordered by the crystallographic mirror plane perpendicular to the [100] thus forming cages (Fig. 3.10) rather than [100] channels as reported by Yan *et al.*<sup>71</sup> Interestingly, the  $\text{WO}_3\text{-bpy}$  of Yan *et al.*<sup>71</sup> shows crystallographic equivalence in W–O–W bond lengths in the [010] direction and a marked asymmetry in the [100] direction, a pattern very similar to that which we observed for the unimplanted crystal. Curiously, whereas equatorial oxygen atoms are disordered and bpy rings are ordered in space group *Pbca*, the converse is true in space group *Cmca*.

### 3.4 Magnetic Measurements

The magnetic behaviour of any material can be described by two principal magnetic measurements: the temperature-dependent and field-dependent magnetization i.e.  $M(T)$  and  $M(H)$  respectively, where  $M$  is magnetization,  $T$  is temperature and  $H$  is applied magnetic field strength. Magnetic susceptibility ( $\chi$ ) can be defined as the ratio  $M/H$  and is used to indicate the degree of magnetization attained in a material in response to the applied magnetic field. Usually two types of magnetic susceptibility measurements are performed: zero field cooled (ZFC) measurements where a sample is first cooled to a characteristic low temperature before applying a magnetic field. Temperature is then raised slowly and the effects of an applied magnetic field are measured. In field cooled (FC) measurements, a magnetic field is applied at a relatively high temperature and then the effects of an applied magnetic field are measured as temperature is slowly lowered. Magnetic susceptibility can be used to provide valuable information about the occurrence of different types of magnetic behaviour in different materials. For example, in paramagnetic materials, which have a positive  $\chi$ , the magnetic field is strengthened by the induced magnetization and in diamagnetic materials, which have negative  $\chi$ , the induced magnetization weakens the applied magnetic field. Both, diamagnetic and paramagnetic materials cannot retain magnetization in the absence of applied magnetic field while ferromagnetic materials that have unpaired electrons and, hence a positive magnetic susceptibility, can retain a persistent magnetization even when the applied magnetic field is removed. Transition-metal tungstate hybrids exhibit a wide range of magnetic behaviour and incorporation of unpaired spins into these systems should give rise to magnetically correlated states. However, it should be noted that the magnetic properties of tungsten oxide based hybrids arise solely from any incorporated metal-ions, not tungsten which has zero spin in its highest oxidation state ( $W^{6+}$ ).

Magnetic measurements on thick polymer-bound  $WO_3$ -bpy films were performed using a Superconducting Quantum Interference Device (SQUID) magnetometer as described in section 2.3.4. Magnetic measurements revealed a sharp diamagnetic transition around 40 K (Fig. 3.11). However, this result was not reproducible as further measurements did not feature any transition. It is likely that this may have been a spurious measurement affected by some stray superconducting material from other laboratory studies. According to some previous studies  $Na^+$  intercalation in  $WO_3$  gives rise to non-localized superconducting states.<sup>21</sup> However, no evidence of

superconductivity was obtained from magnetic susceptibility measurements of Na<sup>+</sup>-implanted polymer-bound WO<sub>3</sub>-bpy films (Fig. 3.12). This could be attributed to nonhomogenous nature of films and the presence of polymer along with original WO<sub>3</sub>-bpy materials.

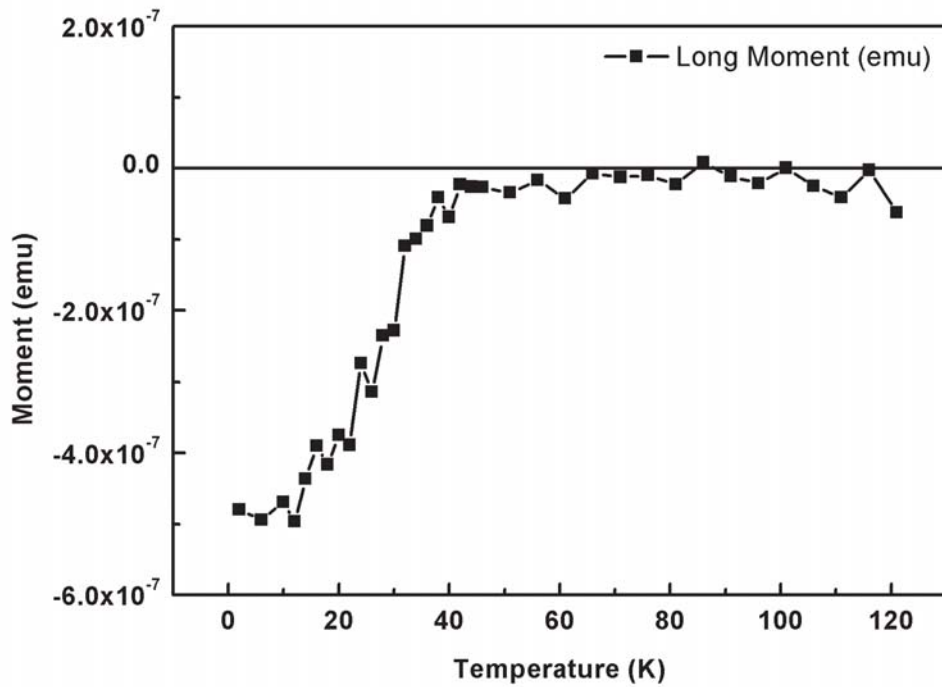


**Figure 3.11** ZFC magnetic measurements of WO<sub>3</sub>-bpy films measured at  $2 \times 10^{-4}$  Tesla.

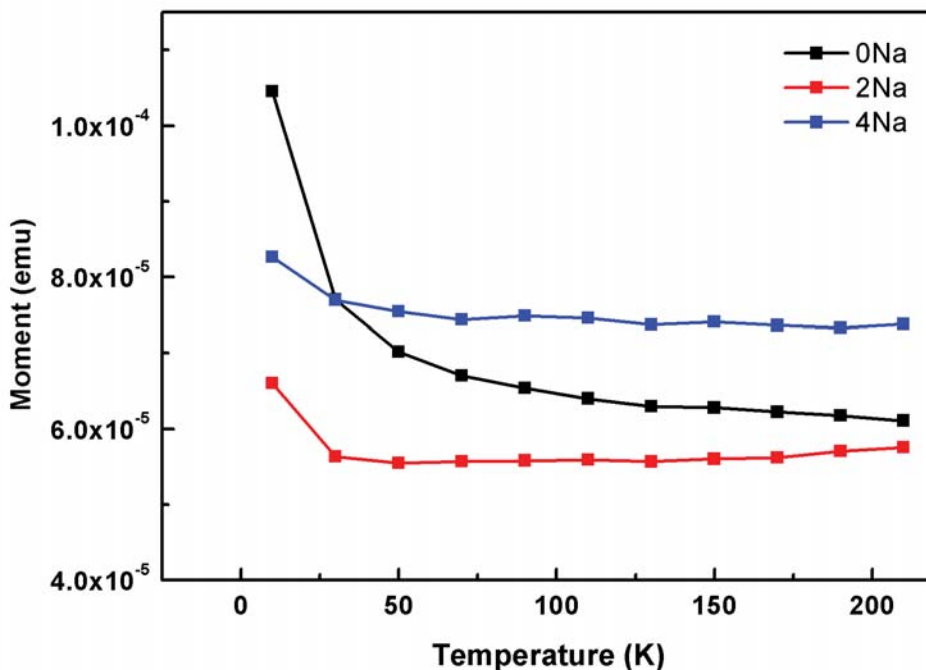


**Figure 3.12** Temperature-dependence of ZFC magnetic moment for unimplanted and  $\text{Na}^+$ -implanted polymer-bound  $\text{WO}_3$ -bpy films.

### 3.5 Raman Measurements

Raman spectroscopy was used to characterize the hybrid organic-inorganic material i.e.  $\text{WO}_3$ -bpy prepared from hydrothermal reactions of  $\text{Na}_2\text{WO}_4 \cdot 2\text{H}_2\text{O}$  and bpy. The aim was to exploit Raman scattering to study the nature of interactions between the organic and inorganic components, and the effect of dopant ions on these interactions. Normal modes related to bpy, which arise due to C–C and C–N bond stretching and in-plane bond-angle deformations, were expected to appear in the Raman spectra of the hybrid material.<sup>154</sup> Phonon modes, arising from stretching vibrations between W and O atoms in  $\text{Na}_2\text{WO}_4 \cdot 2\text{H}_2\text{O}$  were also expected to appear in the Raman spectra.<sup>155</sup>

In order to fully understand the behaviour of the Raman vibrational modes in hybrid  $\text{WO}_3$ -bpy material, Raman measurements were also performed on pure  $\text{Na}_2\text{WO}_4 \cdot 2\text{H}_2\text{O}$  and bpy. From Fig. 3.13, three peaks are identified at  $337 \text{ cm}^{-1}$ ,  $837 \text{ cm}^{-1}$  and  $930 \text{ cm}^{-1}$ , for sodium tungstate dihydrate. These peaks are in accordance with those observed in already published work relating to sodium tungstate dihydrate.<sup>156</sup> Most of the strong bands are completely symmetrical vibrational modes which are often observed in resonantly enhanced Raman spectra.<sup>155</sup>

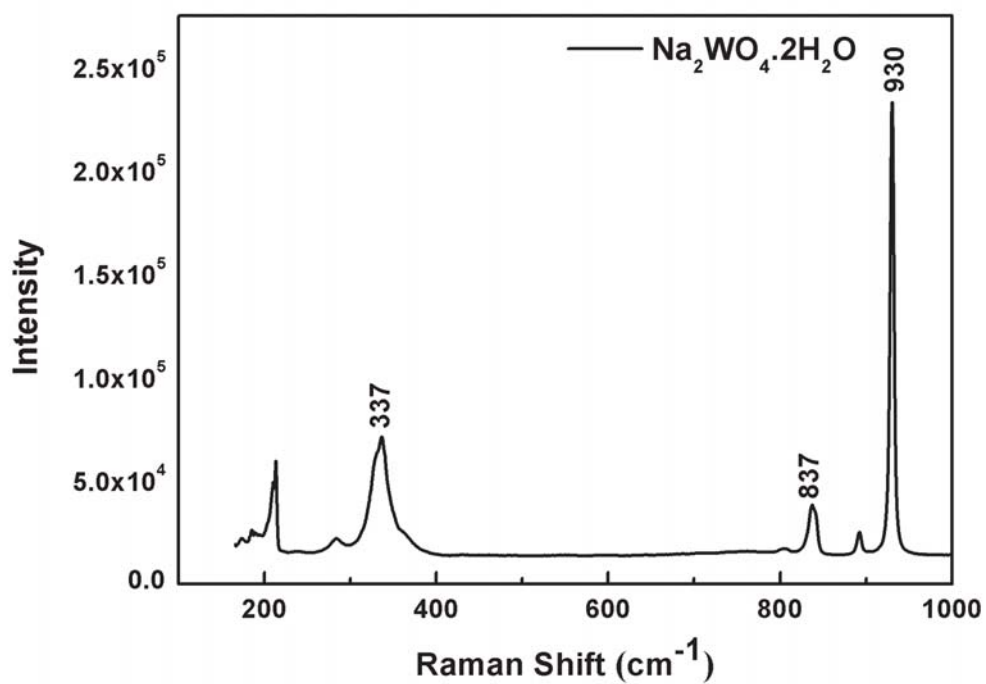


**Figure 3.13** Raman spectra of pure  $\text{Na}_2\text{WO}_4 \cdot 2\text{H}_2\text{O}$ . Intensity is measured in arbitrary units.

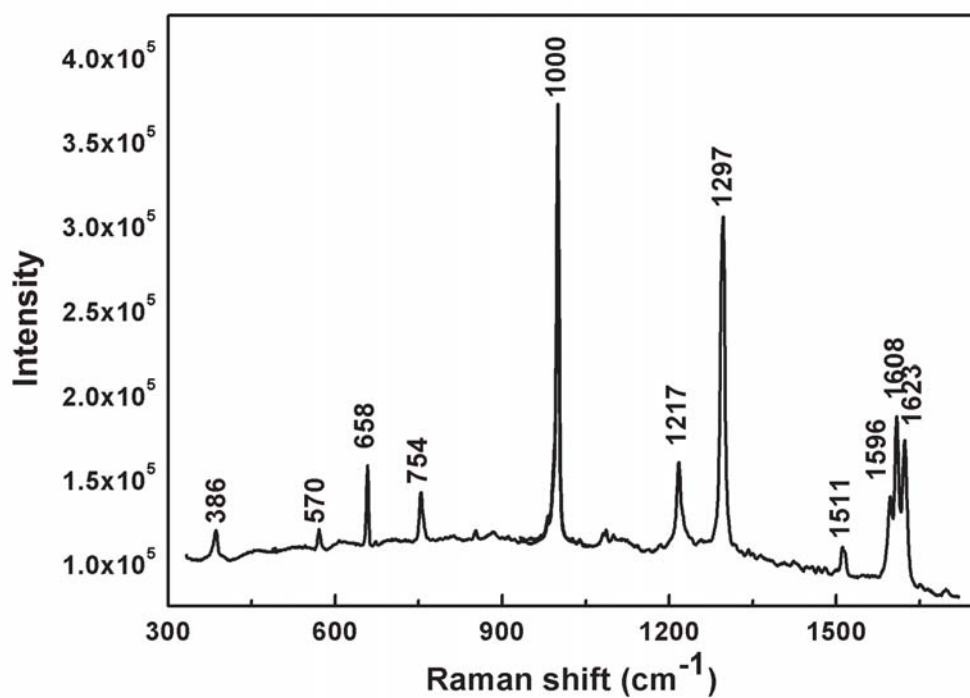
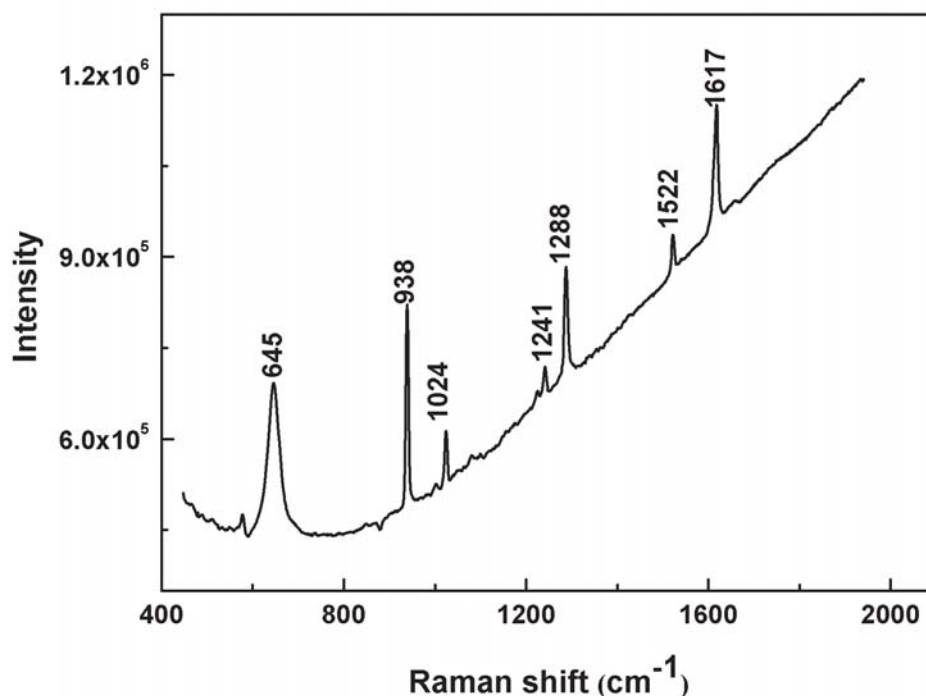


**Figure 3.14** Raman spectra of pure bpy. Data was collected over two spectral windows (330–1050 cm<sup>-1</sup> to 1050–1800 cm<sup>-1</sup>). Intensity is measured in arbitrary units.

Fig. 3.14 displays the Raman spectra of pure bpy, where the observed peaks at 386  $\text{cm}^{-1}$ , 570  $\text{cm}^{-1}$ , 658  $\text{cm}^{-1}$ , 754  $\text{cm}^{-1}$ , 1000  $\text{cm}^{-1}$ , 1217  $\text{cm}^{-1}$ , 1297  $\text{cm}^{-1}$ , 1511  $\text{cm}^{-1}$ , 1596  $\text{cm}^{-1}$ , 1608  $\text{cm}^{-1}$  and 1623  $\text{cm}^{-1}$  are similar to the already reported ones.<sup>154,157,158</sup>

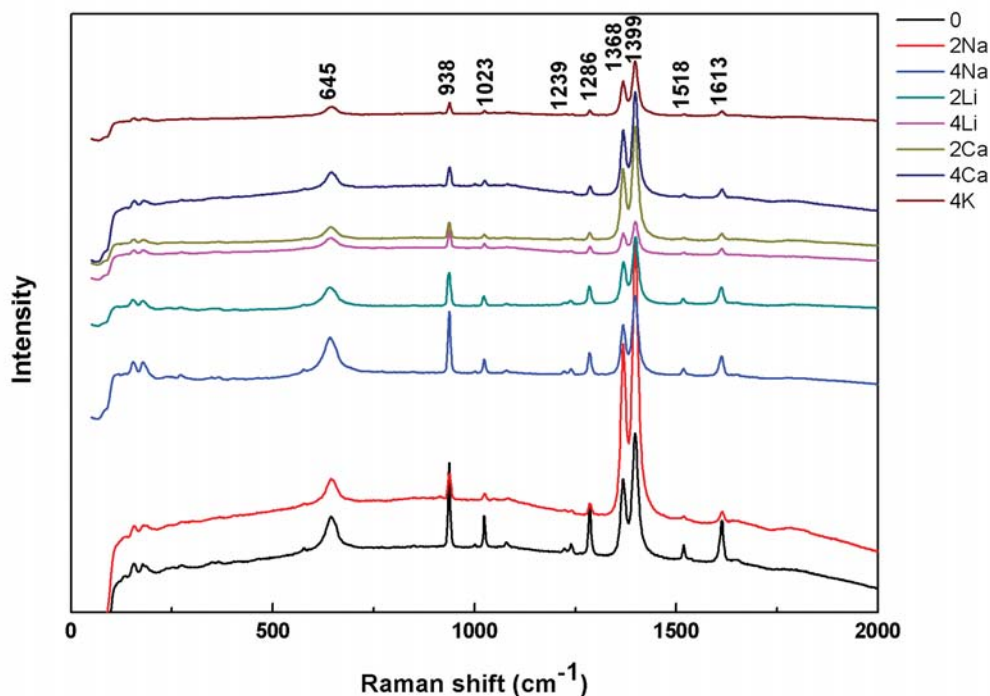
For the Raman studies of the  $\text{WO}_3$  hybrids, it is established that there are three Raman-active modes  $\nu_1(\text{A}_{1g}) + \nu_2(\text{E}_g) + \nu_5(\text{T}_{2g})$  for octahedrally co-ordinated  $\text{WO}_6$  molecules and any kind of distortion imposed on the structure lowers the symmetry and results in a greater number of Raman-active vibrational modes.<sup>159</sup> Therefore, ion implantation, which breaks local symmetry and potentially induces structural disorder, should increase the number of Raman modes relative to the unimplanted material.<sup>129</sup>

Fig. 3.15 shows that the molecular modes due to bpy, and stretching and bending vibrations of W–O bonds in tungsten oxide octahedra account for the main features of the Raman spectra of bulk  $\text{WO}_3$ -bpy hybrid material.<sup>154,156</sup> Since it is established that in  $\text{WO}_6$  octahedral systems most of the stretching and bending vibrations occur between 600-950  $\text{cm}^{-1}$ , the broad peak at 645  $\text{cm}^{-1}$  in the spectrum of  $\text{WO}_3$ -bpy is easily assigned to a stretching O–W–O vibration, whereas the peak at 938  $\text{cm}^{-1}$ , observed for all tungsten oxide based samples involved in this study, is identified as a symmetrical stretch of axial W=O bond.<sup>74,155</sup> The breadth of the 645  $\text{cm}^{-1}$  peak (in comparison with the 938  $\text{cm}^{-1}$  peak) is notable and possibly reflects the fact that equatorial oxygens are transversely disordered away from the W-W midpoint, at least at the temperatures of our measurements. Turning to the higher frequency modes of the organic spacer, Raman bands due to pyridyl rings in bpy appear at 1024  $\text{cm}^{-1}$ , 1288  $\text{cm}^{-1}$ , 1522  $\text{cm}^{-1}$  and 1617  $\text{cm}^{-1}$  in the  $\text{WO}_3$ -bpy spectra and are assigned to  $\nu_{\text{ring}} + \delta(\text{CH})$ ,  $\delta(\text{CH})$ ,  $\nu_{\text{ring}}$  and  $\nu_{\text{ring}}$  respectively, where  $\nu$  denotes stretching, and  $\delta$  denotes bending.<sup>158</sup> In keeping with the fact that certain vibrational modes of free bpy molecule show an upward shift in the spectrum of coordinated bpy, particularly due to coupling with metal-ligand bond vibrations, considerable shifts to higher frequencies were observed for Raman peaks of bpy in our  $\text{WO}_3$ -bpy materials as compared with those of free bpy molecule.<sup>158</sup>



**Figure 3.15** Raman spectra of powdered WO<sub>3</sub>-bpy. Intensity is measured in arbitrary units.

Raman measurements were also performed on doped and undoped polymer bound films of WO<sub>3</sub>-bpy coated on an alumina substrate. Certain phonon modes were expected to appear as a result of broken symmetry caused by doping the ions (off-centre in the cage, Fig. 3.10) into the material. The bottom spectrum in Fig. 3.16 corresponds to Raman spectra of pristine WO<sub>3</sub>-bpy polymer bound films where all the modes appear at similar positions to those observed for bulk WO<sub>3</sub>-bpy material. Two additional peaks, at 1368 cm<sup>-1</sup> and 1399 cm<sup>-1</sup>, appear in the Raman spectra of WO<sub>3</sub>-bpy polymer bound films. These peaks, being absent in the Raman spectra of bulk materials (Fig. 3.15), are attributed to the presence of polypropylene carbonate that was used to prepare thick films. Based on the structural changes induced by ion-implantation, we expected changes in the Raman spectra of ion-implanted polymer bound films. However, relative to undoped samples, no new Raman peaks (or even major shifts) were observed in spectra of doped samples. All the spectra, irrespective of doping, dopant ion and doping concentration, look similar to each other apart from a few irregular differences in some of the peak intensities. This could be attributed to the relatively shallow implantation in the samples relative to the film thickness, and also to the presence of an organic-binder in thick films. Thus in order to avoid these discrepancies, we sought to fabricate polymer-free thick films. This is discussed in chapter 4 in detail.



**Figure 3.16** Raman spectra of doped and undoped polymer bound films. Intensity is measured in arbitrary units.

### 3.6 Summary

Single-crystals and thick polymer bound films of  $\text{WO}_3\text{-bpy}$  have been prepared and characterized by a variety of experimental techniques. Powder XRD measurements reveal a layered structure for this compound which was later confirmed by single-crystal XRD measurements. The crystal structure of  $\text{WO}_3\text{-bpy}$  was found to be consisting of one-dimensional layers of corner-shared tungsten oxide octahedra interlinked by organic ligands to form a three dimensional covalently-bonded network. A careful investigation of the structural data obtained from single-crystal XRD revealed that bpy ligands define cages within the layered structure, potentially able to accommodate intercalated species. In order to precisely understand the effect of intercalated species, selected single-crystals of  $\text{WO}_3\text{-bpy}$  were characterized by XRD, doped with  $\text{Na}^+$ -ions using low energy ion-implanter and then the same crystal was re-characterized by XRD. The crystal structure of ion-implanted hybrids demonstrates the presence of  $\text{Na}^+$  related electron density in the cages which were found

empty for the un-implanted hybrids. This confirmed the bulk intercalation of charge carriers to the host material and prompted further studies. Thick polymer bound films of  $\text{WO}_3$ -bpy were prepared for physical characterization before and after implantation. Despite giving some useful information, magnetic measurements, powder XRD and Raman measurements failed to provide conclusive evidence of intercalation. This is attributed to the shallow implantation and the presence of an organic binder that was used to bind  $\text{WO}_3$ -bpy to the substrate. In short, the above results were highly motivating to carry on further studies on these systems by implanting metal ions other than  $\text{Na}^+$  and developing novel methods to fabricate polymer-free surface bound thick films of  $\text{WO}_3$ -bpy. These questions are addressed in the next chapter.

## Chapter 4

### **Influence of doping on hybrid organic-inorganic $\text{WO}_3(4, 4'$ -bipyridyl) $_{0.5}$ materials**

This chapter contains the follow-up work from the previous chapter. At first, the scope of implanting the  $\text{WO}_3$ -bpy single crystals was extended beyond the  $\text{Na}^+$  ions by implanting  $\text{Ca}^{2+}$  and  $\text{K}^+$  ions into the cages within  $\text{WO}_3$ -bpy. Secondly, in-order to understand the effect of implanted species on the bulk properties of  $\text{WO}_3$ -bpy, thick surface-bound films of  $\text{WO}_3$ -bpy were prepared and characterized before and after ion-implantation.

#### **4.1 Introduction**

There is great scientific interest in developing, understanding and manipulating the tunable structural, optical and electrical behaviours of tungsten oxide ( $\text{WO}_3$ ) films after it was first discovered that  $\text{WO}_3$  films display excellent electrochromic properties.<sup>160,161</sup> Depending on the requisite applications, different synthesis routes can be adopted for fabrication of  $\text{WO}_3$  films. Representative examples include evaporation, sputtering, chemical vapour deposition, atomic-layer deposition, spray-pyrolysis and sol-gel deposition.<sup>162-166</sup> Evaporation is the most convenient method to fabricate  $\text{WO}_3$  films where electron beam deposition is used to fabricate films that contain either of  $\text{WO}_2$ ,  $\text{WO}_3$ ,  $\text{W}_2\text{O}_6$ , and  $\text{W}_3\text{O}_9$  species.<sup>162</sup> Tungsten oxide films prepared by evaporation are largely disordered and have porosity that can be varied by annealing at different temperatures.<sup>163</sup> Nanocrystalline tungsten oxide films can be prepared by the evaporation of tungsten metal in the presence of oxygen.<sup>164</sup>

Sputtering is a well-established technique for the large scale-manufacturing of  $\text{WO}_3$  films.<sup>165</sup> By using DC magnetron sputtering, films can be deposited at temperatures between  $70\text{ }^\circ\text{C}$ – $100\text{ }^\circ\text{C}$ . The porosity of these films depends on the gas pressure in sputtering plasma. These films can become crystalline at  $300\text{ }^\circ\text{C}$ , however, addition of a small quantity of Ti can increase the stability of the films.<sup>166,167</sup> Chemical vapour deposition (CVD) is a low-temperature processing technique that produces amorphous and smooth  $\text{WO}_3$  films. CVD uses decomposition of  $\text{W}(\text{CO})_6$  at low temperatures to make highly porous  $\text{WO}_3$  films. With CVD high quality films can be produced at a very fast rate of  $10\text{ nm/sec}$ .<sup>165</sup> Spray pyrolysis

is a similar technique to CVD but it is possible to produce direct crystalline  $\text{WO}_3$  films at higher substrate temperatures.<sup>168</sup> One major drawback of spray pyrolysis is the evaporation of spray droplets before striking the target substrate. Sol-gel techniques provide a large number of synthetic routes that can be adopted for the fabrication of  $\text{WO}_3$  films.<sup>161,165</sup> Main sol-gel methods for fabricating  $\text{WO}_3$  films include spin-coating, dipping and layer-by-layer deposition. In order to optimize the properties of amorphous  $\text{WO}_3$  films and to overcome some of the drawbacks such as low response time and fatigue, new methods for the fabrication of  $\text{WO}_3$  based organic-inorganic thin films has been reported in recent times. For example, layer-by-layer deposition has been used to fabricate self-assembled superlattice thin-films of  $\text{WO}_3/4,4'$ -BAMBp (4,4'-bis(aminomethyl)-biphenyl).<sup>169</sup> The structure of these films consists of two dimensional networks of corner-shared  $\text{WO}_6$  octahedra where the organic ligands are interspersed between tungsten oxide layers. These films exhibit excellent photochromic and magnetic properties and open up investigations into the possibilities of making different hybrid organic-inorganic thick films based on  $\text{WO}_3$  systems.

This chapter describes a detailed structural, chemical and physical characterization of thick polycrystalline films of  $\text{WO}_3$ -bpy that were deposited on indium tin oxide (herein “ITO”) using a modified layer-by-layer technique. In order to understand the structural, physical and chemical features, these films were characterized by a variety of experimental techniques. In order to develop structural correlations between thick films and crystalline  $\text{WO}_3$ -bpy, the structures of  $\text{Ca}^{2+}$  and  $\text{K}^+$  implanted  $\text{WO}_3$ -bpy have also been determined.

## 4.2 Experimental Details

### 4.2.1 Synthesis

Single crystals of  $\text{WO}_3$ -bpy were synthesized by hydrothermal reactions as described previously (refer to section 3.2 for details).<sup>84,90</sup> Layer-by-layer deposition was attempted to prepare thin films of the bipyridyl tungstate. The main purpose of employing this method was to avoid organic binder solution in making films so that the electronic properties of these hybrid materials could be determined precisely. A possible model for multilayer thin films of  $\text{WO}_3$ -bpy structure is shown in Fig. 4.1. Synthesis of these films was attempted as follows:

First of all, tungstic acid colloid was prepared following the literature<sup>169</sup>. Then, fused silica substrates were surface modified with APS (3-aminopropyltriethoxysilane)<sup>170</sup> and

finally bpy solution in water acidified with HCl ( $\text{pH} \approx 2$ ) was prepared. For layer-by-layer deposition the following steps were performed <sup>169</sup>: (1) An APS-modified substrate was kept for 30 mins in 0.1 M HCl solution for protonation. Thus its surface charge becomes positive. (2) After drying in a vacuum, the substrate was immersed in tungstic acid colloid for 60 mins, thus covering the substrate with one layer of inorganic compound and reversing its charge to negative. (3) After rinsing with milli-Q water and vacuum drying, the substrate was immersed in bpy solution for thirty minutes. Steps (2) and (3) were repeated several times for thirty minutes each in cyclic fashion. After dipping in tungstic acid solution, a white irregular pattern appeared on the surface of the substrate hinting the formation of some sort of layer. This pattern faded on dipping the substrate in bpy solution. This kept on happening during each cycle thereby prohibiting the formation of layer-by-layer film.

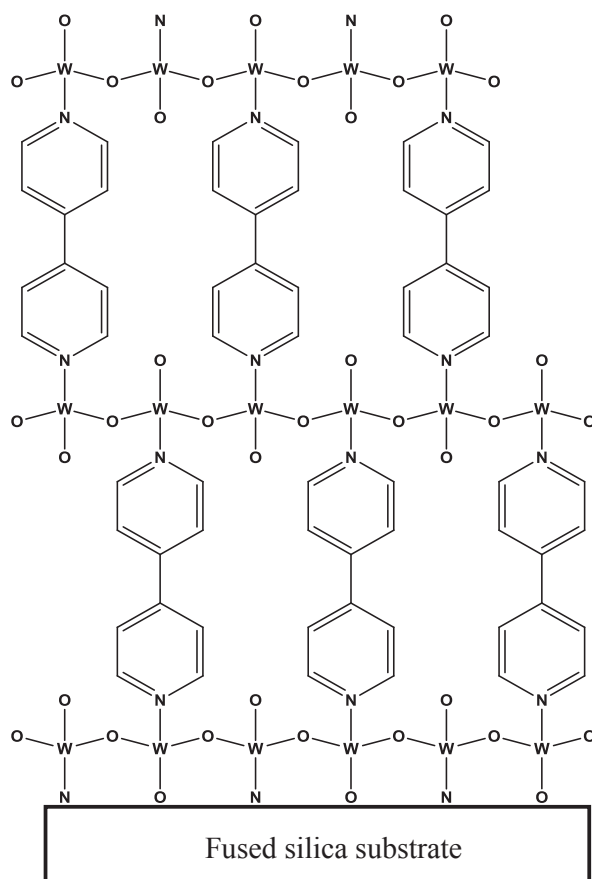


**Figure 4.1** A possible structural model for multilayer thin films of  $\text{WO}_3$ -bpy.

In another attempt, electrochromic coatings were prepared on ITO-coated glass substrates for subsequent layer-by-layer deposition (Fig. 4.2). Tungsten oxide was deposited

onto ITO glass using a literature method.<sup>171</sup> Specifically, tungsten metal powder was dissolved in a solution of glacial acetic acid and 30 % H<sub>2</sub>O<sub>2</sub> (50:50) at 0±1 °C. After standing for 24 hours at a temperature between 0-15 °C, the solution was then refluxed at 55 °C for 18 hours before being filtered to obtain a transparent pale yellow coloured solution. The excess solvent was evaporated under reduced pressure at 65 °C to obtain tungsten peroxy acid as a yellow coloured powder. This was reacted with ethanol at 60 °C for one hour and used immediately for coating WO<sub>3</sub> on ITO-coated glass slides.

ITO glass substrates were cleaned by rinsing with deionized water, sonicating in acetone, again rinsing with deionized water, and drying under vacuum. Alternating layers of WO<sub>3</sub> and bpy were deposited in a two-step manner. (1) Each substrate was dipped in the as-prepared solution of WO<sub>3</sub> for 10 seconds and withdrawn gently. These substrates were then dried in vacuum before heating in a pre-heated oven at 250 °C for 10 minutes. Thus each substrate was covered with a layer of inorganic material. (2) After cooling down to room temperature these substrates were kept in 0.5 molar aqueous solution of bpy inside a Teflon-lined stainless steel autoclave at 160 °C for 72 hours. The sample holder was then slowly cooled overnight before the sample was recovered. As steps (1) and (2) were repeated in alternating fashion a pale yellow coloured coating became apparent on the surface of ITO. All the measurements were performed on samples which were obtained after repeating steps (1) and (2) four times.

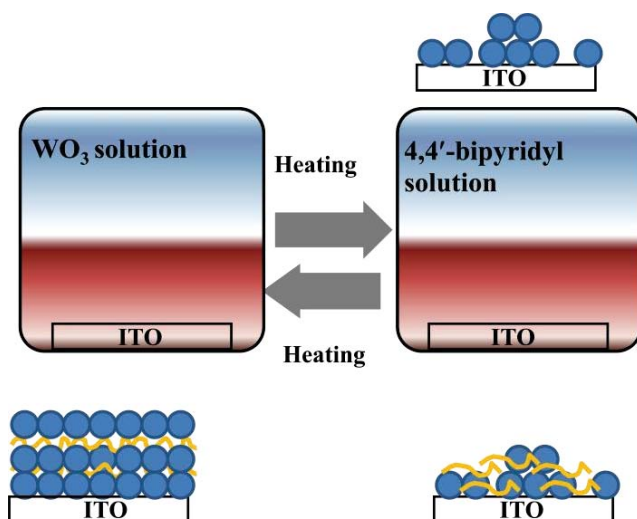


**Figure 4.2** A simplified sketch of modified layer-by-layer scheme for deposition of WO<sub>3</sub>-bpy on ITO.

### 4.2.2 Ion-Implantation

WO<sub>3</sub>-bpy single crystals of sizes  $\sim (10-50) \times (10-50) \times (0.1-0.3) \mu\text{m}^3$  were selected and, separately, 25 keV mass-selected Na<sup>+</sup>, Ca<sup>2+</sup> and K<sup>+</sup> ions were doped into both (opposing large) faces using a lab-built low-energy ion implanter (refer to section 2.2 and 3.2 for details on ion-implantation experiments). Most of the intercalated ions resided in the top 110 nm of each surface and hence penetrate the entire depth of small single crystals.<sup>90</sup> Thick films were also implanted and since the thickness of films is far greater than that of single crystals the implanted ions will remain localised in the uppermost surface layer only. For cross-comparison, all the samples were characterized before and after ion-implantation. Intense changes in colour, modified surface chemical composition, structural and spectroscopic properties, and improved conductivity were noted as main consequences of implanting the host material with metal ions, as described below.

### 4.2.3 Characterization

Raman measurements, and powder as well as single-crystal XRD measurements were performed with the instruments described in previous chapters (refer to sections 2.3 and 3.2). Single crystal XRD data was collected on two WO<sub>3</sub>-bpy single crystals of sizes approximately  $\sim (50) \times (30) \times (0.1) \mu\text{m}^3$ . After data collection on the un-implanted crystals, and while still mounted on their polyimide mounts, both large faces of the crystals were ion-implanted, one crystal with Ca<sup>2+</sup> and the other with K<sup>+</sup> ions and then recharacterised by single-crystal XRD. Structures were obtained for only 2 % Ca<sup>2+</sup> and 2 % K<sup>+</sup> compositions since the diffraction data obtained from 4 % implanted samples were not good enough due to extensive damage by the greater ion flux<sup>90</sup>. Therefore, a detailed structural analysis of only the 2 % Ca<sup>2+</sup>- and K<sup>+</sup>-implanted single crystals is presented.

XPS was used to study the chemical states and stoichiometry of WO<sub>3</sub>-bpy films before and after ion-implantation. Measurements were performed on a Kratos Axis UltraDLD surface analyzing chamber using a monochromated Al K $\alpha$  (1486.69 eV) radiation source. A power of 150 W was used in conjunction with detector pass energy of 160 eV for the survey scans and 20 eV for the core-level narrow-scans. Sample charging was accounted for by shifting all the XPS peaks to fix the carbon 1s reference peak at 285 eV binding energy. SEM images were recorded with FEI Quanta 200 Environmental Scanning Electron Microscope.

Due to the high resistance of the  $\text{WO}_3$ -bpy films, the electrical resistance of the films was measured using a two-terminal configuration. Resistance measurements were carried out on  $\text{WO}_3$ -bpy films before and after ion implantation as a function of temperature. The metallic contacts were deposited onto the films by thermal-evaporation of silver metal with an electrode-gap of less than 0.5 mm. Silver epoxy was used to attach the wires to the silver electrodes. The non-implanted  $\text{WO}_3$ -bpy films have a typical resistance of more than 1 M $\Omega$  at room temperature.

### 4.3 Thick-film structure

Scanning Electron Microscopy (SEM) images of the  $\text{WO}_3$ -bpy films show the formation of an intergrown network of microcrystallite plates on the ITO surface (Fig. 4.3).

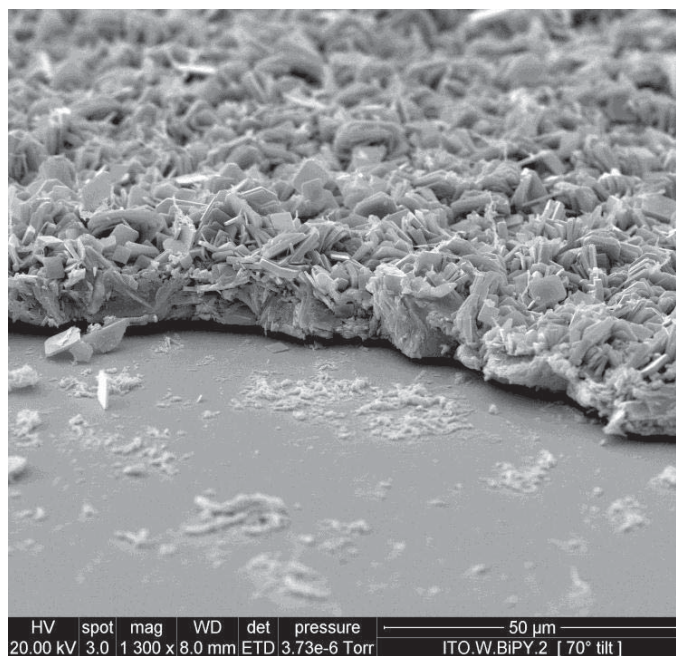


**Figure 4.3** An SEM image of  $\text{WO}_3$ -bpy coated ITO using SEM reveals the formation of intergrown microcrystals.

Powder XRD patterns of bulk  $\text{WO}_3$ -bpy material consist of sharp (00*l*) reflections, where  $l = 2, 4, 6, 8, 10, 12, 14$ , which are characteristic of the formation of a layered structured material (Fig. 4.4). When powder XRD measurements were performed on surface-bound  $\text{WO}_3$ -bpy coatings a diffraction pattern very similar to that of bulk crystalline material,

was obtained strongly indicating that the structure of surface-bound material is identical to that of bulk crystalline material. This was supported by Raman spectroscopic measurements (*vide infra*) where Raman peaks appear at same positions for WO<sub>3</sub>-bpy thick films and bulk material suggesting the formation of essentially identical structures in both cases.

Moreover, no discernable shifts in the diffraction peaks in the powder X-ray diffractograms were observed after ion-implantation of WO<sub>3</sub>-bpy films (Fig. 4.5). This might suggest that the implanted species reside close to the surface of the material and cause very little change to the lattice parameters. However, despite demonstrable intercalation, single-crystal XRD shows that the accompanying changes in cell parameters are in fact small (see section 4.4). Therefore the absence of significant changes in cell parameters cannot be taken as evidence of lack of intercalation. Powder patterns calculated from single-crystal XRD of implanted samples also indicate that diffraction peaks are expected to remain largely unchanged after implantation (Fig. 4.6).

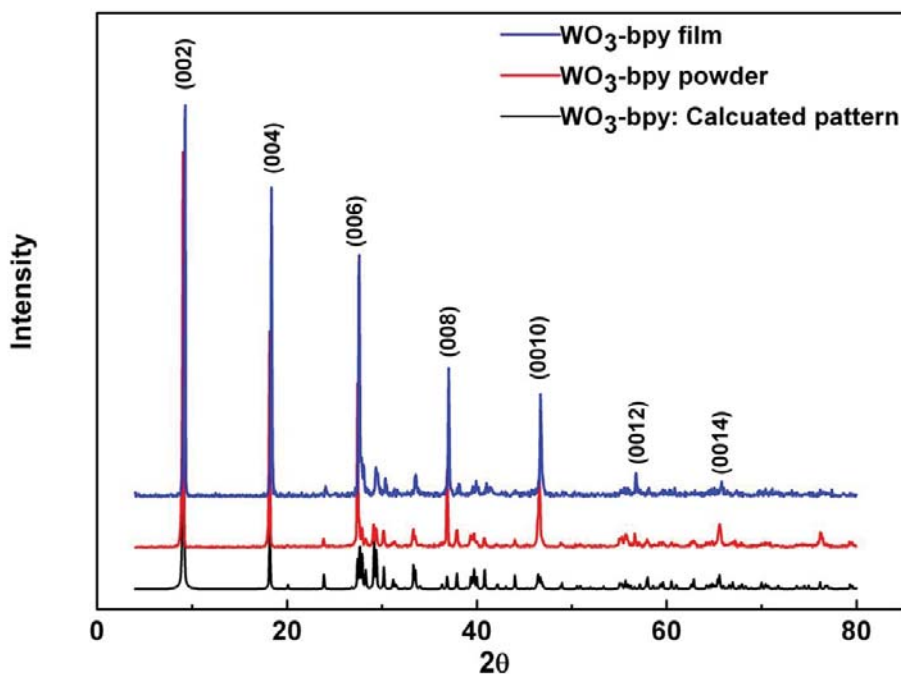


**Figure 4.4** Powder X-ray diffractograms of WO<sub>3</sub>-bpy. The diffraction angle is for Co K $\alpha$  radiation. Evidence for the same layered structure for all the forms of WO<sub>3</sub>-bpy: black = pattern calculated from the single-crystal structure, red = experimental pattern of bulk WO<sub>3</sub>-bpy, blue = experimental pattern of ITO-bound WO<sub>3</sub>-bpy. For comparison, wavelength was changed to Co K $\alpha$  in the pattern calculated from single crystal structure of WO<sub>3</sub>-bpy, which was determined with Cu K $\alpha$  radiation. Intensity is measured in arbitrary units and Bragg angle in degrees.

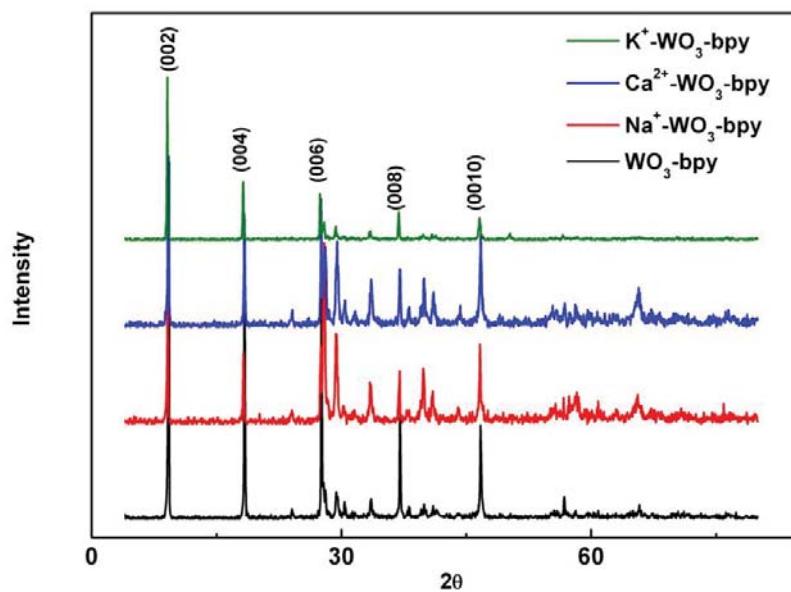


**Figure 4.5** A comparison of powder XRD patterns obtained from  $WO_3$ -bpy films before and after ion-implantation. Intensities were enlarged in both figures. The diffraction wavelength is of Co  $K\alpha$ . Intensity is measured in arbitrary units and Bragg angle in degrees.

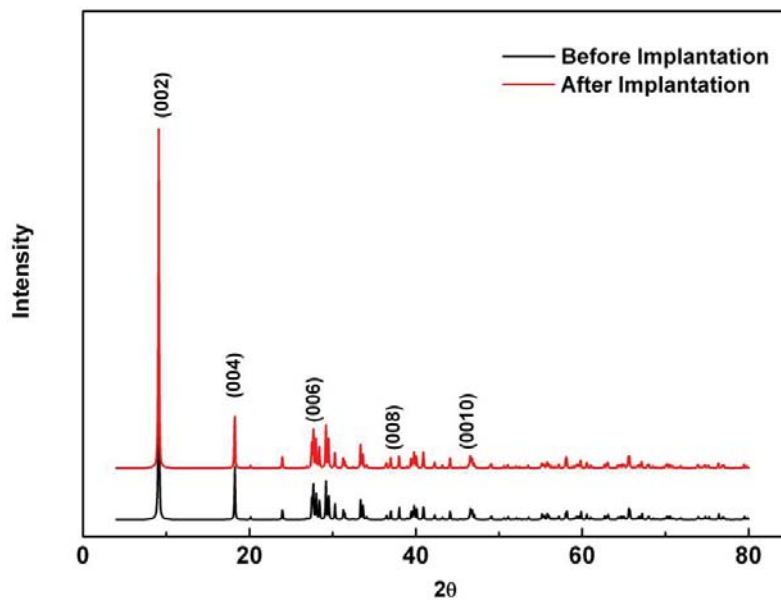


**Figure 4.6** A comparison of powder XRD patterns calculated from single crystal XRD measurements of  $WO_3$ -bpy materials before and after ion-implantation. The diffraction wavelength is of Cu  $K\alpha$ . Intensity is measured in arbitrary units and Bragg angle in degrees.

## 4.4 Single-crystal X-ray Diffraction Studies

The crystal structure of unimplanted and Na<sup>+</sup>-implanted WO<sub>3</sub>-bpy has been reported previously<sup>90</sup> (refer to chapter 3 for full structural details).

Turning to the Ca<sup>2+</sup> and K<sup>+</sup> implanted samples, electron density, absent in the unimplanted structure, lying near the axial line was evident. This was assigned to the implanted Ca<sup>2+</sup> and K<sup>+</sup> ions. The distance of this electron density from the axial oxygen is 2.7 Å for Ca<sup>2+</sup>-implanted samples; compared with the Na<sup>+</sup>-implanted sample, this density lies closer to the centre of inversion and is disordered over the two sites either side of the inversion centre. For K<sup>+</sup>-implanted samples, where K<sup>+</sup> is the largest of three ions, Na<sup>+</sup>, Ca<sup>2+</sup> and K<sup>+</sup>, the electron density moves deeper still into the cage and sits in the centre without any disorder in contrast to that observed for Na<sup>+</sup> and Ca<sup>2+</sup>-implanted samples. The resulting structural units are shown in Fig. 4.7. It was observed that both Ca<sup>2+</sup> and K<sup>+</sup> implantation led to an increase in the *b* and *c* axes resulting to a small expansion in the unit cell volume (approximately 0.1 % or more than 1 Å<sup>3</sup>) in both cases despite a minute decrease in the lengths of the *a* axis, 0.003% and 0.05% respectively for Ca<sup>2+</sup> and K<sup>+</sup> implantation. These small changes in cell parameters are at least partially due to the fact that implanted species are present in very small quantities: the occupancy of Ca is 0.05 and for K it is 0.03. These small increases in volume superficially suggest that the intercalated structures may be metastable only i.e. the structural energy is fractionally raised by the intercalation. However, it is more likely that the small increase in atomic volume is due to internal strain arising from structural damage. The crystallographic data are summarised in Table 4.1.

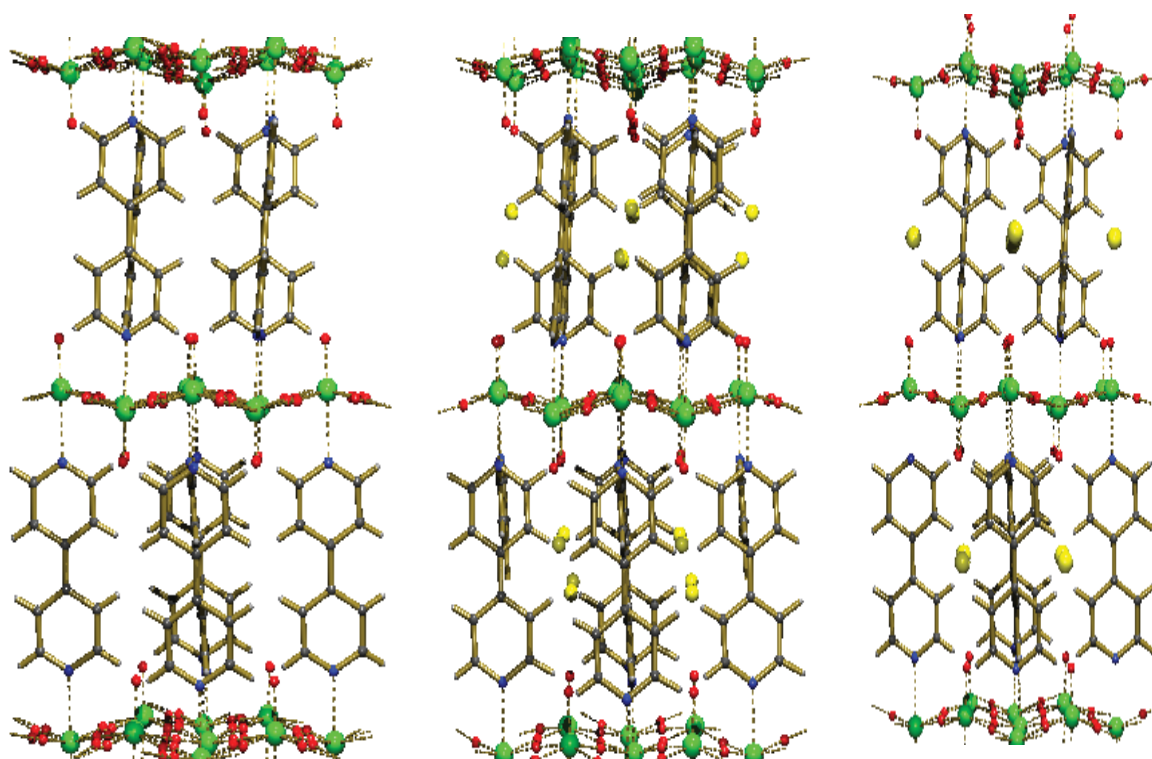


**Figure 4.7** Crystal structures of WO<sub>3</sub>-bpy before (left) and after implantation (centre, Ca<sup>2+</sup> and right, K<sup>+</sup>). Tungsten atoms are shown in green, oxygens in red, nitrogens in blue. Yellow colour represents the sites attributed to implantation of Ca<sup>2+</sup> (centre) and K<sup>+</sup> (right) ions. Like Na<sup>+</sup>, Ca<sup>2+</sup> resides disordered over two sites away from the inversion centre in the centre of the cage, while K<sup>+</sup> resides at the cage centre on a crystallographic centre of inversion. Graphics using PLATON<sup>152</sup> and POV-RAY<sup>153</sup>.

**Table 4.1** Selected single-crystal X-ray diffraction data collection and refinement details of implanted and non-implanted WO<sub>3</sub>-bpy .

Parameter	0 % Ca <sup>2+</sup>	2 % Ca <sup>2+</sup>	0 % K <sup>+</sup>	2%K <sup>+</sup>
Temperature (/K)	143	163	143	153
<i>a</i> (/Å)	7.4777(5)	7.4775(10)	7.4788(10)	7.4751(10)
<i>b</i> (/Å)	7.3858(6)	7.3925(10)	7.3876(10)	7.3943(10)
<i>c</i> (/Å)	22.5668(16)	22.5829(16)	22.5707(16)	22.5813(16)
$\alpha, \beta, \gamma$ ( $^\circ$ )	90, 90, 90	90, 90, 90	90, 90, 90	90, 90, 90
<i>V</i> (/Å <sup>3</sup> )	1246.34(14)	1248.32(9)	1247.04(9)	1248.14(9)
Crystal system	Orthorhom.	Orthorhom.	Orthorhom.	Orthorhom.
Space group	<i>Pbca</i>	<i>Pbca</i>	<i>Pbca</i>	<i>Pbca</i>
Data range (/Å)	20-0.81	20-0.81	20-0.81	20-0.81
Completeness (/%)	94.6	99.0	98.7	98.8
Redundancy	6.48	14.22	14.28	15.78
<i>R</i> <sub>int</sub> , <i>R</i> <sub>sigma</sub> (/%)	11.08, 7.38	11.63, 7.56	11.95, 6.84	11.07, 4.89
Asymm. unit	WO <sub>3</sub> C <sub>5</sub> H <sub>4</sub> N(1)	(1)Ca <sub>0.050</sub> <sup>a</sup>	WO <sub>3</sub> C <sub>5</sub> H <sub>4</sub> N(2)	(2)K <sub>0.03</sub> <sup>b</sup>
<i>R</i> 1(obs), #data <i>I</i> >2 $\sigma$ ( <i>I</i> )	0.0718, 1010	0.065, 693	0.0727, 749	0.042, 631
<i>R</i> 1(all), #data	0.0853, 1213	0.073, 756	0.0851, 897	0.046, 756
<i>wR</i> 2 (all data)	0.2303	0.132	0.2429	0.107
Resid. density (/e <sup>-</sup> /Å <sup>3</sup> )	+4.93, -4.55	+2.27, -2.65	+4.68, -4.73	+2.36, -2.14

<sup>a</sup> Refined *U* = 0.10 Å. <sup>b</sup> Refined *U* = 0.12 Å

## 4.5 Raman Spectroscopy

Raman measurements were performed to study the interactions between organic and inorganic components of the intercalated hybrid network and the effect of doping on these materials. There are three Raman-active modes  $\nu_1(A_{1g}) + \nu_2(E_g) + \nu_3(T_{2g})$  for octahedrally coordinated  $WO_6$  molecules and any kind of distortion imposed on the structure lowers the symmetry and results in a greater number of Raman-active vibrational modes.<sup>159</sup> Therefore, ion implantation, which breaks local symmetry and potentially induces structural disorder, should increase the number of Raman modes relative to the unimplanted material.<sup>129</sup>

The bottom spectrum in Fig. 4.8 corresponds to the Raman spectra of bulk  $WO_3$ -bpy hybrid material where all the assignments are made similar to those mentioned in Section 3.4.

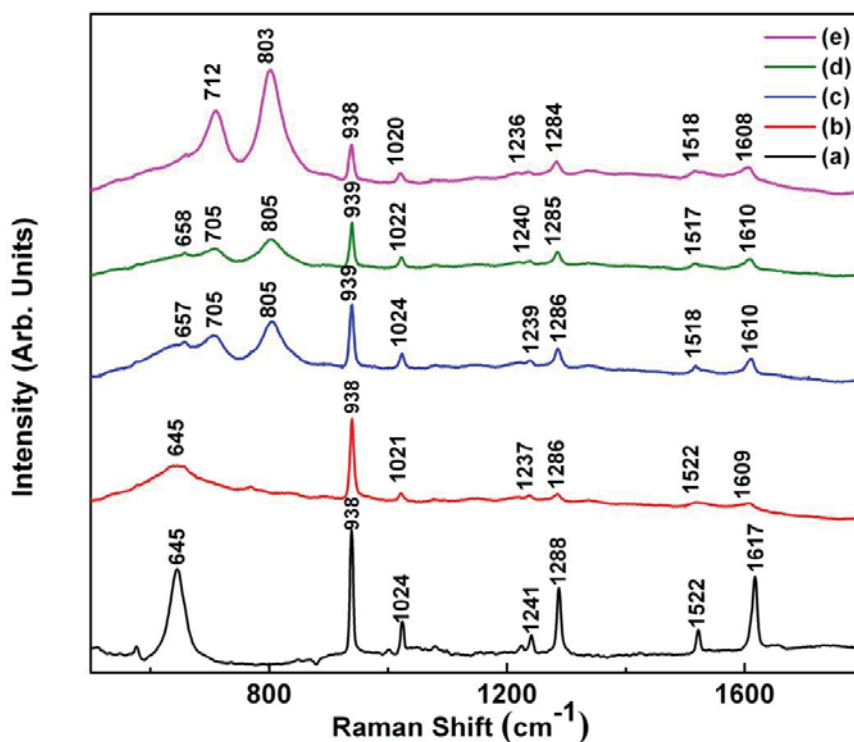


**Figure 4.8** Raman spectra of  $WO_3$ -bpy before and after ion-implantation. (a) Bulk crystalline  $WO_3$ -bpy material, (b)  $WO_3$ -bpy film before implantation, (c)  $Na^+$ -implanted  $WO_3$ -bpy film, (d)  $Ca^{2+}$ -implanted  $WO_3$ -bpy film (e)  $K^+$ -implanted  $WO_3$ -bpy film.

In Fig. 4.8, the Raman spectra (b-e) correspond to various WO<sub>3</sub>-bpy films before and after implantation. Raman peaks for pure WO<sub>3</sub>-bpy films appear at similar positions to those of the bulk crystalline material; the most notable difference in the film spectrum is a marked broadening of the band at 645 cm<sup>-1</sup>, whose broadened nature in unimplanted material had been attributed to observed disorder in positions of equatorial oxygen atoms.<sup>90</sup> Nonetheless, the Raman spectra confirm the formation of essentially identical structures in both cases. However, new peaks appear in the Raman spectra of films after ion-implantation (Fig. 4.8(c-e)). For Na<sup>+</sup>- and Ca<sup>2+</sup>-implanted samples, these new peaks appear at 705 and 805 cm<sup>-1</sup> while the broad peak due to the O–W–O stretching vibration is shifted from 645 cm<sup>-1</sup> in the unimplanted samples to 658 cm<sup>-1</sup> after implantation. For the K<sup>+</sup>-implanted samples, these peaks appear at 712 and 803 cm<sup>-1</sup> with greater intensity than for the Na<sup>+</sup>- and Ca<sup>2+</sup>-implanted samples, whereas the shoulder peak at 658 cm<sup>-1</sup> becomes very weak. The implanted samples all show significantly decreased intensity of the 939 cm<sup>-1</sup> mode, especially for the K<sup>+</sup>-implanted sample. This mode is interpreted as a marker for the unimplanted materials and the presence of this mode in the implanted spectra indicates that there are regions of the sample within the scattering volume that retain the unimplanted structure. The spectra show that the K<sup>+</sup>-implanted samples have the smallest proportion of the unimplanted material remaining. The new peaks at 705–712 and 805 cm<sup>-1</sup> remain unidentified, but though these peaks are broadened, they are not as broad as might be expected if they originated merely from structural disorder arising from the implantation process. Further, there is a slight distortion in the bpy rings as a result of the ion implantation, but nonetheless the overall intensity and position of the bpy-related modes remain essentially unaltered, suggesting that the overall hybrid structure, as reflected by the Raman studies, remains the same. These new modes appear to be well-defined vibrational modes modified by the presence of the intercalated cations. Indeed, two essentially identical modes are observed at 713 and 804 cm<sup>-1</sup> in monoclinic WO<sub>3</sub>, and there the modes are assigned, respectively, to the asymmetric and symmetric O–W–O stretches. We tentatively make the same assignment in the case of the doped hybrid.<sup>172</sup>

## 4.6 X-Ray Photoelectron Spectroscopy

In order to study the surface composition and local chemical states, thick films of WO<sub>3</sub>-bpy were analysed with XPS before and after ion-implantation. In the past, XPS has been used as an efficient tool to demonstrate the effect of doping on surface chemical states of metal-oxide films.<sup>84,173</sup>

Fig. 4.9 gives a comparison of XPS spectra recorded from implanted and non-implanted thick films of WO<sub>3</sub>-bpy. The core-level peaks of W 4*f*, O 1*s*, C 1*s* and N 1*s*, which constitute the chemical composition of WO<sub>3</sub>-bpy, are apparent in all samples, while new peaks appear for the implanted samples. These new peaks are assigned to core-level peaks for Na 1*s*, Ca 2*p* and K 2*p* on the basis of the respective elements used in the implantation. The XPS spectra of non-implanted WO<sub>3</sub>-bpy films reveal that tungsten is present in its highest oxidation state of +6, which is similar to the already reported measurements from WO<sub>3</sub> thin films.<sup>174-176</sup> For non-implanted samples, the XPS C 1*s* peak can be deconvoluted into two components (Fig. 4.10). The peak with lower binding energy value of 284.9 eV can be assigned to adventitious surface carbon while the one at a higher binding energy value of 285.7 eV is assigned to C=C of bpy as reported in the earlier investigation of similar compounds.<sup>84,177</sup> The XPS O 1*s* spectrum shows the presence of two oxygen species at the surface of non-implanted WO<sub>3</sub>-bpy films (Fig. 4.10). The O 1*s* peak at 530.24 eV corresponds to lattice oxygen while the one with a higher binding energy of 532.01 eV is assigned to adsorbed oxygen.<sup>56</sup> One can rule out the possibility of the latter peak being a surface hydroxyl in which case it would have appeared at 533.2 eV.<sup>178</sup> In the XPS survey scan of WO<sub>3</sub>-bpy, the appearance of the N 1*s* peak as a singlet at 394.5 eV suggests that bipyridyls are coordinated. Therefore, it can be inferred that nitrogen is not protonated as this would result in the appearance of another nitrogen related XPS peak at 401 eV.<sup>179,180</sup> This is also supported by Raman measurements (Fig. 4.9) where the absence of stretching N–H vibration confirms that bpy is not protonated. Single-crystal XRD rules out this possibility as well where none of the nitrogens were protonated. From these XPS measurements the C/W, N/W and O/W atomic ratios are calculated to be 6.26, 0.9, and 2.81 respectively. This gives an effective formula of WO<sub>2.81</sub>C<sub>6.26</sub>H<sub>5</sub>N<sub>0.9</sub> for the surface of this compound which is in good agreement with the chemical formula (WO<sub>3</sub>C<sub>5</sub>H<sub>4</sub>N) obtained from single-crystal XRD measurements.

It can be noted that ion-implantation doesn't have much effect on the C 1s, O 1s and N 1s peaks which is consistent with the results from Raman measurements and single-crystal XRD. However, the XPS spectrum of tungsten related peaks change remarkably upon ion-implantation. The lower spectrum in Fig. 4.11 shows the W 4f peak of the unimplanted sample, which, upon Shirley background subtraction, is assigned to the doublet W 4f<sub>7/2</sub> and W 4f<sub>5/2</sub>.<sup>176</sup> The binding energies of the peaks are at 35.5 and 37.6 eV, respectively, with a full-width at half-maximum (FWHM) of 1.1 eV. The energy position of this doublet corresponds approximately to W<sup>6+</sup>.<sup>175</sup> The remaining curves in Fig. 4.11 show the evolution of the W 4f peaks upon ion implantation, where a significant broadening is observed, in addition to the evolution of new peaks on the lower-binding-energy side of the W<sup>6+</sup> XPS peaks. Furthermore, the lower-binding-energy peaks are higher in intensity compared with the fully oxidised tungsten peak indicating a considerable amount of reduced tungsten species caused by the implantation process. Indeed, deconvolution of the implanted W 4f peaks show the presence of W<sup>5+</sup> (4f<sub>7/2</sub> = 35.7 eV, 4f<sub>5/2</sub> = 37.8 eV), W<sup>4+</sup> (4f<sub>7/2</sub> = 34.9 eV, 4f<sub>5/2</sub> = 37.0 eV), plus a tungsten sub-oxide, "WO<sub>x</sub>", species with binding energies of W 4f<sub>7/2</sub> = 31.7 eV and 4f<sub>5/2</sub> = 33.9 eV. One can rule-out the presence of metallic tungsten, W(0), as the W 4f spin-orbit components are positioned at 31.2 and 33.4 eV.<sup>181</sup> A previous XPS study on the aqueous electrochemical intercalation of Na<sup>+</sup>-ions into WO<sub>3</sub>-bpy showed that the only reduced species present was W<sup>5+</sup> with a W<sup>5+</sup>/W<sup>6+</sup> ratio of 0.5.<sup>84</sup> In the present study, the ratio of (total reduced species)/W<sup>6+</sup> ranges from 2 to 2.5, which highlights the reducing power of the implantation process in creating a highly reduced species in the form of "WO<sub>x</sub>" which is predominantly prepared through well-controlled oxidation of metallic tungsten<sup>182</sup> or the thermal reduction of WO<sub>3</sub>.<sup>181</sup> Considerable amounts of the implanted species were detected by XPS. The Na 1s peak is centred at 1071.4 eV with a FWHM of 1.6 eV. The Ca 2p appears as a doublet with binding energies of 343.9 and 347.4 eV and a FWHM of 1.6 eV, and the K 2p also appears as the doublet K 2p<sub>3/2</sub> and K 2p<sub>1/2</sub> with binding energies of 293.9 and 296.7 eV, respectively and a FWHM of 1.3 eV. Based on the XPS peak areas and corrected by the respective atomic sensitivity factors [W 4f = 3.52; Na 1s = 1.69; Ca 2p = 1.83; and K 2p = 1.47], the surface atomic ratios are found to be 0.78, 0.26, and 0.21 for Na/W, Ca/W, and K/W, and respectively. The trend is in good agreement with the relative amounts of intercalate obtained from single-crystal XRD refinements: WO<sub>3</sub>C<sub>5</sub>H<sub>4</sub>NNa<sub>0.125</sub>, WO<sub>3</sub>C<sub>5</sub>H<sub>4</sub>NCa<sub>0.05</sub> and WO<sub>3</sub>C<sub>5</sub>H<sub>4</sub>NK<sub>0.03</sub>, where Na<sup>+</sup>-implantation gives the largest amount of intercalate, whereas K<sup>+</sup>-implantation yields the least.

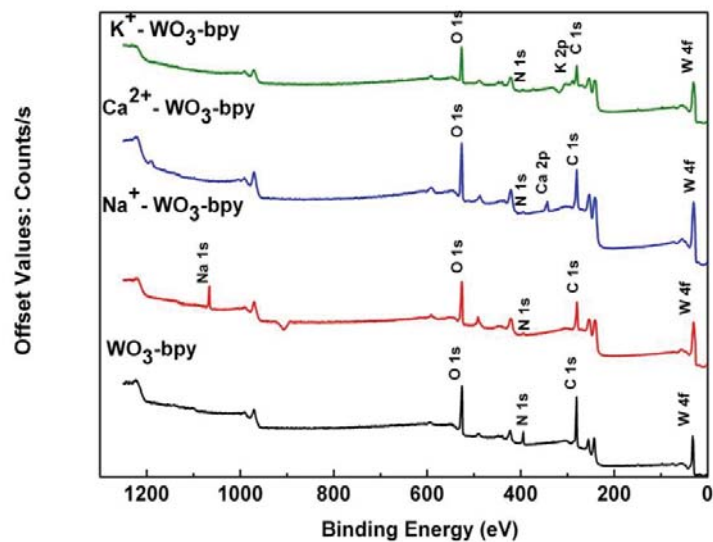


Figure 4.9 XPS scans of  $\text{WO}_3\text{-bpy}$  films before and after ion-implantation.

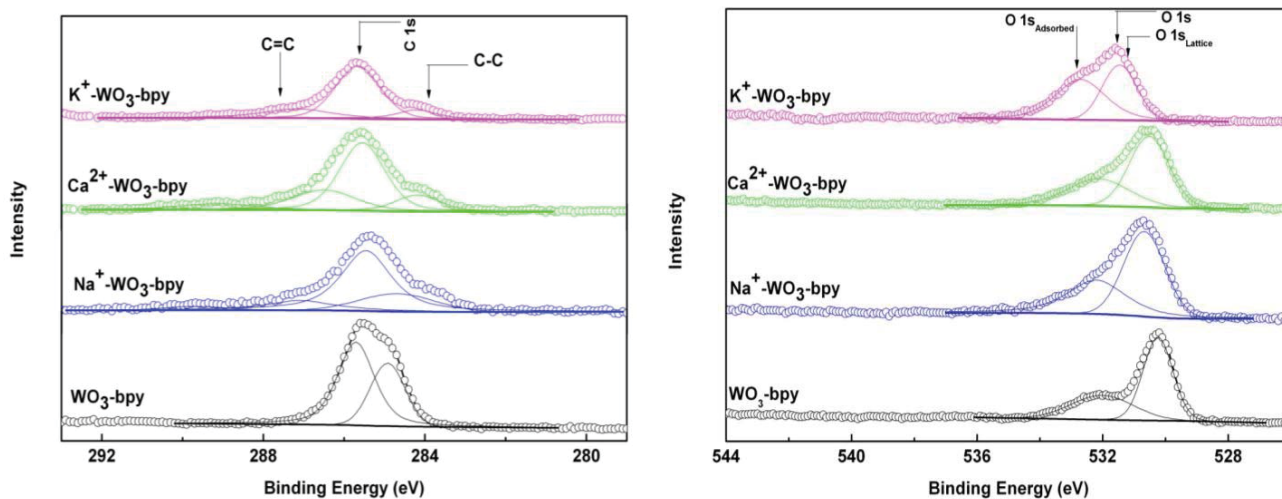
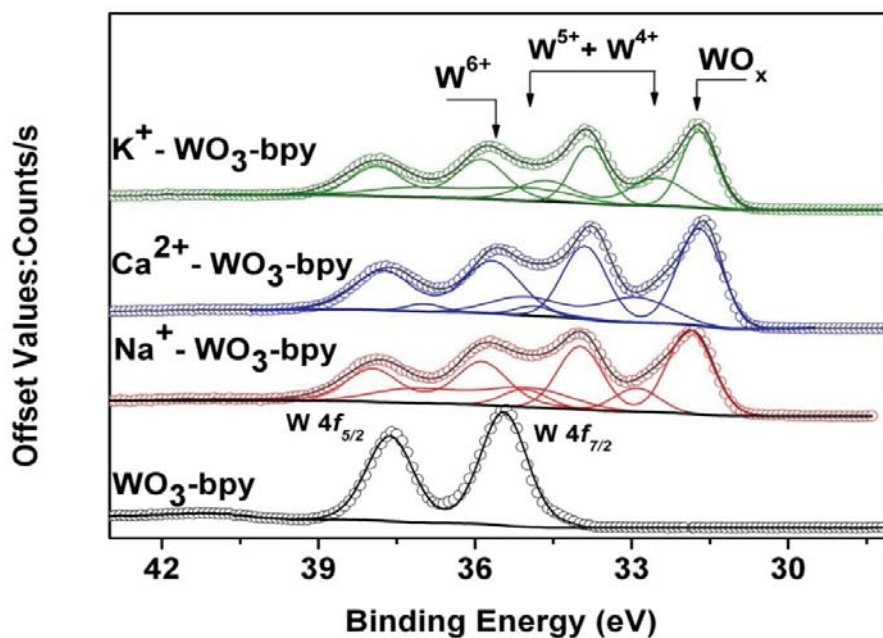
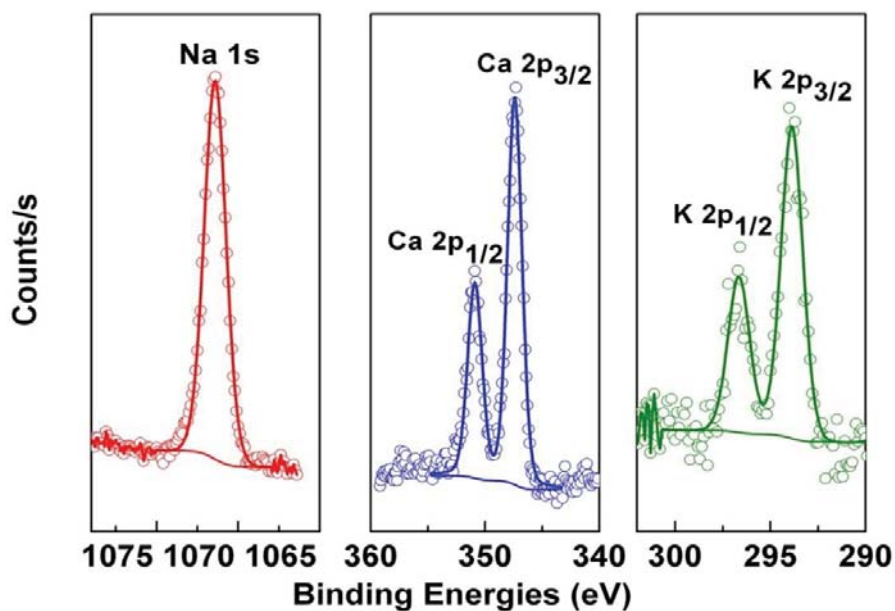


Figure 4.10 Deconvolution of XPS peaks C 1s (left) and O 1s (right) for non-implanted and implanted thick films of  $\text{WO}_3\text{-bpy}$ .



**Figure 4.11** Evolution of the W 4*f* XPS peaks upon ion-implantation. The arrows indicate the position of tungstate species with respect to the W 4*f*<sub>7/2</sub> peak.



**Figure 4.12** Intercalated species were detected by XPS for Ca 2*p*, K 2*p* and Na 1*s* in ion-implanted WO<sub>3</sub>-bpy films.

## 4.7 Resistivity Measurements

Fig. 4.13 shows the temperature dependence of the resistance for a  $\text{WO}_3$ -bpy film before and after  $\text{Ca}^{2+}$ -implantation. In both cases, an upturn in resistance with decreasing temperature could suggest a semiconducting behaviour for this material, and this is certainly the case for the non-intercalated material. However, these samples are very granular with poor intergranular links and the resistivity is therefore dominated by this granularity (see Fig. 4.3). So far it was not possible to carry out measurements on single crystals partly because of their small size, but also because they easily delaminate. Upon implanting the film with  $\text{Ca}^{2+}$  ions, the resistance decreases considerably, although it is still in the mega-ohms range and with semiconducting-like temperature dependence. However, the above-noted granularity could easily conceal the expected insulator to metal transition that is likely to occur with intercalation and which is certainly seen in doped  $\text{WO}_3$ .<sup>183</sup> The inset shows the voltage-current (V-I) behaviour of the  $\text{WO}_3$ -bpy films before and after  $\text{Ca}^{2+}$ -implantation at room temperature. Considerable hysteresis is observed in both curves, most probably due to weak-links between  $\text{WO}_3$ -bpy crystallites in the film. A decrease in resistance upon ion-implantation is also evident from the V-I curves which can be attributed to injection of charge carriers to a conduction band accompanied, as we note, by a putative insulator to metal transition.

These results suggest that there is a close correlation among Raman, XPS and resistivity measurements of implanted and non-implanted  $\text{WO}_3$ -bpy thick films. New shifts in Raman spectra and evolution of XPS  $\text{W}4f$  peak point to the fact that ion-implantation had significant effects on tungsten oxide layer without appreciably modifying the aromatic ligands. This leads to the reduction of tungsten species, from  $\text{W}^{6+}$  to  $\text{W}^{5+}$  and  $\text{W}^{4+}$ , and causes an increased conductivity of ion-implanted  $\text{WO}_3$ -bpy thick films suggesting the charge-carrier injection to the conduction band.

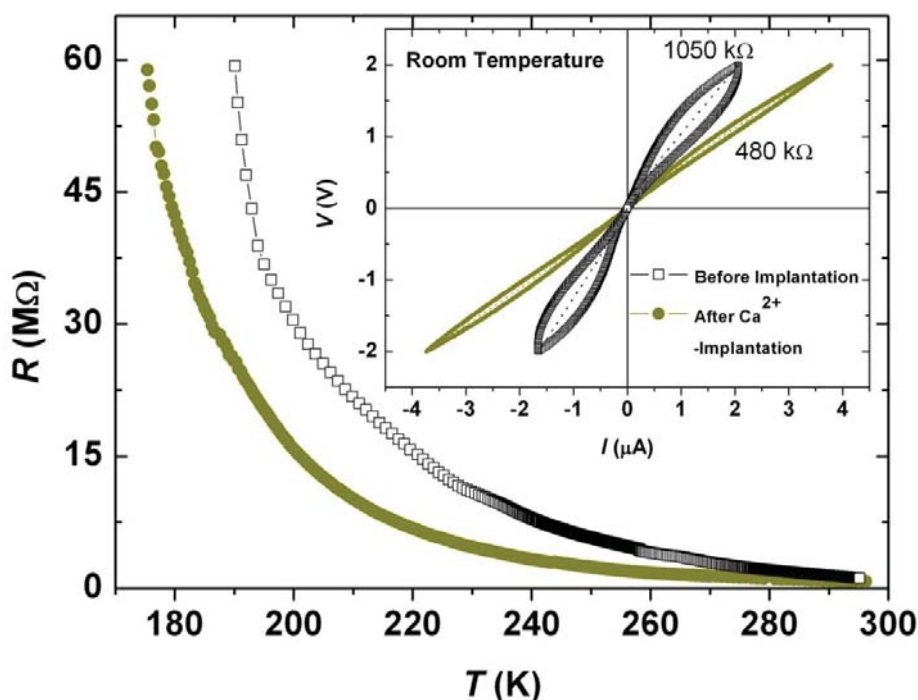


**Figure 4.13** Temperature dependence of the resistance of  $\text{WO}_3$ -bpy films before and after  $\text{Ca}^{2+}$  implantation. The inset shows the corresponding V-I curves measured at room temperature. The displayed resistances are calculated from dotted lines in the respective V-I curves.

## 4.8 Summary

We have prepared single crystals and films of the organic-inorganic hybrid material  $\text{WO}_3$ -bpy and investigated the effects of ion-implantation on its structural and physical properties. Powder diffraction studies of films deposited on substrate reveal the formation of a material that is similar to the crystalline material. Single-crystal XRD studies on the ion-implanted  $\text{WO}_3$ -bpy single crystals show the presence of intercalated species in the cage structures formed by bpy that coordinate the atomic layers of  $\text{WO}_5\text{N}$  octahedra. Photoelectron spectroscopy shows that ion-implantation results in the formation of reduced tungsten species which correlates with the darkened coloration of the sample. The appearance of new Raman modes upon ion implantation can be attributed to local broken symmetry, reduction of a significant fraction of W sites and interactions with implanted cations. The increased conductivity refers to the injection of charge carriers into the conduction band. The generic  $\text{MO}_3(4,4'\text{-bipyridyl})_{0.5}$  system ( $\text{M}=\text{W}, \text{Mo}$  or  $\text{V}$ ) and related materials represent a potentially phase-rich model system for exploring doping-dependent electronic properties and possible correlated states.

## Chapter 5

# Synthesis and characterization of novel single and bimetallic layered organic-inorganic hybrid materials

### 5.1 Introduction

Transition metal oxides exhibit excellent structural diversity, a broad compositional range and extensive chemical and physical properties making them ubiquitous in the rational design of novel metal oxide based organic-inorganic hybrids.<sup>69,184</sup> These hybrid materials display a wide range of electronic properties that can be manipulated to offer a range of applications including semiconductor, electrochromic and photochromic devices, materials for optical and medical uses, and high temperature superconductors.<sup>38,185,186</sup> One important method that is used to synthesize such hybrid materials is hydrothermal synthesis that exploits self-assembly processes and modifies the inorganic microstructures in order to give the hybrid framework.<sup>69,70</sup> This method has been exploited successfully by Borissevitch *et al* for the development of tungsten and molybdenum oxide based hybrid materials.<sup>187</sup> Depending upon the reaction conditions for synthesis and various other factors, such as nature of interaction between transition metal oxides and organic ligands, coordination preferences of transition metal oxides and the effect of secondary metal atom within the inorganic layers, the following three major classes of tungsten (or molybdenum) oxide hybrid materials have been reported: (1) solids where organonitrogen ligands act as spacer molecules between the inorganic layers, (2) two dimensional (2D) covalently bonded hybrid materials that consist of layers of inorganic metal oxides bridged by N- terminated ligands and (3) three dimensional (3D) hybrid frameworks containing bimetallic inorganic oxide layers covalently bonded to each other by organic ligands. With the synthesis of a large number of these three kinds of hybrid materials, it has been demonstrated quite successfully how small changes in ligand geometry can have profound structural consequences.<sup>79,188</sup> Therefore, in order to fully understand the physical and chemical properties of these hybrid materials, development of new ligand systems is essential. However, most of the reported hybrid materials contain

organic ligands such as diaminoalkanes, 2, 3, or 4-substituted pyridines such as 2,2'-bipyridine, 3,3'-bipyridine, 3,4'-bipyridine, 4,4'-bipyridine, pyrazine, 1,2,4-triazole, phenanthrolines and their derivatives.<sup>66,69,84</sup> Indeed, 1,10-phenanthroline is one of many aromatic-ring based ligand systems that offers diverse electronic properties and have been used as chelating agent in making hybrid materials (Fig. 5.1).<sup>189</sup> 1,10-phenanthroline and its derivatives represent one such ligand system that displays excellent chemical and structural features such as aromaticity, rigidity, planarity and chelating capability but has been ignored when it comes to bridging the metal ions.<sup>190</sup>



**Figure 5.1** A comparison of 1,10-phenanthroline (left) and 3,8-phenanthroline (right) structures.

To the best of author's knowledge, there aren't any reports of phenanthroline being used as covalent linker between the metal-oxide layers. Results described below attempt to investigate the role of 3,8-phenanthroline (herein "phen") ligands in bridging the metal-oxide layers. Specifically, this chapter describes synthesis of novel layered hybrid organic-inorganic materials, namely  $\text{WO}_3\text{-(3,8-phenanthroline)}_{0.5}$  (herein " $\text{WO}_3\text{-phen}$ "),  $\text{MoO}_3\text{-(3,8-phenanthroline)}_{0.5}$  (herein " $\text{MoO}_3\text{-phen}$ "),  $\text{CuMoO}_4\text{-(3,8-phenanthroline)}_{0.5}$  (herein " $\text{CuMoO}_4\text{-phen}$ ") and  $\text{Cu}_3\text{Cr}_2\text{O}_{10}\text{-(3,8-phenanthroline)}_{0.5}$  (herein " $\text{Cu}_3\text{Cr}_2\text{O}_{10}\text{-phen}$ ") where inorganic layers of transition metal oxides are bridged by phen ligands to give hybrid frameworks. In order to understand the structural, chemical and physical properties, these compounds have been characterized in detail by XRD, Raman spectroscopy and magnetic measurements.

## 5.2 Experimental Details

### 5.2.1 Synthesis

#### **WO<sub>3</sub>-phen**

Single-crystals of WO<sub>3</sub>-phen were prepared via hydrothermal reaction of WO<sub>3</sub>, phen and H<sub>2</sub>O using a molar ratio of 0.18:0.095:277 mM . The reactants were kept in a sealed Teflon-lined stainless-steel autoclave reactor at 160–170 °C for 120 hours before slowly cooling (approximately -10 °C per hour) the autoclave to room temperature. Light yellow platelet crystals of sizes *ca.* 30 x 60 μm were obtained upon filtration. Elemental analysis: C = 22.37 %, H = 1.25 %, N = 4.35 % (calculated); C = 20.05 %, H = 1.21 %, N = 3.89% (experimental).

#### **MoO<sub>3</sub>-phen**

Single-crystals of MoO<sub>3</sub>-phen were prepared via hydrothermal reaction of MoO<sub>3</sub>, phen and H<sub>2</sub>O using a molar ratio of 0.28:0.095:277 mM . The reactants were kept in a sealed Teflon-lined stainless-steel autoclave reactor at 160–170 °C for 70 hours before slowly cooling (approximately -10 °C per hour) the autoclave to room temperature. Dark green platelet crystals of sizes *ca.* 40 x 100 μm were obtained upon filtration. Elemental analysis: C = 30.72 %, H = 1.72 %, N = 5.99 % (calculated); C = 28.50 %, H = 1.70 %, N = 5.45% (experimental).

#### **CuMoO<sub>4</sub>-phen**

Single-crystals of CuMoO<sub>4</sub>-phen were prepared via hydrothermal reaction of MoO<sub>3</sub>, Cu<sub>2</sub>O, phen and H<sub>2</sub>O using a molar ratio of 0.14:0.14:0.095:277 mM . The reactants were kept in a sealed Teflon-lined stainless-steel autoclave reactor at 160–170 °C for 70 hours before slowly cooling (approximately -10 °C per hour) the autoclave to room temperature. Very thin needle-like crystals of sizes *ca.* 10 x 200 μm were obtained upon filtration. Elemental analysis: C = 22.37 %, H = 1.25 %, N = 4.35 % (calculated); C = 20.05 %, H = 1.21 %, N = 3.89% (experimental).

#### **Cu<sub>3</sub>Cr<sub>2</sub>O<sub>10</sub>-phen**

Single-crystals of Cu<sub>3</sub>Cr<sub>2</sub>O<sub>10</sub>-phen were prepared via hydrothermal reaction of CrO<sub>3</sub>, Cu<sub>2</sub>O, phen and H<sub>2</sub>O using a molar ratio of 0.1:0.07:0.055:139 mM . The reactants were kept in a sealed Teflon-lined stainless-steel autoclave reactor at 180 °C for 18 hours before slowly cooling (approximately -20 °C per hour) the autoclave to room temperature. Dark green

noncrystalline product was obtained with very few (approximately 10%) orange crystals. Few attempts to achieve phase purity remain unsuccessful.

## 5.2.2 Characterization

Powder and single crystal XRD, Raman and magnetic measurements were performed using the same instruments as described in sections 2.3 and 3.2. Lack of phase purity prevented the Raman and magnetic measurements on  $\text{Cu}_3\text{Cr}_2\text{O}_{10}$ -phen.

## 5.3 Single Crystal X-ray Diffraction

### 5.3.1 $\text{WO}_3$ -phen and $\text{MoO}_3$ -phen

The crystal structures of  $\text{WO}_3$ -phen and  $\text{MoO}_3$ -phen are closely isomorphous and, apart from small changes in the cell parameters resemble, interestingly, their bpy counterparts *i.e.*  $\text{WO}_3$ -bpy and  $\text{MoO}_3$ -bpy.<sup>70,90</sup> The asymmetric unit of  $\text{WO}_3$ -phen consists of a tungsten atom, two equatorial oxygen atoms, one apical oxygen atom and half a molecule of phen while the unit cell for  $\text{MoO}_3$ -phen is a bit larger in the volume but has atomic arrangement similar to  $\text{WO}_3$ -phen (Fig. 5.2).

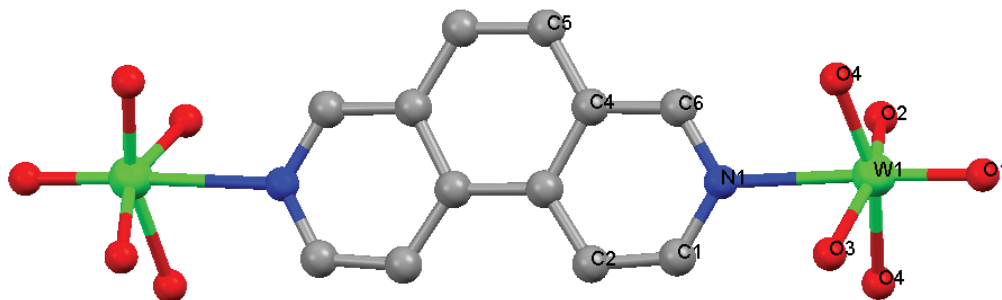


**Figure 5.2** Crystal repeat unit for  $\text{MO}_3$ -phen (where  $M = \text{W}$  or  $\text{Mo}$ ).  $\text{O}_2$  and  $\text{O}_3$  have 50% occupancy for both structures making metal-oxide ratio to 1:3. Hydrogen atoms are omitted for clarity.

$\text{WO}_3$ -phen and  $\text{MoO}_3$ -phen both crystallize in the *Cmca* space group. Infinite layers of corner-shared octahedral tungsten or molybdenum oxide exist in the *ab*-plane. These inorganic layers are bridged through phen ligands that coordinate axially to metal atoms and form 3D hybrid organic-inorganic network (Fig. 5.3). The octahedral coordination geometry at each metal atom site is defined by one terminal oxo group, four bridging oxo groups and a

nitrogen donor from phen ligand. The strong influence of terminal oxo groups is reflected in long W(1)–N(1) (2.437(7) Å) and Mo(1)–N(1) (2.419(11) Å) bond distances, while the terminal oxo bond lengths, W(1)=O(1) (1.711(7) Å) and Mo(1)=O(1) (1.699(9) Å), and bridging oxo bond lengths which range from 1.816 Å to 1.892 Å for WO<sub>3</sub>-phen and 1.776 Å to 1.883 Å for MoO<sub>3</sub>-phen, are within the oxo bond lengths expected for tungsten and molybdenum oxides.<sup>70,130,147</sup> The bridging oxygen bonds, W(1)–O(1)–W(1) and Mo(1)–O(4)–Mo(1), almost run parallel to the short *b*-axis and are nearly non-linear owing to the angles of 178.7(4) and 179.1(3) degrees respectively. However, the remaining bridging oxygen bonds, W(1)–O(2)–W(1), W(1)–O(3)–W(1), Mo(1)–O(2)–Mo(1), and Mo(1)–O(3)–Mo(1), are parallel to the longer *c*-axis and are non-linear with their respective angles of 156.3(7), 169.7(3), 153.1(8) and 163.8(9) degrees. These changes in bond angles are nicely consistent with the way the unit cell changes in the *b* and *c* directions for both compounds. The axial (W=O and Mo=O) and metal-ligand (W–N and Mo–N) bonds of metal-oxide octahedra alternate in direction in both *a* and *b* directions, leading to undulating WO<sub>4</sub> and MoO<sub>4</sub> layers in the *ab* plane. Refer to Table 5.1 for key structural and refinement details.

The phen group and the axial oxygen atom are well ordered, however, the equatorial oxygen atoms are stochastically disordered on either side of the line joining pairs of metal atoms. All the residual electron density was concentrated near the metal oxide planes and none of it was around the phen ligands, suggesting possible disorder. However, close inspection of data frames revealed no missing weak reflections and hence no attempt was made to model this disorder. Despite the similar bond distances, there is doubling of an axis for WO<sub>3</sub>-phen and MoO<sub>3</sub>-phen as compared to their bpy counterparts and hence a larger unit cell volume for the phen based compounds. Despite the similar herringbone alignment of organic ligands in both systems, the packings of the organic ligands in these compounds are distinctly different:  $\pi$ -stacking for phen in WO<sub>3</sub>-phen and MoO<sub>3</sub>-phen as compared to eschew  $\pi$ -stacking of the bpy ligands in WO<sub>3</sub>-bpy and MoO<sub>3</sub>-bpy. Therefore the cages defined by WO<sub>3</sub>-phen and MoO<sub>3</sub>-phen are much smaller than those formed in WO<sub>3</sub>-bpy and MoO<sub>3</sub>-bpy which limits the possibilities of introducing even very small metal atoms there (Fig. 5.3).

**Table 5.1** Selected crystallographic and refinement details for WO<sub>3</sub>-phen and MoO<sub>3</sub>-phen hybrids.

<b>Parameter</b>	<b>WO<sub>3</sub>-phen</b>	<b>MoO<sub>3</sub>-phen</b>
<i>a</i> (Å)	22.6294(4)	22.7233(4)
<i>b</i> (Å)	7.5777(10)	7.7355(10)
<i>c</i> (Å)	14.7923(10)	14.5903(10)
$\alpha, \beta, \gamma$ (°)	90, 90, 90	90, 90, 90
<i>V</i> (Å <sup>3</sup> )	2536.63(18)	2564.63(18)
Crystal system	Orthorhombic	Orthorhombic
Space group	<i>Cmca</i>	<i>Cmca</i>
Data range (°/Å)	20-0.81	20-0.81
Completeness (%)	97.2	99.0
Redundancy	4.92	12.484
<i>R</i> <sub>int</sub> , <i>R</i> <sub>sigma</sub> (%)	5.28, 3.95	9.89, 5.43
Asymm. unit	WO <sub>3</sub> C <sub>6</sub> H <sub>4</sub> N	MoO <sub>3</sub> C <sub>6</sub> H <sub>4</sub> N
<i>R</i> 1(obs), #data*	0.0318, 856	0.0548, 651
<i>R</i> 1(all), #data	0.0448, 1039	0.0615, 804
<i>wR</i> 2 (all data)	0.0814	0.1751
Resid. Density	2.50, -1.68	1.30, -1.72

\*  $I > 2\sigma(I)$

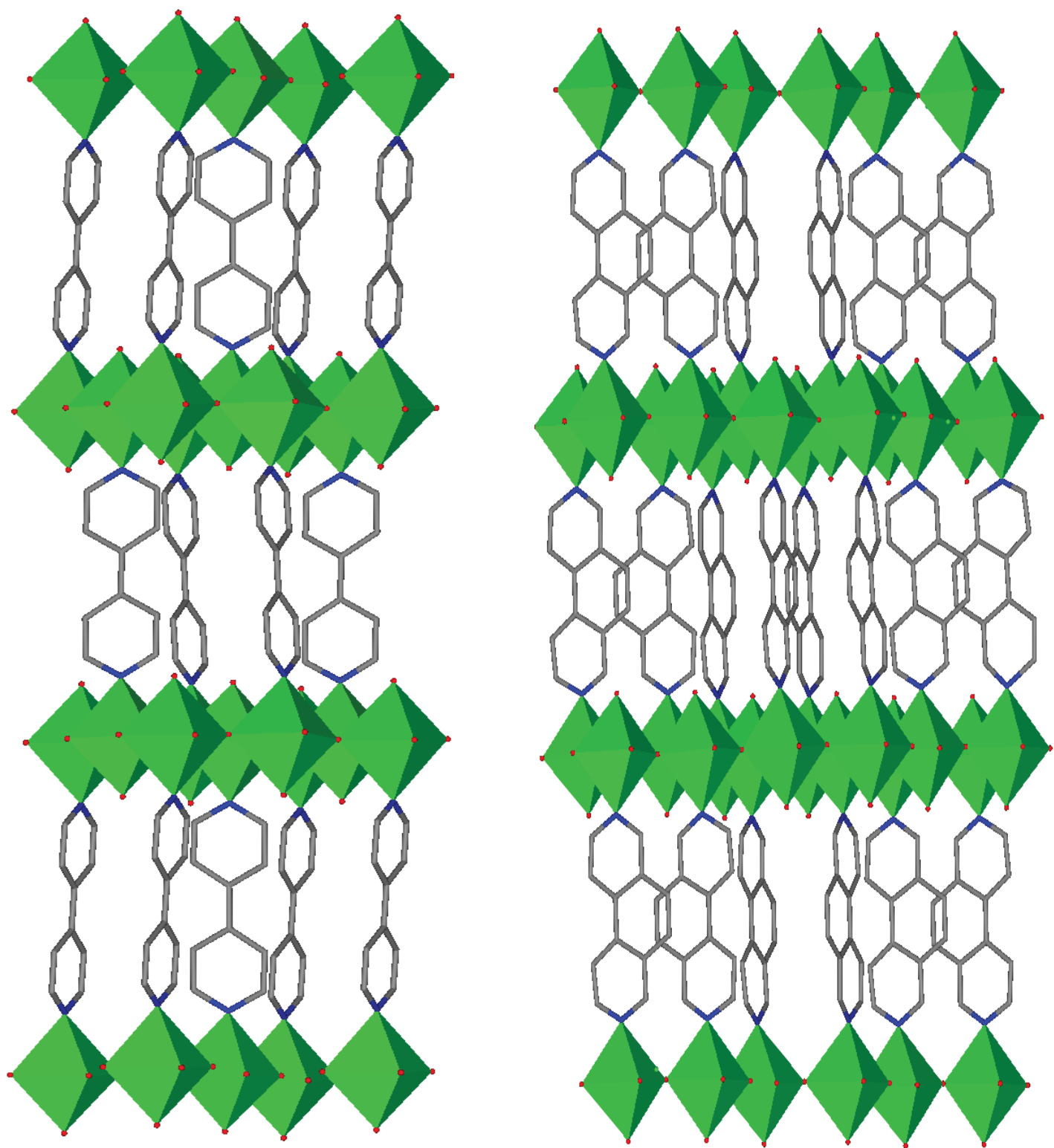


**Figure 5.3** A comparison of ligand-packing for WO<sub>3</sub>-bpy (left) and WO<sub>3</sub>-phen (right) structures. It can be noted that the cavity between apical oxygens is much smaller for WO<sub>3</sub>-phen as compared to that of WO<sub>3</sub>-bpy. Colour scheme is similar to Fig.5.2.

### 5.3.2 CuMoO<sub>4</sub>-phen

The crystal structure of CuMoO<sub>4</sub>-phen consists of alternating bimetallic layers of inorganic metal oxides that are bridged together by phen ligands in order to form a 3D framework. The bimetallic oxide layers, which propagate in the *ab*-plane, are constructed from two types of atoms with different coordination environments: tetrahedrally coordinated molybdenum and octahedrally coordinated copper. Thus each layer consists of discrete tetranuclear units of edge-sharing copper oxide (CuO<sub>5</sub>N) octahedra interconnected by corner-shared molybdenum oxide (MoO<sub>4</sub>) tetrahedra (Fig. 5.4). The phen ligands interlink the adjacent bimetallic layers through Cu–N bridging interactions thus generating the complete structure as shown in Fig.5.4.

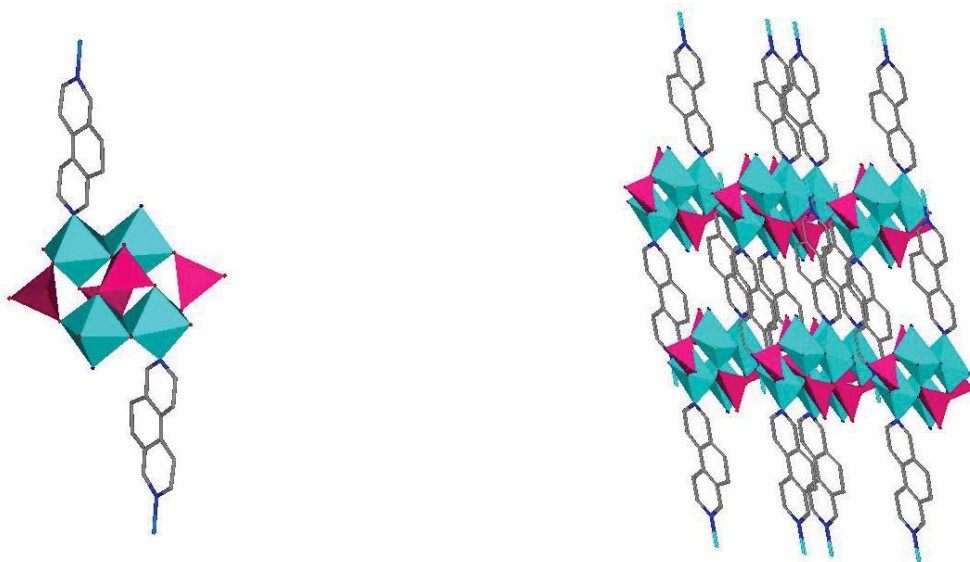


**Figure 5.4** Crystal structure of CuMoO<sub>4</sub>-phen. A structural motif (left) and a complete structure (right) is generated by bimetallic layers of edge-shared copper oxide octahedra and corner shared molybdenum oxide tetrahedra in the *ab*-plane while ligands interconnect the inorganic layers to form a 3D covalent framework. Hydrogen atoms are omitted for clarity. Copper is displayed in cyan, molybdenum in pink, oxygen in red, nitrogen in blue and carbon in grey.

Five oxo groups from five corner-shared molybdenum oxide tetrahedra and a nitrogen donor from phen define the coordination geometry at each Cu(II) site while the coordination geometry at each Mo(VI) site is defined by four oxo groups. However, in contrast to a single Cu(II) site throughout the each bimetallic inorganic oxide layer, there are two distinct

molybdenum sites where the coordination geometry at Mo(2) is composed of three bridging oxo groups that are involved in Mo–O–Cu bridging and a terminal oxo group which is not linked to copper clusters. The coordination geometry at Mo(1) is defined by four oxo groups that are all involved in Mo–O–Cu bonding interactions. Fig.5.5 elaborates the coordination geometries at Cu(II) and Mo(VI) sites.

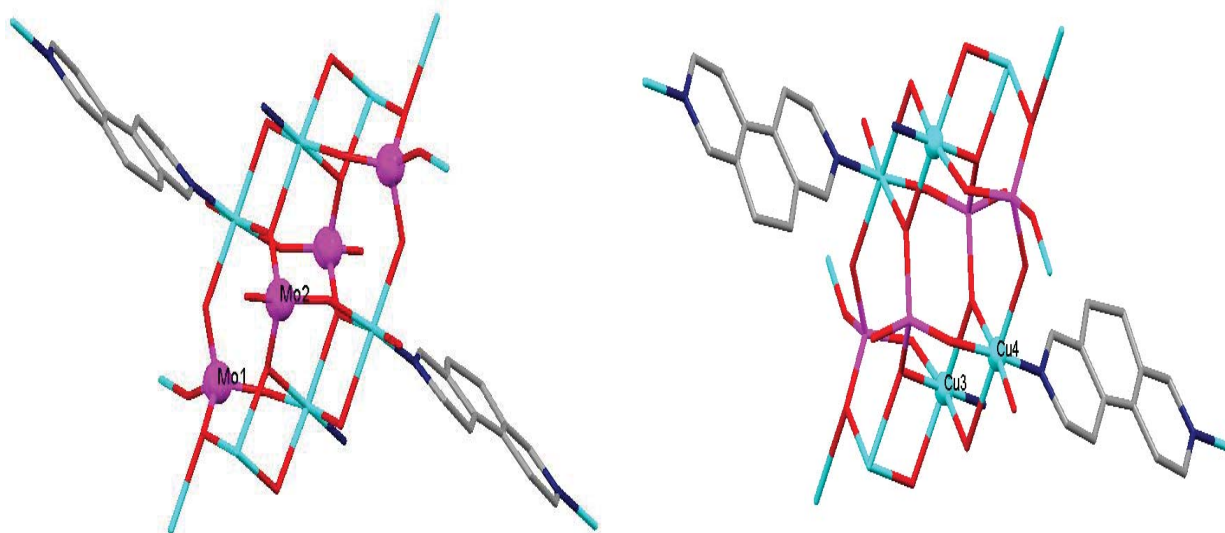


**Figure 5.5** Coordination geometries for Mo (left) and Cu (right) sites. Both Cu(3) and Cu(4) have similar six coordination. Although both Mo(1) and Mo(2) are four coordinated, the coordination at Mo(1) is defined by four bridging oxo while for Mo(2) it is composed of three bridging oxo and a terminal group. Colour scheme similar to Fig. 5.4.

The terminal oxo Mo(2)=O(6) (1.72(4) Å) and bridging oxo, O(5)–Mo(2)–O(7) (1.8 Å, on average, for each Mo–O bond) bond lengths are, on average, within the expected bond length range for molybdenum oxides.<sup>130,147,191</sup> However, the axial Cu–O bond distances, Cu(1)–O(1) (2.25(4) Å), Cu(1)–O(3) (2.45(3)) and Cu(2)–O(5) (2.34(4) Å), Cu(2)–O(7) (2.27(4) Å) are significantly larger than equatorial bonds, Cu(1)–O(2) (1.91(4) Å), Cu(1)–O(5) (2.04(4) Å), Cu(1)–O(8) (1.99(3) Å), and Cu(2)–O(3) (2.05(3) Å), Cu(2)–O(4) (1.97(3) Å). This can be attributed to Jahn-Teller distortions as expected for Cu<sup>2+</sup> which has been observed previously in similar compounds such as CuMoO<sub>4</sub>, CuCrO<sub>4</sub>, and Cu<sub>3</sub>Mo<sub>2</sub>O<sub>8</sub> etc.<sup>192,193</sup> The metal-ligand distances Cu(1)–N(1) (1.98(4) Å) and Cu(2)–N(2) (1.90(5) Å) are similar to the already reported copper oxide hybrids.<sup>191</sup> The interlayer spacing for CuMoO<sub>4</sub>-phen is 7.47 Å, which is significantly larger than those of WO<sub>3</sub>-phen (3.880 Å) and MoO<sub>3</sub>-

phen (3.876 Å) which shows that interlayer distance does not only reflect the addition of more atoms into the ligand tether but also on the number of atoms in the inorganic oxide layers.

### 5.3.3 $\text{Cu}_3\text{Cr}_2\text{O}_{10}$ -phen

Replacing Mo with Cr in the inorganic-oxide layer of  $\text{CuMoO}_4$ -phen gives rise to significant structural changes in the resulting compound i.e.  $\text{Cu}_3\text{Cr}_2\text{O}_{10}$ -phen. Fig.5.6 shows the asymmetric unit cell for  $\text{Cu}_3\text{Cr}_2\text{O}_{10}$ -phen consists of two Cu atoms, one Cr atom, five oxygens and half a ring of phen. An inversion centre is present at the midpoint of the bond between atoms C4 and C4' hence the central aromatic ring of the phen ligand is disordered by symmetry. The complete crystal structure of  $\text{Cu}_3\text{Cr}_2\text{O}_{10}$ -phen comprises alternating bimetallic layers of inorganic metal oxides that are bridged together by phen ligands in order to form a 3D framework.

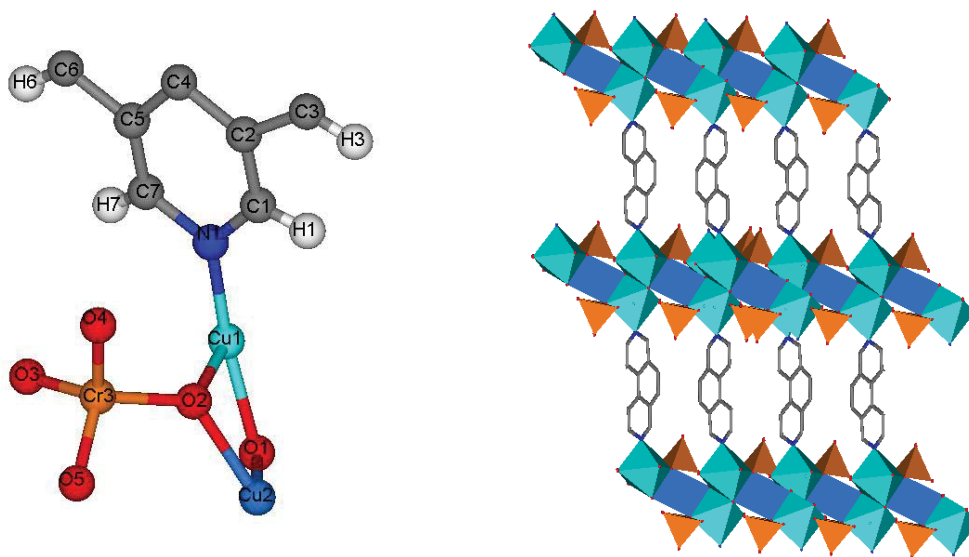


**Figure 5.6** Crystal repeat unit of  $\text{Cu}_3\text{Cr}_2\text{O}_{10}$ -phen (left) and complete structure (right). Colour scheme is same in both figures. Hydrogens and disordered carbon atoms are removed from right side figure for clarity.

First consider the bimetallic oxide layer of  $\text{Cu}_3\text{Cr}_2\text{O}_{10}$ -phen which is composed of three types of metal ions with different coordination environments (Fig. 5.7). Each Cr atom is coordinated to four oxo groups. Three oxo groups are involved in Cr–O–Cu bridging interactions while the remaining atomic site around Cr is occupied by a terminal oxygen atom that points outward from bimetallic layer. Since bond distances of terminal oxo (1.60(19) Å) and bridging oxo groups (1.64-1.76 Å) are similar to those described in previous studies of compounds involving tetrahedral chromium(VI) oxide (terminal oxo: 1.61-1.63 Å, bridging oxo: 1.62-1.79 Å), therefore an oxidation state of +6 is assigned to chromium in  $\text{Cu}_3\text{Cr}_2\text{O}_{10}$ -phen.<sup>192,194</sup> The respective bond angles (108.8 to 110.4 degrees) suggest a tetrahedral geometry for Cr(VI)O<sub>4</sub>.

There are two distinct Cu sites in the inorganic layer: Cu(1) and Cu(2). Cu(2) sits on a special position and makes coordinated bonds with two bridging oxo groups that are involved in Cu–O–Cr bridging interactions and two oxo groups that are employed in Cu–O–Cu bridging. All of these bonds have identical distances of 1.93(2) Å. Moreover, these bond distances are well within the range of equatorial Cu–O bond lengths observed in previously reported copper-oxide based bimetallic hybrids such as  $\text{CuMoO}_4$ -bpy (1.95-2.02 Å) and  $\text{Cu}_3(\text{CrO}_4)_2(\text{OH})_2(\text{bpy})_2$  (1.94-2.0 Å).<sup>191,192</sup> Based on this comparison an oxidation state of +2 is assigned to Cu(2). Bond angles (83 to 180 degrees) for bridging interactions involving Cu(2) suggest a square-planar geometry.

Contrary to Cu(2), Cu(1) sits on a general position and is fully occupied. Approximate octahedral coordination for Cu(1) is defined by three bridging oxo groups that are involved in Cr–O–Cu bridging interactions, two oxo groups that are employed in Cu–O–Cu interactions and a nitrogen donor from organic ligand. The axial and equatorial Cu(1)–O bond lengths as well as metal-ligand bond lengths (axial: 2.31-2.45 Å, equatorial: 1.95-1.99 Å, Cu(1)–N : 1.91(2)) are similar for  $\text{Cu}_3\text{Cr}_2\text{O}_{10}$  and other related compounds ( $\text{CuMoO}_4$ -phen (axial: 2.31-2.48 Å, equatorial: 1.96-1.97 Å, Cu–N: 1.90-1.98 Å),  $\text{CuMoO}_4$ -bpy (equatorial: 1.94-2.02 Å, axial: 2.27-2.38 Å, Cu–N: 1.98-2.0 Å),  $\text{Cu}_3(\text{CrO}_4)_2(\text{OH})_2(\text{bpy})_2$  (equatorial: 1.94-2.0 Å, axial: 2.32-2.44 Å, Cu–N: 2.0 Å)). In these previously reported compounds, organic ligand-coordinated copper is assigned an oxidation state of +2. For example, in  $\text{Cu}_3(\text{CrO}_4)_2(\text{OH})_2(\text{bpy})_2$ , which is very similar to the  $\text{Cu}_3\text{Cr}_2\text{O}_{10}$ -phen, charges are balanced by attributing one oxygen atom, involved in bridging copper atoms, a hydroxyl. However, despite closely inspecting crystallographic data for  $\text{Cu}_3\text{Cr}_2\text{O}_{10}$ -phen no protons could be located within a reasonable distance of oxo groups to be assigned as hydroxyl. Therefore,

Cu(1) in  $\text{Cu}_3\text{Cr}_2\text{O}_{10}$ -phen appears to be trivalent. Bond valence sum calculations (Appendix A) further strengthen this possibility where a valence of 2.002, 2.5872 and 5.7374 were calculated for Cu(2), Cu(1) and Cr(3) respectively. Based on all the crystallographic information and requirement for charge balance an oxidation state of +3 is tentatively assigned for Cu(1) site in  $\text{Cu}_3\text{Cr}_2\text{O}_{10}$ -phen.

Thus each inorganic layer consists of discrete units of edge-sharing copper oxide ( $\text{CuO}_5\text{N}$ ) octahedra and square-planar copper oxide ( $\text{CuO}_4$ ) interconnected by corner-shared chromium oxide ( $\text{CrO}_4$ ) tetrahedra (Fig. 5.7). The phen ligands interlink the adjacent bimetallic layers through Cu–N bridging interactions thus generating the complete structure as shown in Fig.5.6. The interlayer spacing of 5.63 Å is significantly larger than those of  $\text{WO}_3$ -phen (3.880 Å) and  $\text{MoO}_3$ -phen (3.876 Å) reflecting the increased number of atoms in the inorganic-oxide layer. However, the interlayer spacing is significantly smaller than that of  $\text{CuMoO}_4$ -phen, possibly, because of the smaller sized metal atoms in the inorganic oxide layer of  $\text{Cu}_3\text{Cr}_2\text{O}_{10}$ -phen.

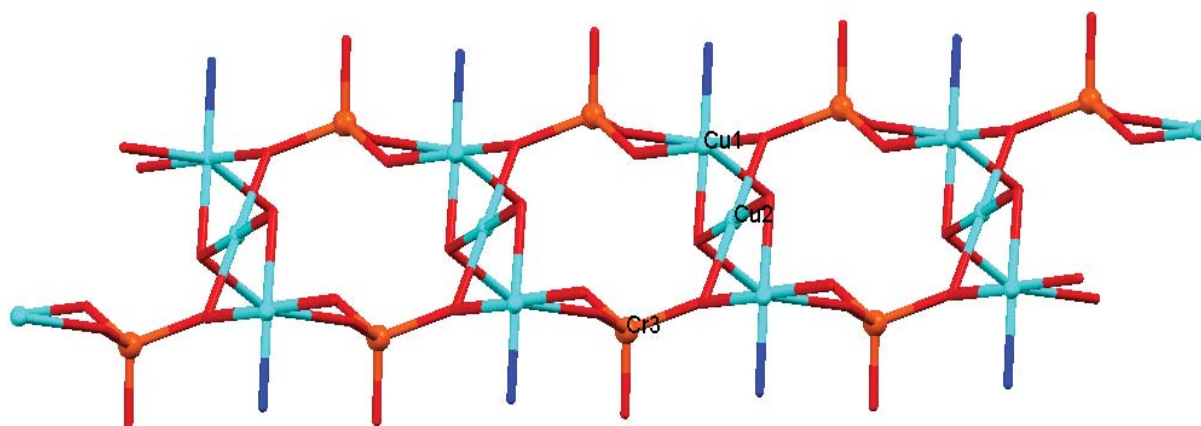


**Figure 5.7** A metal-oxide inorganic layer of  $\text{Cu}_3\text{Cr}_2\text{O}_{10}$ -phen demonstrating coordination geometries of the three metal ion sites.

**Table 5.2** Selected crystallographic and refinement details for CuMoO<sub>4</sub>-phen and Cu<sub>3</sub>Cr<sub>2</sub>O<sub>10</sub>-phen hybrids.

Parameter	CuMoO <sub>4</sub> -phen	Cu <sub>3</sub> Cr <sub>2</sub> O <sub>10</sub> -phen
<i>a</i> (Å)	7.4173(5)	5.6292(7)
<i>b</i> (Å)	9.2259(7)	5.6494(6)
<i>c</i> (Å)	13.8144(10)	13.7959(13)
$\alpha, \beta, \gamma$ (°)	72.173, 89.886, 73.221	92.654, 90.330, 109.093
<i>V</i> (Å <sup>3</sup> )	857.75(11)	414.05(8)
Crystal system	Triclinic	Triclinic
Space group	<i>P</i> -1	<i>P</i> -1
Data range (Å)	20-0.99	20-0.90
Completeness (%)	99.2	89
Redundancy	4.98	3.55
<i>R</i> <sub>int</sub> , <i>R</i> <sub>sigma</sub> (%)	33.42, 41.10	13.36, 15.18
Asymm. unit	CuMoO <sub>4</sub> C <sub>6</sub> H <sub>4</sub> N	Cu <sub>3</sub> Cr <sub>2</sub> O <sub>10</sub> C <sub>12</sub> H <sub>8</sub> N <sub>2</sub>
<i>R</i> 1(obs), #data*	0.1715, 648	0.199, 717
<i>R</i> 1(all), #data	0.3169, 1836	0.227, 1061
<i>wR</i> 2 (all data)	0.4350	0.5151
Resid. Density	4.30, -1.76	1.35, -1.86

\*  $I > 2\sigma(I)$

Based on the above structural analysis it can be said that phen-based single and bimetallic layered hybrids offer great structural diversity which arises not only from ligand geometry but also from coordination preferences of the metal components. Various experimental techniques can be used to further understand the influence of different ligands and metal components on the chemical and physical properties of layered hybrid networks. Powder X-ray diffraction, Raman spectroscopy and magnetic measurements were used for further analysis of these compounds and the following section comprises some of the results obtained from these measurements.

## 5.4 Powder X-ray Diffraction

Powder XRD was used as a preliminary tool to probe the structure of hybrid materials. Fig. 5.8 shows that the powder XRD pattern of  $\text{WO}_3$ -phen consists of sharp, well-defined reflections which represent the formation of a layered structure. A similar diffraction pattern was calculated from single-crystal XRD measurements of  $\text{WO}_3$ -bpy which suggests that the given material possesses identical layered structure in both, the bulk and crystalline forms. Likewise, experimental and calculated powder XRD patterns of  $\text{MoO}_3$ -phen,  $\text{CuMoO}_4$ -phen and  $\text{Cu}_3\text{Cr}_2\text{O}_{10}$ -phen suggest the formation of layered structure in crystalline and bulk forms. (Figs. 5.9-5.12) The powder XRD patterns are almost identical for  $\text{MoO}_3$ -phen and  $\text{WO}_3$ -phen suggesting similar lattice parameters for both structures, however, the powder XRD pattern for  $\text{CuMoO}_4$ -phen and  $\text{Cu}_3\text{Cr}_2\text{O}_{10}$ -phen are significantly different than those of  $\text{WO}_3$ -phen and  $\text{MoO}_3$ -phen. This can be attributed to the presence of additional metal atoms in the inorganic oxide layer of  $\text{CuMoO}_4$ -phen and  $\text{Cu}_3\text{Cr}_2\text{O}_{10}$ -phen which suggests significant changes in lattice parameters that were confirmed from the single-crystal XRD measurements.

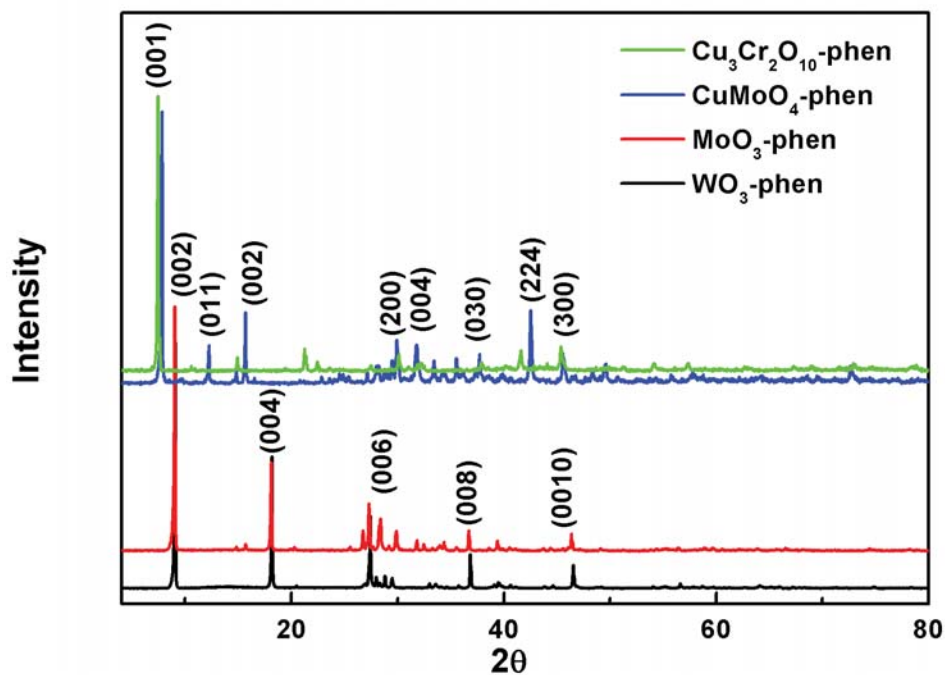


**Figure 5.8** Powder X-ray diffractograms for  $\text{WO}_3\text{-phen}$ ,  $\text{MoO}_3\text{-phen}$ ,  $\text{CuMoO}_4\text{-phen}$  and  $\text{Cu}_3\text{Cr}_2\text{O}_{10}\text{-phen}$ . The diffraction angle is for  $\text{Co K}\alpha$  radiation. The intensities were scaled in both figures for better comparison. Intensity is measured in arbitrary units and Bragg angle in degrees.

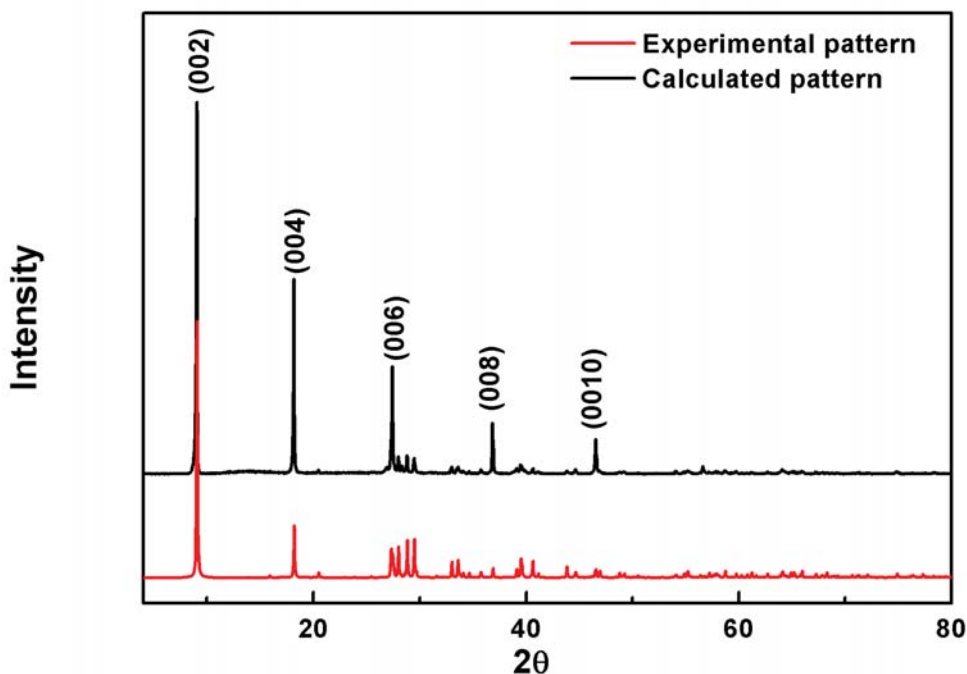


**Figure 5.9** A comparison of experimental and calculated powder X-ray patterns for  $\text{WO}_3\text{-phen}$ . For comparison, the wavelength was changed to  $\text{Co K}\alpha$  in the pattern calculated from the single crystal structure of  $\text{WO}_3\text{-phen}$ , which was determined with  $\text{Cu K}\alpha$  radiation.

Intensity is measured in arbitrary units and Bragg angle in degrees.

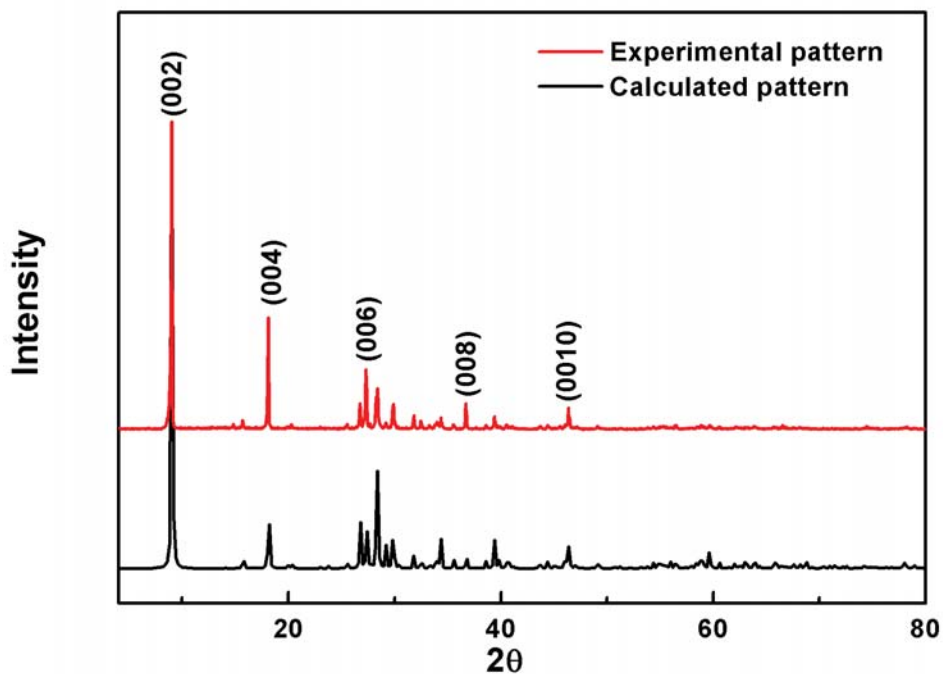


**Figure 5.10** A comparison of experimental and calculated powder X-ray patterns for MoO<sub>3</sub>-phen. For comparison, the wavelength was changed to Co K $\alpha$  in the pattern calculated from the single crystal structure of MoO<sub>3</sub>-phen, which was determined with Cu K $\alpha$  radiation. Intensity is measured in arbitrary units and Bragg angle in degrees.

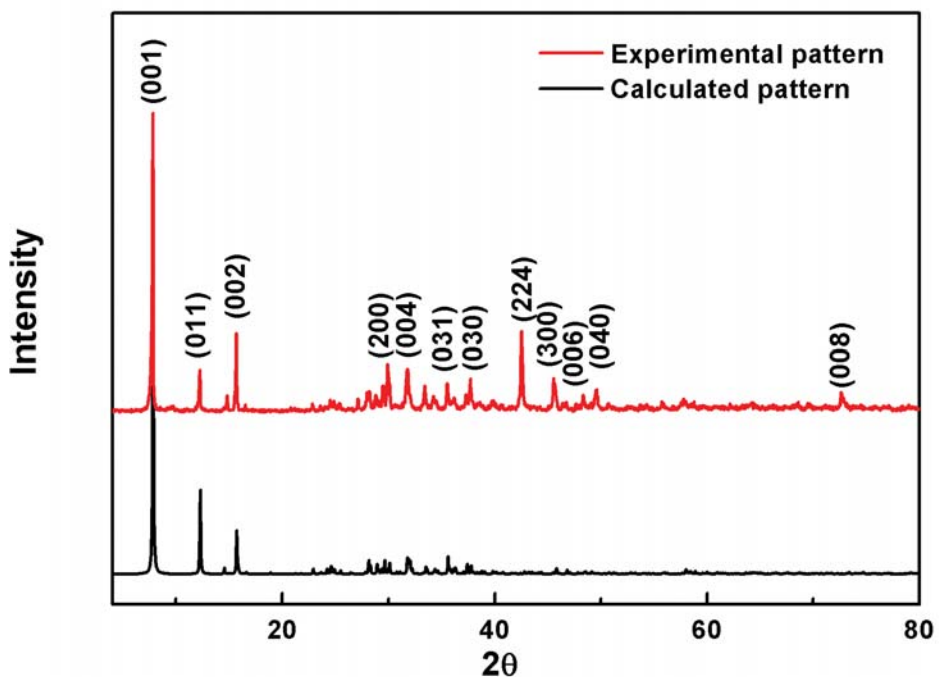


**Figure 5.11** A comparison of experimental and calculated powder X-ray patterns for CuMoO<sub>4</sub>-phen. For comparison, the wavelength was changed to Co K $\alpha$  in the pattern calculated from the single crystal structure of CuMoO<sub>4</sub>-phen, which was determined with Cu K $\alpha$  radiation. Intensity is measured in arbitrary units and Bragg angle in degrees.

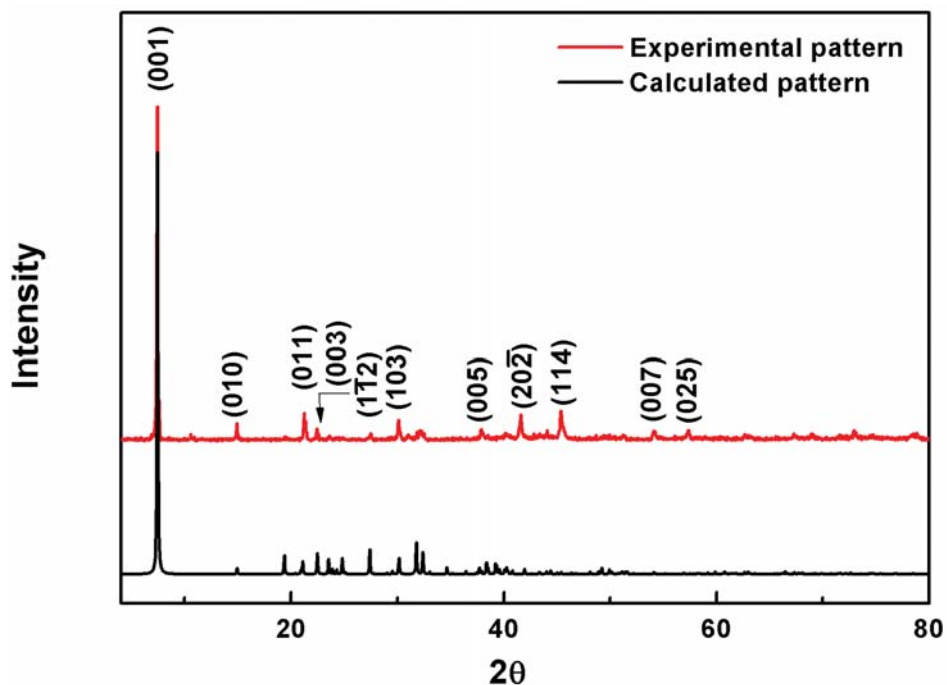


**Figure 5.12** A comparison of experimental and calculated powder X-ray patterns for  $\text{Cu}_3\text{Cr}_2\text{O}_{10}$ -phen. For comparison, the wavelength was changed to Co  $K\alpha$  in the pattern calculated from the single crystal structure of  $\text{Cu}_3\text{Cr}_2\text{O}_{10}$ -phen, which was determined with Cu  $K\alpha$  radiation. Intensity is measured in arbitrary units and Bragg angle in degrees.

## 5.5 Raman Spectroscopy

The Raman spectrum of  $\text{WO}_3$ -phen contains characteristic vibrational modes which correspond to both the organic and inorganic components of the hybrid network (Fig. 5.13). The broad peak at  $675\text{ cm}^{-1}$  is identified as stretching O–W–O vibration. A similar mode has been reported at  $645\text{ cm}^{-1}$  for  $\text{WO}_3$  and  $\text{WO}_3$ -bpy systems.<sup>74,91,131</sup> The apparent red shift in the position of this mode for  $\text{WO}_3$ -phen is quite intriguing and can be explained in a sense that equatorial bond angles for  $\text{WO}_3$ -bpy ( $92.41^\circ$ ) and  $\text{WO}_3$ -phen ( $95.30^\circ$ ) are quite different. A very sharp peak at  $938\text{ cm}^{-1}$  is assigned to the stretching vibration of terminal oxygen (W=O) and it happens to be at similar position in the Raman spectra of  $\text{WO}_3$ -bpy.<sup>74,90,91</sup> Once again this can be explained with the help of single-crystal X-ray data which suggests that terminal oxygen bond lengths are very similar for  $\text{WO}_3$ -bpy and  $\text{WO}_3$ -phen. Raman modes due to aromatic rings in phen appear at  $1067\text{ cm}^{-1}$ ,  $1256\text{ cm}^{-1}$ ,  $1295\text{ cm}^{-1}$ ,  $1355\text{ cm}^{-1}$ ,  $1437\text{ cm}^{-1}$ ,  $1538\text{ cm}^{-1}$  and are assigned to various stretching and bending vibrations caused by aromatic rings in phen.<sup>132,195,196</sup> Due to

enormous fluorescence background signal in the Raman spectra of phen it was not possible to identify distinct vibrational bands. No experimental Raman spectrum of phen appears in the literature, presumably due to the fluorescence background signal. A comparison between calculated and experimental Raman spectra of 1,10-phenanthroline reveals that most significant vibrational modes appear at similar positions (Fig. 5.14). This suggests that experimental Raman spectra of phen would also be very similar to its calculated version. Hence, all the mode assignments in phen based hybrids were made from calculated phen spectrum alone (Fig. 5.15).

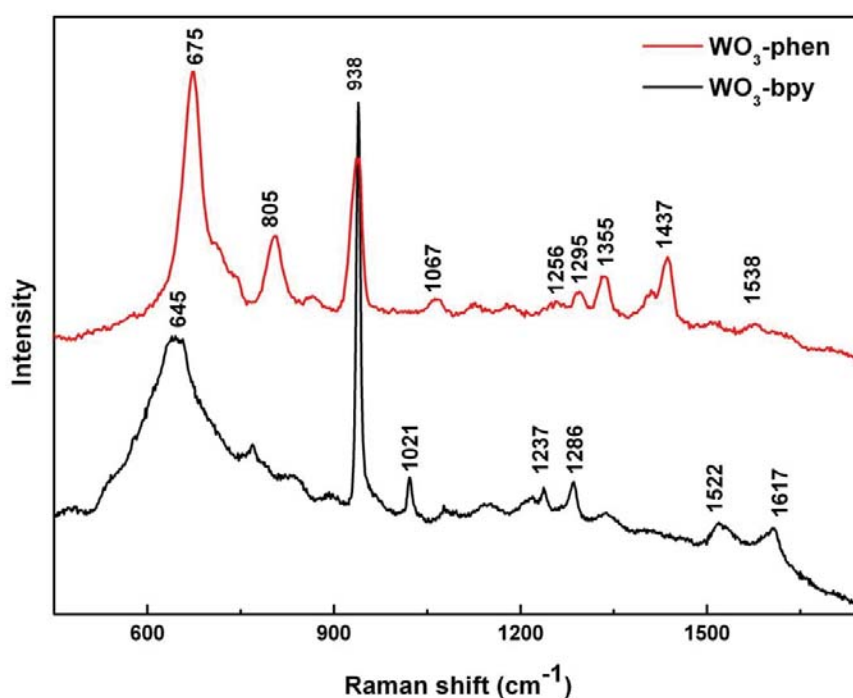


**Figure 5.13** A comparison of Raman spectra of WO<sub>3</sub>-phen and WO<sub>3</sub>-bpy. Intensity is measured in arbitrary units.

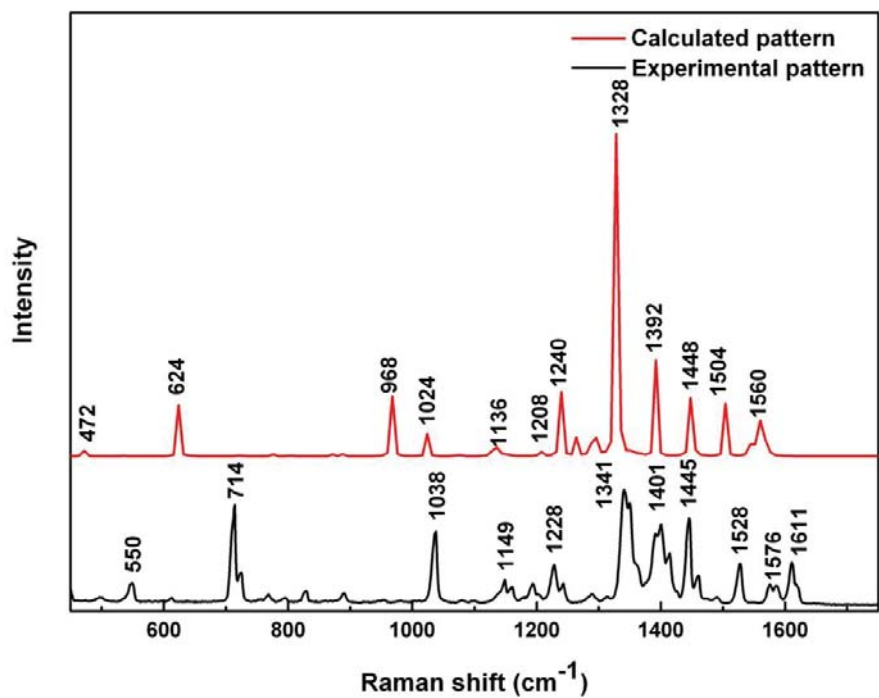


**Figure 5.14** Experimental and calculated Raman spectra of 1,10-phenanthroline. Experimental spectrum was recorded in solid state with 633 nm excitation. Intensity is measured in arbitrary units.

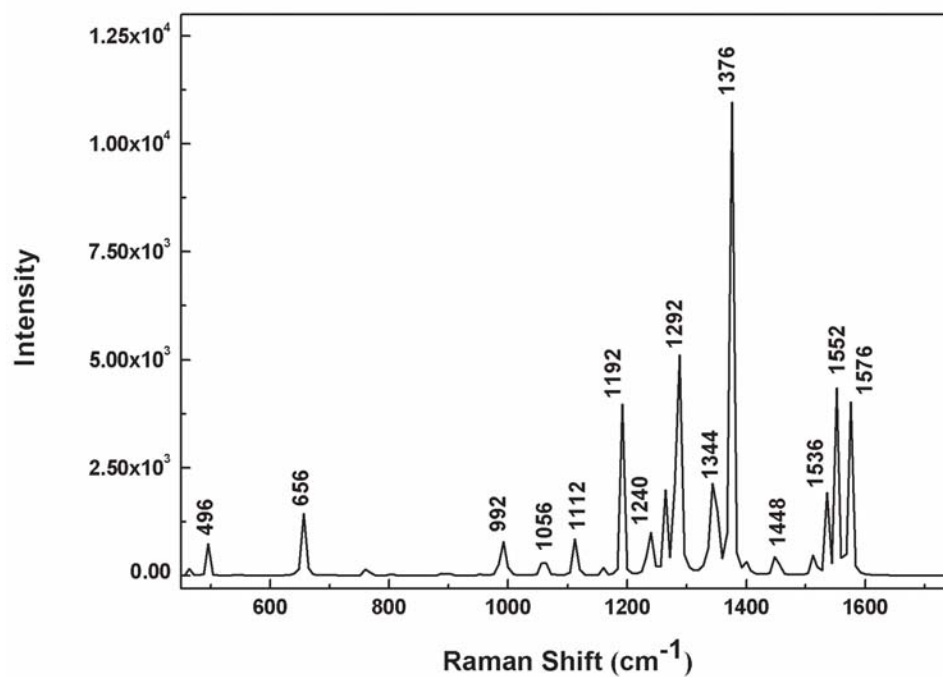


**Figure 5.15** Theoretical spectrum of phenanthroline calculated using Gaussian09 and figure generated using GaussView 5.<sup>197</sup> Intensity is measured in arbitrary units.

The Raman spectrum of MoO<sub>3</sub>-phen can be divided into two spectral regions. It is possible to identify four distinct bands in the first region that spans 450–1000 cm<sup>-1</sup> (Fig. 5.16). The first significant peak at 662 cm<sup>-1</sup>, and two strong peaks at 754 and 815 cm<sup>-1</sup> are identified as stretching vibrations of bridging oxygens in the Mo–O–Mo entity.<sup>130</sup> However, positions of these modes are significantly shifted for MoO<sub>3</sub>-phen when compared to MoO<sub>3</sub>-bpy, perhaps due to anomalies in the bond angles for these two compounds i.e. 96.37° for MoO<sub>3</sub>-phen and 99.59° for MoO<sub>3</sub>-bpy. Generally, in molybdenum oxide systems, the terminal oxo groups Mo=O are characterized by narrow Raman bands between 900–1000 cm<sup>-1</sup>.<sup>130,198</sup> Accordingly, the two Raman bands that appear at 915 cm<sup>-1</sup> and 991 cm<sup>-1</sup> in the Raman spectra of MoO<sub>3</sub>-phen are assigned to stretching vibrations of terminal oxygens Mo=O. However, Raman spectra of MoO<sub>3</sub>-bpy systems display a single well-behaved band at 917 cm<sup>-1</sup> suggesting that the molybdenum oxide octahedra are more distorted in MoO<sub>3</sub>-phen as compared to the former. Raman spectral region from 1000–1650 contains phen related modes which appear at similar positions in both WO<sub>3</sub>-phen and MoO<sub>3</sub>-phen. However, these modes are quite weak in intensity for MoO<sub>3</sub>-phen, perhaps, because of the dark colour of the specimen. Since X-ray structural studies confirm the coordinated layered structure for MoO<sub>3</sub>-phen, therefore, reduced intensity of these modes should not be considered as presence of uncoordinated ligands in the sample.

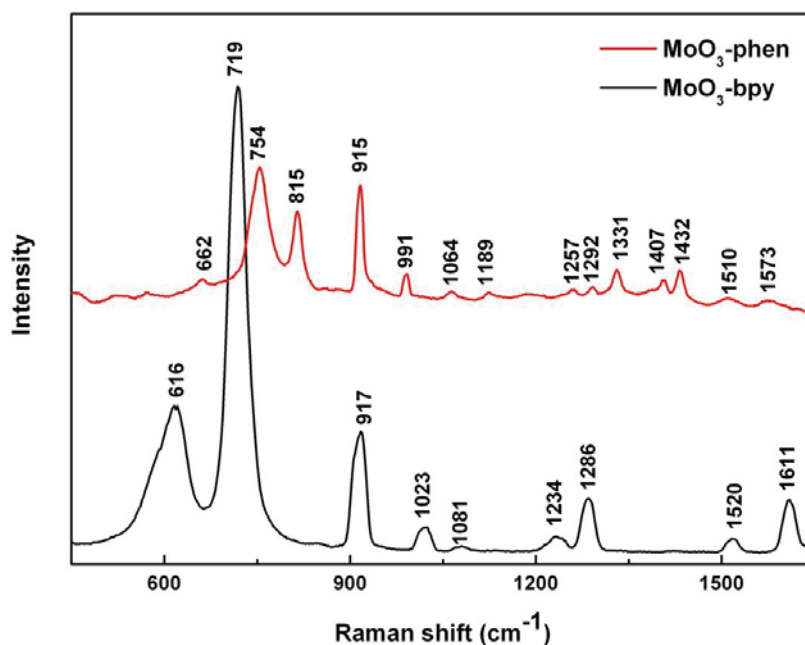


**Figure 5.16** Raman spectra of MoO<sub>3</sub>-phen and MoO<sub>3</sub>-bpy. Intensity is measured in arbitrary units.

The Raman spectra of  $\text{CuMoO}_4\text{-phen}$  display well-defined bands between 450–1650  $\text{cm}^{-1}$  (Fig.5.17). The strongest of these appears at 929  $\text{cm}^{-1}$  which is identified as stretching vibration of terminal oxo groups. Owing to the similar Mo=O bond distances in  $\text{CuMoO}_4$ ,  $\text{CuMoO}_4\text{-bpy}$  and  $\text{CuMoO}_4\text{-phen}$ , the position of this Raman band stays the same in all three compounds. Stretching vibrations of bridging oxo groups in  $\text{CuMoO}_4\text{-phen}$  result in four peaks that appear at 655  $\text{cm}^{-1}$ , 745  $\text{cm}^{-1}$ , 774  $\text{cm}^{-1}$  and 844  $\text{cm}^{-1}$ . Since there are two different types of coordination environments for molybdenum species in  $\text{CuMoO}_4\text{-phen}$ , therefore, the peaks at 655 and 844  $\text{cm}^{-1}$  are assigned to the symmetric stretch of (Mo–O–Mo) type bridging oxygens while those at 745  $\text{cm}^{-1}$  and 774  $\text{cm}^{-1}$ , which were absent in single-metal hybrids, correspond to (O–Mo–O) stretching vibrations. It can be noted that the position of these modes shift slightly for different bimetallic compounds reflecting the changes in the bond angles for bridging oxo groups and coordination preferences of metal-oxides. The Raman peaks from 1000–1650  $\text{cm}^{-1}$  correspond to stretching and bending vibrations of aromatic rings in phen and appear at positions similar to those discussed above.

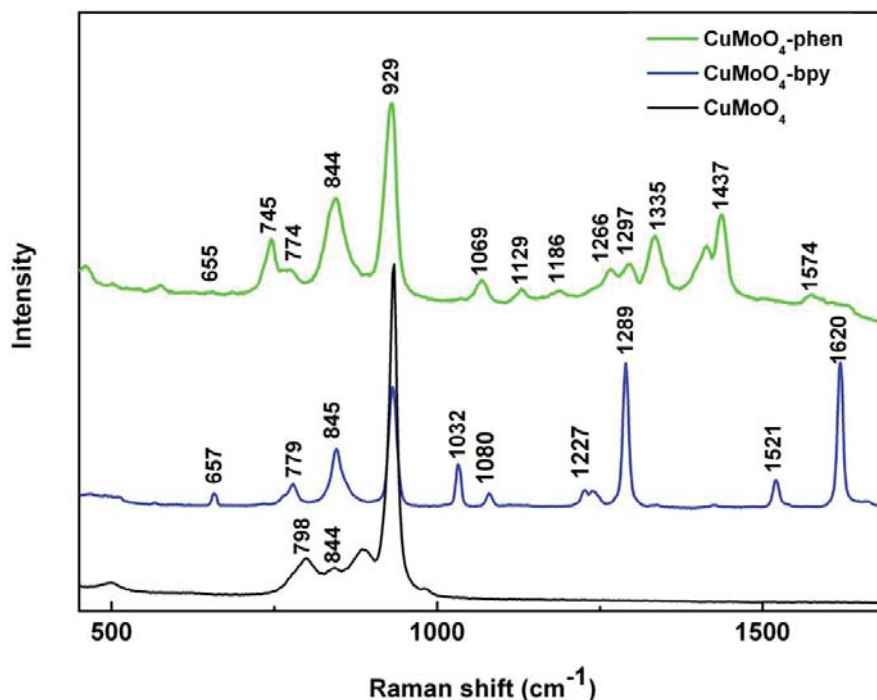


**Figure 5.17** A comparison of Raman spectra obtained from  $\text{CuMoO}_4$ ,  $\text{CuMoO}_4\text{-bpy}$  and  $\text{CuMoO}_4\text{-phen}$ . Despite the different nature of ligands, the position of 929  $\text{cm}^{-1}$  remains unchanged in all three compounds which reflects the strong influence of terminal oxo groups. Intensity is measured in arbitrary units.

The above results can be summarized as follows: (1) The metal-oxide stretching vibrations appear between 450–1000  $\text{cm}^{-1}$  while ligand bands appear between 1000–1650  $\text{cm}^{-1}$  (2) The terminal M=O stretching vibrations appear at similar wavenumber irrespective of the choice of ligands. (3) Change in bond angles for bridging oxo groups leads to shifts in Raman peaks. (4) The correlation between structural and spectroscopic data can be used to analyze the nature of metal-ligand interaction in single and bimetallic layered organic-inorganic hybrids.

## 5.6 Magnetic Measurements

Layered organic-inorganic hybrid materials display interesting magnetic properties and provide opportunities to develop 2D magnetically condensed systems.<sup>79,188,191</sup> Previous studies have shown that subtle changes in various reaction parameters such as the oxidation states of metal-atoms, orientation and geometry of organic ligands, and incorporation of secondary-metal atoms within the inorganic-oxide layer can help achieve near-perfect two-dimensional magnetic systems.<sup>79,191,193</sup>

$\text{WO}_3$ -phen and  $\text{MoO}_3$ -phen are diamagnetic because both  $\text{W}^{6+}$  and  $\text{Mo}^{6+}$  have no unpaired electrons i.e.  $S = 0$ . This is reflected by the temperature-dependent volume susceptibility measurements presented in Fig. 5.18 where the temperature-independent Pauli-like susceptibility does suggest that individual crystals are metallic. Fig. 5.18 shows that there is a magnetic transition for both compounds around 50 K. However, owing to the paired spins the appearance of this transition is highly unexpected in these materials. This was confirmed later by measuring these samples at high applied fields where no such transition was detected. Moreover, high-temperature magnetic susceptibility data of these compounds does not fit to Curie-Weiss law which further validates the diamagnetic nature of these compounds. The upturn at low temperatures could arise from small contamination of free spins forming a Curie behaviour that is negligible in all except at lowest temperatures. In contrast to  $\text{WO}_3$ -phen and  $\text{MoO}_3$ -phen,  $\text{CuMoO}_4$ -phen demonstrates strong antiferromagnetic behaviour which can be attributed to the presence of  $\text{Cu}^{2+}$  ions that reside in the  $\text{CuMoO}_4$  layers. As previously described, the structure of  $\text{CuMoO}_4$ -phen contains bimetallic oxide layers composed of discrete tetramer units of edge-sharing copper oxide ( $\text{CuO}_5\text{N}$ ) octahedra interconnected by corner-shared molybdenum oxide ( $\text{MoO}_4$ ) tetrahedra.

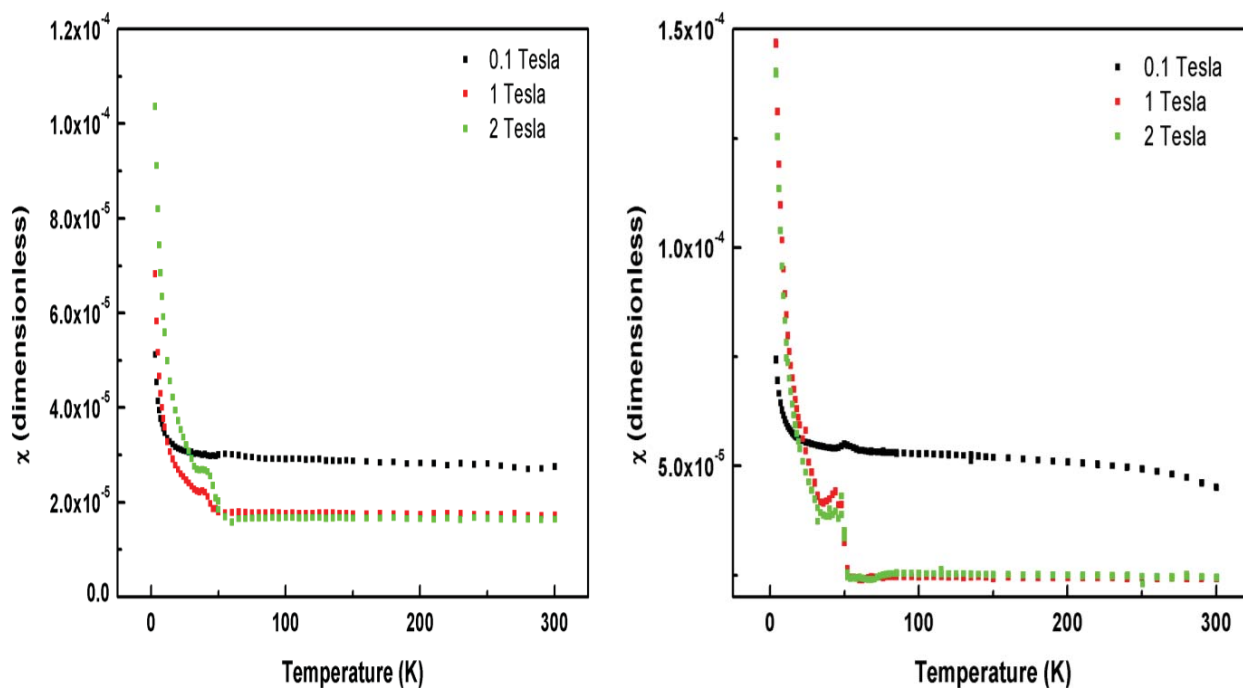


**Figure 5.18** Temperature-dependent volume susceptibility measurements recorded at different applied fields for  $\text{WO}_3\text{-phen}$  (left) and  $\text{MoO}_3\text{-phen}$  (right).

The outer Cu–Cu distances of 3.324–3.255 Å are much shorter than inter-tetramer Cu–Cu separations of 4.927–5.551 Å. Therefore, the magnetic susceptibility of  $\text{CuMoO}_4\text{-phen}$  can be approximated by a linear tetramer model.<sup>191</sup> Fig.5.19 shows the temperature-dependent susceptibility measurements of  $\text{CuMoO}_4\text{-phen}$  recorded at different applied magnetic fields. It can be noted that a broad maximum appears at 40 K which becomes significant with the increase of applied field. The appearance of this band can be attributed to strong antiferromagnetic ordering of  $\text{Cu}^{2+}$  ions in the bimetallic inorganic oxide layer. The high-temperature region of susceptibility data was fitted to Curie – Weiss Law

$$\chi = \frac{C}{T - \Theta}$$

where  $T$  is the temperature,  $C$  the Curie constant and  $\Theta$  the Weiss constant. Results show that data collected at higher applied fields (1 and 2 Tesla) satisfies the above relationship with  $\Theta = -10$  K the negative value of which suggest antiferromagnetic interactions of  $\text{Cu}^{2+}$  ions (Fig. 5.20). The strong antiferromagnetic ordering can further be confirmed by  $\chi T$  vs  $T$  plot which shows a gradual decrease in the  $\chi T$  product with decreasing temperature followed by a sudden drop at low temperatures (Fig. 5.21).

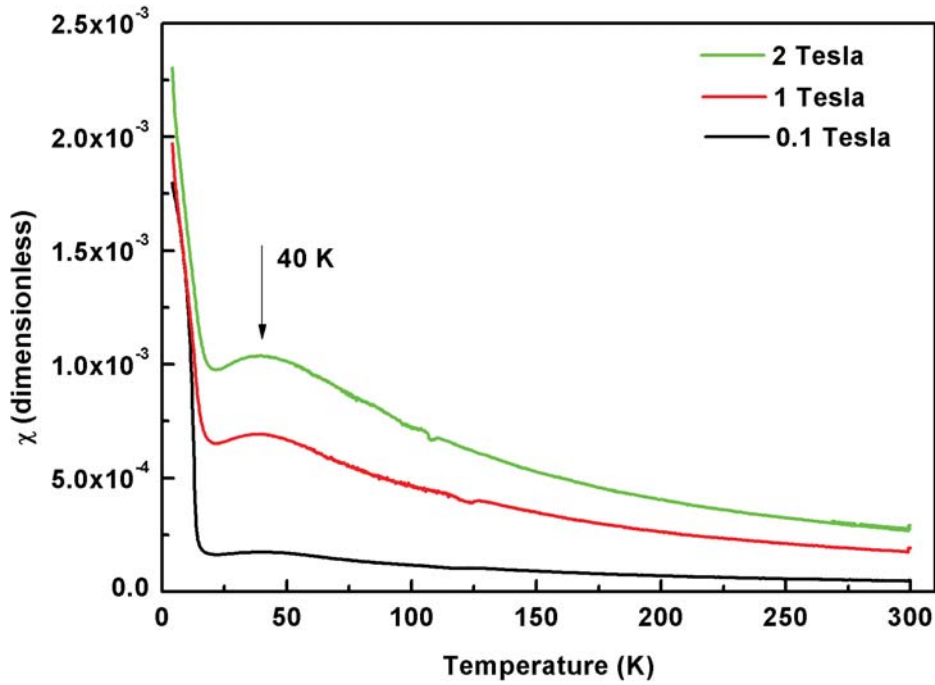


**Figure 5.19** Volume magnetic susceptibility of CuMoO<sub>4</sub>-phen measured at different applied fields.

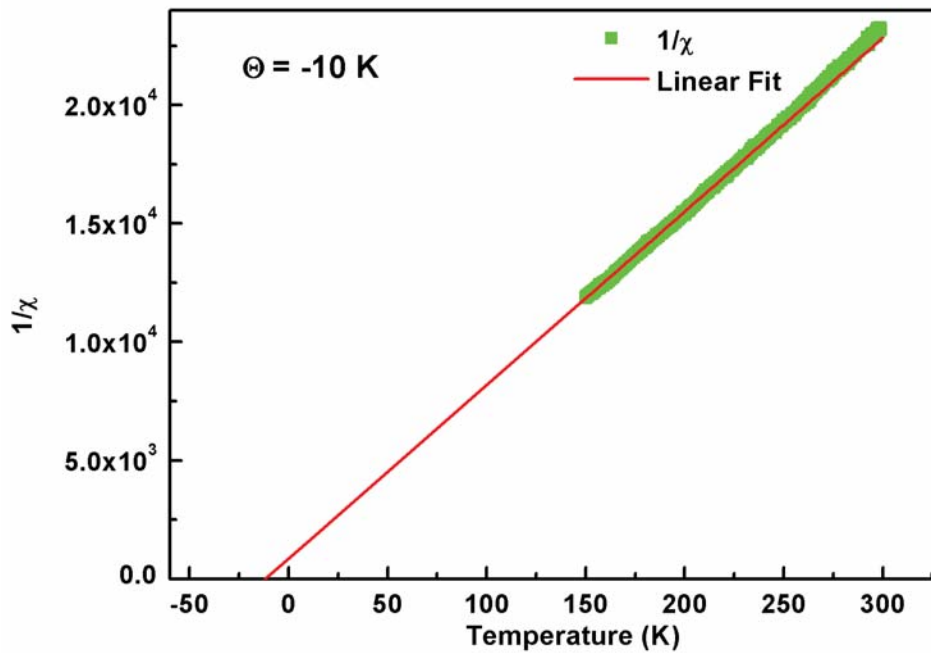


**Figure 5.20** Curie-Weiss Fitting to high-temperature susceptibility data of CuMoO<sub>4</sub>-phen.

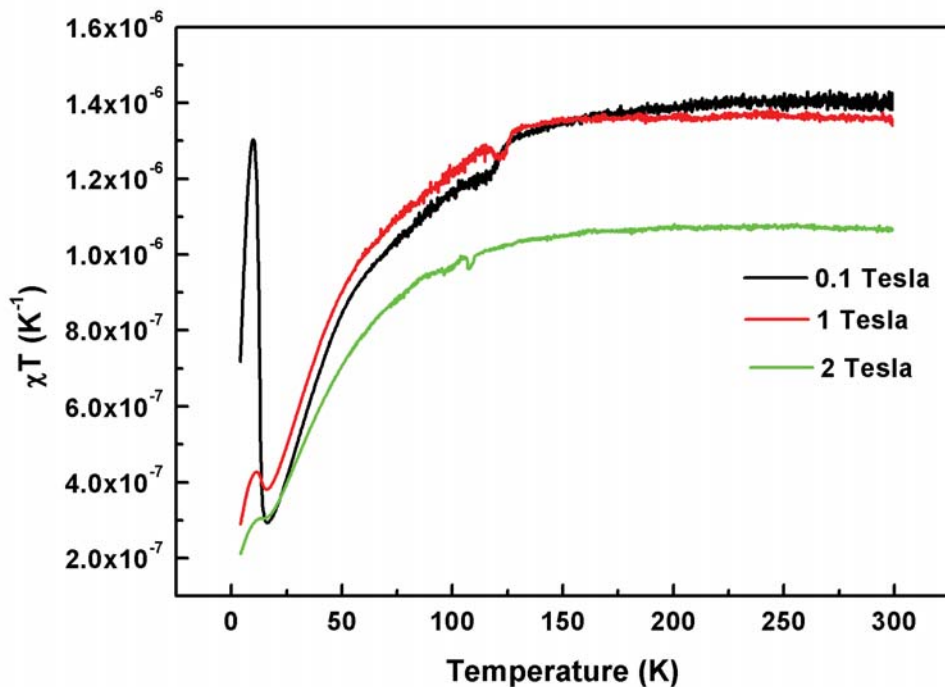


**Figure 5.21** Temperature-dependent  $\chi T$  plots for  $\text{CuMoO}_4\text{-phen}$  recorded at different applied fields.

## 5.7 Summary

For the first time, 3,8-phenanthrolines has been employed as bridging ligands to develop a system of novel layered organic-inorganic hybrid materials. The resulting materials exhibit two and three dimensional covalently bonded hybrid frameworks constructed from single and bimetallic oxide layers interlinked by organic ligands. Raman measurements correlate to the structural data and illustrate that how small changes in crystal structure can have significant effects on vibrational characteristics of the hybrid network. Insertion of  $\text{Cu}^{2+}$  ions within the inorganic layers induces strongly antiferromagnetic behaviour in the otherwise diamagnetic materials. The synthesis of  $\text{WO}_3\text{-phen}$ ,  $\text{MoO}_3\text{-phen}$  and  $\text{CuMoO}_4\text{-phen}$ ,  $\text{Cu}_3\text{Cr}_2\text{O}_{10}\text{-phen}$  open up possibilities for developing new materials by introducing different magnetic ions within the inorganic layers and searching for improved magnetic properties and even superconductivity in these types of hybrid materials.

## Chapter 6

### Summary and Future Directions

#### 6.1 Summary

A detailed study regarding the synthesis, characterization and doping, primarily by ion-implantation, of layered hybrid organic-inorganic materials has been carried out. For this purpose three main research areas were targeted: exploiting the self-assembly of simple reaction precursors to achieve layered structures, doping these materials in search of improved properties and performing a detailed characterization of these materials by means of physical and chemical techniques.

Firstly, single crystals of  $\text{WO}_3\text{-bpy}$  were prepared by hydrothermal synthesis. Single-crystal XRD demonstrated that structure of  $\text{WO}_3\text{-bpy}$  consists of atomic layers of corner-shared  $\text{WO}_5\text{N}$  octahedra bound by columns of bipyridyls linking the axial nitrogen atom. A close inspection of crystallographic data, by considering factors such as crystallographically imposed disorder, revealed that the bridging organic ligands are aligned alternately in  $[110]$  and  $[\bar{1}\bar{1}0]$  so as to define small cages, not the channels as reported previously.<sup>71,90</sup> In an attempt to intercalate alkali-metal atoms in these cages, selected single crystals were implanted with  $\text{Na}^+$  ions. Significant electron density, as determined by X-ray crystallography, confirmed the bulk intercalation of  $\text{Na}^+$  ions and prompted further studies. To determine the impact of  $\text{Na}^+$  intercalation on chemical and physical properties, thick films were coated on ITO substrate by combining  $\text{WO}_3\text{-bpy}$  with a conducting organic polymer. These films were implanted with  $\text{Na}^+$  ions and characterized by powder XRD, Raman and magnetic measurements before and after ion-implantation. Powder XRD and Raman spectra remained unchanged for implanted and unimplanted samples, possibly because of the presence of an organic binder and the shallow penetration depth of the intercalated species. Magnetic susceptibility measurements on polymer-bound thick films revealed a diamagnetic transition around 40 K but the result was not reproducible. Further measurements on implanted and un-implanted thick film samples did not provide any conclusive evidence of intercalation. Therefore, a precise understanding of the role of intercalated species in the

hybrid network required a successful fabrication of thin epitaxial films (or surface bound coatings without the use of organic binder). While several attempts to prepare epitaxial films proved unsuccessful, a polycrystalline surface-bound coating of  $\text{WO}_3$ -bpy was deposited on an ITO-coated glass substrate. To extend the scope of ion-implantation beyond  $\text{Na}^+$ , selected single crystals and surface-bound polycrystalline films were separately implanted with  $\text{Ca}^{2+}$  and  $\text{K}^+$  ions. Single crystal XRD confirmed the presence of intercalated species within the cage structure, while various other techniques were used to determine their presence in thick films. XPS analysis revealed a great deal of modification in the stoichiometry and composition of surface chemical states. Specifically, reduced tungsten species and additional residual electron density, absent in the original samples, were found in implanted samples. New phonon modes appear in the Raman spectra of implanted samples possibly because of local broken symmetry, reduced tungsten species and interaction of implanted cations with the host material. A significant increase in electrical conductivity upon ion-implantation further strengthened the assumption of charge carrier injection into the conduction band of the 2D metal oxide layer.<sup>91</sup>

Since magnetic susceptibility measurements of implanted and unimplanted thick films did not provide conclusive evidence of intercalation and the successful fabrication of thin films was not achieved, remaining challenges are to synthesize thin epitaxial films and large area single crystals for magnetic measurements. In order to further explore the structural diversity offered by transition-metal oxide layered hybrid networks, phen was selected as a bridging ligand. At first,  $\text{WO}_3$ -phen and  $\text{MoO}_3$ -phen were prepared using hydrothermal conditions very similar to those used for synthesis of their bpy counterparts. The resulting crystal structures of  $\text{WO}_3$ -phen and  $\text{MoO}_3$ -phen were found to be closely isomorphous where infinite layers of octahedral tungsten (or molybdenum) oxide are bridged by phen ligands through nitrogen atoms. Despite the similarities in the unit cell of bpy and phen based structures, the alignment of bridging ligands is distinctly different. A staggered herring-bone alignment of phen hybrids results in very small sized cages between apical oxygens thus limiting the scope of ion-implantation. Therefore, in-situ doping was attempted by introducing  $\text{Cu}^{2+}$  ions in the inorganic-metal oxide layers. The reactions were unsuccessful for  $\text{WO}_3$ -phen, however, introduction of  $\text{Cu}^{2+}$  in the inorganic layers of  $\text{MoO}_3$ -phen resulted in the formation of a novel bimetallic hybrid material  $\text{CuMoO}_4$ -phen. The crystal structure of this compound consists of bimetallic layers of edge-sharing copper oxide ( $\text{CuO}_5\text{N}$ ) octahedra corner-sharing with molybdenum oxide tetrahedra. These inorganic oxide layers are

interconnected by phen rings through Cu–N coordination bonds to form 3D hybrid frameworks. Replacing molybdenum with chromium in the bimetallic layers of  $\text{CuMoO}_4$ -phen generated another novel structure *i.e.*  $\text{Cu}_3\text{Cr}_2\text{O}_{10}$ -phen. The crystal structure of  $\text{Cu}_3\text{Cr}_2\text{O}_{10}$ -phen consists of bimetallic layers of edge-shared copper Cu(III) oxide octahedra and square-planar Cu(II) oxide corner-sharing with tetrahedral Cr(VI) oxides. Phen ligands link the adjacent inorganic layers through Cu–N coordination bonds to generate the overall network. All the phen based compounds except  $\text{Cu}_3\text{Cr}_2\text{O}_{10}$ -phen (owing to phase impurities) were further characterized by Raman spectroscopy and magnetic measurements. Raman measurements provided a deeper insight into the structural changes induced by changing organic and inorganic species within hybrid frameworks. It was found that, irrespective of the ligand choice, be it bpy or phen, the terminal M=O (M = W or Mo) vibrational modes appear at similar positions. However, significant changes in bond-lengths and bond-angles induced by replacing bpy with phen in these materials give rise to shifts in corresponding vibrational modes. Furthermore, introducing additional metal atoms in the inorganic-layers of  $\text{MoO}_3$ -phen significantly changes the position of terminal oxo and bridging oxo vibrational modes. Owing to the paired spins in  $\text{WO}_3$ -phen and  $\text{MoO}_3$ -phen, magnetic susceptibility measurements demonstrate a diamagnetic behaviour for these materials. However, a strong-antiferromagnetic transition was observed at low temperature in  $\text{CuMoO}_4$ -phen. While we failed to observe superconductivity in these systems it would seem that this goal is still realizable especially in view of the demonstration of corner-shared square-planar  $\text{CuO}_2$  which form the structural basis of cuprate superconductors. This requires finding ways of increasing the in-plane oxygen content per Cu atom to move from edge-shared CuO structures to corner-shared.

The materials described above represent a model system that promise excellent structural, electronic and magnetic features arising from self-assembly of organic and inorganic precursors. It is possible to exploit the self-assembly by controlling the size of organic-linkers, number and size of metal atoms in the inorganic-oxide layer and concentration of dopant species. The work described in this thesis provides only a glimpse into such a fascinating system and further experiments should be done to develop a full understanding of the underlying physics and to realize the applications these materials have to offer.

## 6.2 Future prospects

The results obtained from this study lead to several interesting prospects for future research.

Basically, two kind of ligands (bpy and phen) having similar chain length and similar position of terminal group, have been deployed successfully as organic linkers for the formation of layered hybrid frameworks. Synthesis of these hybrids with a similar, but non-linear ligand 1,2-bispyridylethylene (bpe), resulted in the formation of uncoordinated structures where bpe was not bonded to inorganic metal oxide molecules. Variations in reaction conditions, such as pH, change in molar ratio, heating/cooling duration were attempted but layered hybrids could not be obtained. Now since the position of the donor group (i.e. N) is essentially the same for these ligands (bpy, phen and bpe), the only difference is linearity. Therefore, as long as linearity is preserved, ligands with more benzene rings could be used as organic linkers in layered organic-inorganic frameworks. For example, instead of bpy, incorporating 1,4-di(pyridin-4-yl)benzene and 4,4'-di(pyridin-4-yl)biphenyl ligands in the hybrid frameworks will produce novel layered structures.<sup>199,200</sup> These compounds could offer enlarged cages between apical oxygens that can be used for implantation of larger metallic species than those used for WO<sub>3</sub>-bpy. Intercalation of small organic molecules such as 1,2-diaminohexane can also be a possibility by using electrochemical doping.

Since an exhaustive research has already been done on bpy based bimetallic hybrids involving molybdenum oxides, during this study synthesis of tungsten oxide based bimetallic hybrids was attempted.<sup>69</sup> A large number of reaction permutations were attempted but unfortunately synthesis of W-oxide-based layered bimetallic hybrids could not be achieved. This can be attributed to rigidity, relativistic effects and high bond-enthalpies of tungsten oxide systems.<sup>201</sup> Using salts of tungsten oxides such as WCl<sub>2</sub>O<sub>2</sub> instead of WO<sub>3</sub> or Na<sub>2</sub>WO<sub>4</sub>·2H<sub>2</sub>O as a starting material may help forming the hybrid network. This is definitely one of the proposed tasks.

Successful synthesis of phen hybrids opens up an entire new field for the synthesis of pillared hybrid materials. Numerous layered structures involving inorganic layers of transition-metal oxides can be achieved by replacing bpy ligands with phen. A detailed characterization of the resulting materials could provide a better understanding of structure-property relationship in these materials.

While thick, polycrystalline films of  $\text{WO}_3$ -bpy were coated successfully on ITO substrate without using an organic-binder, precise magnetic and electrical measurements, however, require the fabrication of homogenous thin epitaxial films.<sup>202</sup> Several attempts to fabricate such films using sol-gel deposition methods proved unfruitful. In the past vacuum deposition techniques such as atomic layer deposition (ALD), chemical vapour deposition (CVD), metal-oxide CVD or molecular beam epitaxy (MBE) have been used to prepare superlattice films of organic-inorganic hybrids.<sup>202-204</sup> Application of these techniques to fabricate thin films of the above studied hybrid organic-inorganic materials could be targeted in future.

## Appendix A

### Bond Valence Sum Calculations

Bond Valence Sum (BVS) were performed to determine the oxidation states of metal species in  $\text{Cu}_3\text{Cr}_2\text{O}_{10}$ -phen hybrid materials. BVS can be determined by using following equation

$$V_{cu} = \sum_i \exp\left(\frac{r_o - r_i}{B}\right) \quad (1)$$

Where  $r_i$  represents the Cu–O bond lengths. B has a fixed value of 0.37 and  $r_o$  has standard values as calculated in reference (204)<sup>205</sup>

For Cu – O bond lengths

$r_o = 1.679$  when Cu is close to divalent and

$r_o = 1.73$  when Cu is close to trivalent

Therefore, we have two forms of (1)

$$V_{1cu} = \sum_i \exp\left(\frac{1.679 - r_i}{0.37}\right) \quad (2)$$

And

$$V_{2cu} = \sum_i \exp\left(\frac{1.73 - r_i}{0.37}\right) \quad (3)$$

For Cu–N bond lengths,  $r_o$  values are not calculated in reference (204). However, a comparison of  $r_o$  for X–O and X–N bonds for other compounds reveals that  $r_o$  is about 0.1 higher for X–N.

Therefore, for Cu–N bond lengths

$r_o = 1.779$  when Cu is close to divalent and

$r_o = 1.83$  when Cu is close to trivalent

Cu(2)–O bond distances are given in Table A1

**Table A1:** Selected Cu(2)–O bond distances. Mathematical transformations used to generate symmetrically equivalent atoms:  $g = 1-x,-y,-z$

Bonds	Distances (Å)
Cu2–O1	1.93(2)
Cu2–O2	1.94(2)
Cu2–O1_g	1.93(2)
Cu2–O2_g	1.94(2)

Inserting the above bond distances in (2) and (3), we get

$$V_{1cu} = 0.5074 + 0.4939 + 0.5074 + 0.4939 = 2.002$$

$$V_{2cu} = 0.5824 + 0.5669 + 0.5824 + 0.5664 = 2.298$$

Now, since

$$V_{cu} = \frac{3V_{1cu} - 2V_{2cu}}{V_{1cu} + 1 - V_{2cu}}$$

$$V_{cu} = 2.002$$

So Cu(2) is divalent.

Turning towards Cu(1), Cu(1)–O and Cu(1)–N distances are given below

**Table A2:** Selected Cu(1)–O bond distances. Mathematical transformations used to generate symmetrically equivalent atoms: a = -1+x,y,z; b = -1+x,1+y,-1+z; e = -x,-y,-z.

Bonds	Distances (Å)
Cu1-O1	1.98(2)
Cu1-O2	1.97(2)
Cu1-N1	1.91(2)
Cu1-O5_a	1.95(2)
Cu1-O3_b	2.46(2)
Cu1-O1_e	2.32(3)

Inserting these distances in (2) and (3), we get

$$V_{1cu} = 0.4433 + 0.4554 + 0.7018 + 0.4807 + 0.1211 + 0.1767 = 2.3791$$

$$V_{2cu} = 0.5088 + 0.5228 + 0.8055 + 0.5517 + 0.1390 + 2.2030 = 2.7308$$

Now since

$$V_{cu} = \frac{3V_{1cu} - 2V_{2cu}}{V_{1cu} + 1 - V_{2cu}}$$

$$V_{cu} = 2.5872$$

So it is likely that Cu(1) is trivalent.

The Cr-O bond distances are as follow

**Table A3:** Selected Cr(3)-O bond distances

Bonds	Distance (Å)
Cr3-O2	1.76(2)
Cr3-O3	1.64(2)
Cr3-O4	1.60(2)
Cr3-O5	1.66(2)

The value of  $r_o$  is 1.794 Å. Inserting the values  $r_o$  and bond distances in (2), we get

$$V_{cr} = 1.096 + 1.51621 + 1.6893 + 1.4364 = 5.7374$$

So as expected Cr is hexavalent.

## Appendix B

### Unsuccessful Synthesis

Despite the successful synthesis of above described materials several attempts to prepare following layered hybrid materials remain unsuccessful.

#### **WO<sub>3</sub>-bpe**

It was aimed that replacing bpy with bpe in WO<sub>3</sub>-bpy structure would produce layered hybrid materials with larger cages, potentially, to accommodate larger metal ions or even small organic molecules. However, several attempts to achieve these compounds resulted in the formation of uncoordinated structures, mostly, consisting of decatungstate clusters and free standing organic ligands without any bonding to inorganic clusters. Various changes in reaction conditions were tried but no layered structures were obtained.

#### **MWO<sub>4</sub>-X (where M = V, Cr, Mn, Cu, Mo and X = bpy or phen)**

Several attempts to prepare tungsten oxide based bimetallic layered hybrids proved unsuccessful. Large numbers of reaction permutations were tried but no layered material was obtained. Details of the unsuccessful reactions can be found in table B1.

**Table B1** Details of unsuccessful synthesis.

<b>Target Compound</b>	<b>Stoichiometry</b>	<b>Heating *T/*1D</b>	<b>Cooling *T/*1D</b>	<b>Observation</b>
<b>Bispyridylethylene Tungstate WO<sub>3</sub>(bpe)<sub>0.5</sub></b>	Na <sub>2</sub> WO <sub>4</sub> .2H <sub>2</sub> O:Bpe:H <sub>2</sub> O 0.285:0.110:15 (g, mL) HCl = 0.08 mL	160/120	20/5	Orange crystals. Uncoordinated structure. Asymmetric unit cell: W <sub>10</sub> O <sub>32</sub> (H <sub>2</sub> bpy) <sub>2</sub>
Bispyridylethylene Tungstate WO <sub>3</sub> (bpe) <sub>0.5</sub>	Na <sub>2</sub> WO <sub>4</sub> .2H <sub>2</sub> O:Bpe:H <sub>2</sub> O 0.285:0.110:15 (g, mL) HCl = 0.08 mL	160/120	Slow cooling at approximate rate of -10 °C per hour	White powder. No crystals.
Bispyridylethylene Tungstate WO <sub>3</sub> (bpe) <sub>0.5</sub>	Na <sub>2</sub> WO <sub>4</sub> .2H <sub>2</sub> O:Bpe:H <sub>2</sub> O 0.285:0.110:15 (g, mL) HCl = 0.32 mL	160/120	Slow cooling at approximate rate of -10 °C per hour	Yellow and green product. No crystals.
Bispyridylethylene Tungstate WO <sub>3</sub> (bpe) <sub>0.5</sub>	Na <sub>2</sub> WO <sub>4</sub> .2H <sub>2</sub> O:Bpe:H <sub>2</sub> O 0.285:0.110:15 (g, mL) HCl = 0.02 mL	160/120	Slow cooling at approximate rate of -10 °C per hour	Yellow crystalline product. Structure could not be obtained due to poor data.
Bispyridylethylene Tungstate WO <sub>3</sub> (bpe) <sub>0.5</sub>	Na <sub>2</sub> WO <sub>4</sub> .2H <sub>2</sub> O:Bpe:H <sub>2</sub> O 0.143:0.055:7.5 (g, mL)	160/124	Slow cooling at approximate rate of -10 °C per hour	Few bits of sticky material. No crystals.

Bispyridylethylene Tungstate  $\text{WO}_3(\text{bpe})_{0.5}$	$\text{Na}_2\text{WO}_4 \cdot 2\text{H}_2\text{O}:\text{Bpe}:\text{H}_2\text{O}$ 0.143:0.055:7.5 (g, mL) pH = 9 adjusted by adding few drops of NaOH solution	160/124	Slow cooling at approximate rate of -10 $^\circ\text{C}$ per hour	Transparent solution. No solid product.
<b>Bipyridyl Copper Tungstate</b>  $\text{CuWO}_4\text{-(bpy)}_{0.5}$	$\text{Na}_2\text{WO}_4 \cdot 2\text{H}_2\text{O}:\text{Cu}(\text{NO}_3)_2 \cdot 3$ $\text{H}_2\text{O}:\text{Bpy}:\text{H}_2\text{O}$  0.06:0.05:0.06:15 (g, mL)	160/124	Slow cooling at approximate rate of -10 $^\circ\text{C}$ per hour	Green crystalline product. Structure could not be obtained due to poor data.
Bipyridyl Copper Tungstate  $\text{CuWO}_4\text{-(bpy)}_{0.5}$	$\text{Na}_2\text{WO}_4 \cdot 2\text{H}_2\text{O}:\text{Cu}_2\text{O}:$ $\text{Bpy}:\text{H}_2\text{O}$  0.06:0.06:0.05:15 (g, mL)	170/120	Slow cooling at approximate rate of -10 $^\circ\text{C}$ per hour	Black coloured product. No crystals.
Bipyridyl Copper Tungstate  $\text{CuWO}_4\text{-(bpy)}_{0.5}$	$\text{Na}_2\text{WO}_4 \cdot 2\text{H}_2\text{O}:\text{Cu}_2\text{O}:$ $\text{Bpy}:\text{H}_2\text{O}$  0.06:0.06:0.05:15 (g, mL)	170/72	Slow cooling at approximate rate of -10 $^\circ\text{C}$ per hour	Red coloured product. No crystals.
Bipyridyl Copper Tungstate  $\text{CuWO}_4\text{-(bpy)}_{0.5}$	$\text{Na}_2\text{WO}_4 \cdot 2\text{H}_2\text{O}:\text{Cu}_2\text{O}:$ $\text{Bpy}:\text{H}_2\text{O}$  0.06:0.06:0.05:15 (g, mL) HCl = 0.1 mL	170/72	Slow cooling at approximate rate of -10 $^\circ\text{C}$ per hour	Yellow crystals. Asymmetric unit cell: $(\text{CuCl})_2\text{bpy}$
Bipyridyl Copper Tungstate  $\text{CuWO}_4\text{-(bpy)}_{0.5}$	$\text{Na}_2\text{WO}_4 \cdot 2\text{H}_2\text{O}:\text{Cu}_2\text{O}:$ $\text{Bpy}:\text{H}_2\text{O}$  0.12:0.06:0.05:15 (g, mL) HCl = 0.1 mL	170/72	Slow cooling at approximate rate of -10 $^\circ\text{C}$ per hour	Yellow crystals. Asymmetric unit cell: $(\text{CuCl})_5(\text{bpy})_{2.5}$

Bipyridyl Copper Tungstate  CuWO <sub>4</sub> -(bpy) <sub>0.5</sub>	Na <sub>2</sub> WO <sub>4</sub> .2H <sub>2</sub> O:Cu <sub>2</sub> O: Bpy:H <sub>2</sub> O  0.233:0.087:0.05:15 (g, mL)	170/72	Slow cooling at approximate rate of -10 °C per hour	Green powder. No crystals.
Bipyridyl Copper Tungstate  CuWO <sub>4</sub> -(bpy) <sub>0.5</sub>	Na <sub>2</sub> WO <sub>4</sub> .2H <sub>2</sub> O:CuSO <sub>4</sub> : Bpy:H <sub>2</sub> O  0.06:0.06:0.05:15 (g, mL)	170/72	Slow cooling at approximate rate of -10 °C per hour	Blue crystals. Asymmetric unit cell: CuSO <sub>4</sub> (bpy) <sub>2</sub>
Bipyridyl Copper Tungstate  CuWO <sub>4</sub> -(bpy) <sub>0.5</sub>	Na <sub>2</sub> WO <sub>4</sub> .2H <sub>2</sub> O:CuSO <sub>4</sub> : Bpy:H <sub>2</sub> O  0.09:0.06:0.05:15 (g, mL)	170/72	Slow cooling at approximate rate of -10 °C per hour	Green product. No crystals.
Bipyridyl Copper Tungstate  CuWO <sub>4</sub> -(bpy) <sub>0.5</sub>	Na <sub>2</sub> WO <sub>4</sub> .2H <sub>2</sub> O:CuSO <sub>4</sub> : Bpy:H <sub>2</sub> O  0.06:0.06:0.05:15 (g, mL)	220/49	24 hours at room temperature.	Yellow product. No crystals.
Bipyridyl Copper Tungstate  CuWO <sub>4</sub> -(bpy) <sub>0.5</sub>	Na <sub>2</sub> WO <sub>4</sub> .2H <sub>2</sub> O:CuSO <sub>4</sub> : Bpy:H <sub>2</sub> O  0.06:0.06:0.05:15 (g, ml)	220/72	Slow cooling at approximate rate of -10 °C per hour	Yellow product. No crystals.
Bipyridyl Copper Tungstate  CuWO <sub>4</sub> -(bpy) <sub>0.5</sub>	Na <sub>2</sub> WO <sub>4</sub> .2H <sub>2</sub> O:CuSO <sub>4</sub> : Bpy:H <sub>2</sub> O  0.06:0.06:0.05:15 (g, mL)	220/120	Slow cooling at approximate rate of -10 °C per hour	Yellow product. No crystals.

Bipyridyl Copper Tungstate  CuWO <sub>4</sub> -(bpy) <sub>0.5</sub>	Na <sub>2</sub> WO <sub>4</sub> .2H <sub>2</sub> O:CuCl <sub>2</sub> . 2H <sub>2</sub> O: Bpy:H <sub>2</sub> O  0.06:0.06:0.05:15 (g, mL)	220/120	Slow cooling at approximate rate of -10 °C per hour	Orange coloured crystalline product. Asymmetric unit cell: (CuClbpy) <sub>2</sub>
Bipyridyl Copper Tungstate  CuWO <sub>4</sub> -(bpy) <sub>0.5</sub>	Na <sub>2</sub> WO <sub>4</sub> .2H <sub>2</sub> O:CuCl <sub>2</sub> . 2H <sub>2</sub> O: Bpy:H <sub>2</sub> O  0.06:0.06:0.05:15 (g, mL)	220/96	Slow cooling at approximate rate of -10 °C per hour	Orange coloured crystalline product. Asymmetric unit cell: (CuClbpy) <sub>2</sub>
Bipyridyl Copper Tungstate  CuWO <sub>4</sub> -(bpy) <sub>0.5</sub>	Na <sub>2</sub> WO <sub>4</sub> .2H <sub>2</sub> O:CuCl <sub>2</sub> . 2H <sub>2</sub> O: Bpy:H <sub>2</sub> O  0.286:0.121:0.091:15 (g, mL)	220/96	Slow cooling at approximate rate of -10 °C per hour	Green powder. No crystals.
Bipyridyl Copper Tungstate  CuWO <sub>4</sub> -(bpy) <sub>0.5</sub>	Na <sub>2</sub> WO <sub>4</sub> .2H <sub>2</sub> O:CuCl <sub>2</sub> . 2H <sub>2</sub> O: Bpy:H <sub>2</sub> O  0.137:0.070:0.06:15 (g, mL)	220/72	Slow cooling at approximate rate of -10 °C per hour	Green powder. No crystals.
Bipyridyl Copper Tungstate  CuWO <sub>4</sub> -(bpy) <sub>0.5</sub>	H <sub>2</sub> WO <sub>4</sub> :Cu <sub>2</sub> O: Bpy:H <sub>2</sub> O  0.12:0.06:0.05:15 (g, ml)	170/72	Slow cooling at approximate rate of -10 °C per hour	Multicoloured (cyan and red) product. No crystals.

Bipyridyl Copper Tungstate  CuWO <sub>4</sub> -(bpy) <sub>0.5</sub>	H <sub>2</sub> WO <sub>4</sub> :Cu <sub>2</sub> O: Bpy:H <sub>2</sub> O  0.06:0.06:0.05:15 (g, mL) HCl = 0.1 mL	170/72	Slow cooling at approximate rate of -10 °C per hour	Brown crystalline product. Assymmetric unit cell: CuCl(bpy) <sub>0.5</sub>
Bipyridyl Copper Tungstate  CuWO <sub>4</sub> -(bpy) <sub>0.5</sub>	WO <sub>3</sub> :Cu <sub>2</sub> O: Bpy:H <sub>2</sub> O  0.06:0.06:0.05:15 (g, mL)	170/72	Slow cooling at approximate rate of -10 °C per hour	Multicoloured product. No crystals.
Bipyridyl Copper Tungstate  CuWO <sub>4</sub> -(bpy) <sub>0.5</sub>	WO <sub>3</sub> :Cu <sub>2</sub> O: Bpy:H <sub>2</sub> O  0.06:0.06:0.05:15 (g, mL)	220/72	Slow cooling at approximate rate of -10 °C per hour	Multicoloured product. No crystals.
Bipyridyl Copper Tungstate  CuWO <sub>4</sub> -(bpy) <sub>0.5</sub>	WO <sub>3</sub> :Cu <sub>2</sub> O: Bpy:H <sub>2</sub> O  0.06:0.06:0.05:15 (g, mL)	220/120	Slow cooling at approximate rate of -10 °C per hour	Multicoloured product. No crystals.
Bipyridyl Copper Tungstate  CuWO <sub>4</sub> -(bpy) <sub>0.5</sub>	WO <sub>3</sub> :Cu <sub>2</sub> O: Bpy:H <sub>2</sub> O  0.06:0.06:0.05:15 (g, mL) Nitric acid = 0.07 ml	220/120	Slow cooling at approximate rate of -10 °C per hour	Blue solution. No solid product.

Bipyridyl Copper Tungstate  CuWO <sub>4</sub> -(bpy) <sub>0.5</sub>	WO <sub>3</sub> :Cu <sub>2</sub> O: Bpy:H <sub>2</sub> O  0.96:0.06:0.05:15 (g, mL)	170/72	Slow cooling at approximate rate of -10 °C per hour	Yellow crystalline product. Despite of no chloride in the reactants. Cu, however, picked Cl from impurities. Asymmetric unit cell: CuCl(bpy) <sub>2</sub>
Bipyridyl Copper Tungstate  CuWO <sub>4</sub> -(bpy) <sub>0.5</sub>	WO <sub>3</sub> :Cu <sub>2</sub> O: Bpy:H <sub>2</sub> O  0.96:0.06:0.05:15 (g, mL)	220/240	Slow cooling at approximate rate of -10 °C per hour	Multicoloured product. Crystals not good enough to pursue a full X- ray scan.
Bipyridyl Copper Tungstate  CuWO <sub>4</sub> -(bpy) <sub>0.5</sub>	WO <sub>3</sub> :Cu <sub>2</sub> O: Bpy:H <sub>2</sub> O  0.06:0.06:0.05:15 (g, mL) NaOH = 0.5 mL	170/72	Slow cooling at approximate rate of -10 °C per hour	Multicoloured product. No crystals.
Bipyridyl Copper Tungstate  CuWO <sub>4</sub> -(bpy) <sub>0.5</sub>	WO <sub>3</sub> :Cu <sub>2</sub> O: Bpy:H <sub>2</sub> O  0.06:0.06:0.05:15 (g, mL) NaOH = 1 mL	170/72	Slow cooling at approximate rate of -10 °C per hour	Black coloured product. Crystals not good enough to pursue a full X- ray scan.
Bipyridyl Copper Tungstate  CuWO <sub>4</sub> -(bpy) <sub>0.5</sub>	WO <sub>3</sub> :Cu <sub>2</sub> O: Bpy:H <sub>2</sub> O  0.06:0.06:0.05:15 (g, mL) NaOH = 1 mL	220/72	Slow cooling at approximate rate of -10 °C per hour	Black coloured product. No crystals

Bipyridyl Copper Tungstate  CuWO <sub>4</sub> -(bpy) <sub>0.5</sub>	WO <sub>3</sub> :Cu <sub>2</sub> O: Bpy:H <sub>2</sub> O  0.96:0.06:0.05:15 (g, mL) NaOH = 1 mL	220/240	Slow cooling at approximate rate of -10 °C per hour	Multicoloured product. Crystals not good enough to pursue a full X- ray scan.
Bipyridyl Copper Tungstate  CuWO <sub>4</sub> -(bpy) <sub>0.5</sub>	WO <sub>3</sub> :Cu <sub>2</sub> O: Bpy:H <sub>2</sub> O  0.06:0.06:0.05:15 (g, mL) NaOH = 2 mL	170/72	Slow cooling at approximate rate of -10 °C per hour	Black coloured product. Crystals not good enough to pursue a full X- ray scan.
Bipyridyl Copper Tungstate  CuWO <sub>4</sub> -(bpy) <sub>0.5</sub>	WO <sub>3</sub> :Cu <sub>2</sub> O: Bpy:H <sub>2</sub> O  0.096:0.033:0.05:15 (g, mL)	170/120	Slow cooling at approximate rate of -10 °C per hour	Black coloured product. No crystals.
Bipyridyl Copper Tungstate  CuWO <sub>4</sub> -(bpy) <sub>0.5</sub>	WO <sub>3</sub> :CuSO <sub>4</sub> : Bpy:H <sub>2</sub> O  0.06:0.06:0.05:15 (g, mL)	170/72	Slow cooling at approximate rate of -10 °C per hour	Cyan powder product. No crystals.
Bipyridyl Copper Tungstate  CuWO <sub>4</sub> -(bpy) <sub>0.5</sub>	WO <sub>3</sub> :CuSO <sub>4</sub> : Bpy:H <sub>2</sub> O  0.06:0.06:0.05:15 (g, mL)	170/96	Slow cooling at approximate rate of -10 °C per hour	Cyan powder product. No crystals.
Bipyridyl Copper Tungstate  CuWO <sub>4</sub> -(bpy) <sub>0.5</sub>	WO <sub>3</sub> :CuSO <sub>4</sub> : Bpy:H <sub>2</sub> O  0.06:0.06:0.05:15 (g, mL)	170/96	Slow cooling at approximate rate of -10 °C per hour	Cyan powder product. No crystals.

<b>Bipyridyl Vanadium Tungstate</b>  <b>VWO<sub>4</sub>-(bpy)<sub>0.5</sub></b>	Na <sub>2</sub> WO <sub>4</sub> .2H <sub>2</sub> O:V <sub>2</sub> O <sub>5</sub> : Bpy:H <sub>2</sub> O  0.06:0.05:0.02:15 (g, mL)	170/77	Slow cooling at approximate rate of -10 °C per hour	Bright yellow transparent solution. No solid product.
Bipyridyl Vanadium Tungstate  VWO <sub>4</sub> -(bpy) <sub>0.5</sub>	Na <sub>2</sub> WO <sub>4</sub> .2H <sub>2</sub> O:V <sub>2</sub> O <sub>5</sub> : Bpy:H <sub>2</sub> O  0.06:0.05:0.02:15 (g, mL)	240/77	Slow cooling at approximate rate of -10 °C per hour	Bright yellow transparent solution. No solid product.
Bipyridyl Vanadium Tungstate  VWO <sub>4</sub> -(bpy) <sub>0.5</sub>	Na <sub>2</sub> WO <sub>4</sub> .2H <sub>2</sub> O:V <sub>2</sub> O <sub>5</sub> : Bpy:H <sub>2</sub> O  0.06:0.05:0.02:15(g, mL) HCl = 0.1 mL	240/77	Slow cooling at approximate rate of -10 °C per hour	Black powder. No crystals.
Bipyridyl Vanadium Tungstate  VWO <sub>4</sub> -(bpy) <sub>0.5</sub>	Na <sub>2</sub> WO <sub>4</sub> .2H <sub>2</sub> O:V <sub>2</sub> O <sub>5</sub> : Bpy:H <sub>2</sub> O  0.06:0.05:0.02:15 (g, mL) HCl = 0.1 mL	170/77	Slow cooling at approximate rate of -10 °C per hour	Light green powder. No crystals.
Bipyridyl Vanadium Tungstate  VWO <sub>4</sub> -(bpy) <sub>0.5</sub>	WO <sub>3</sub> :V <sub>2</sub> O <sub>5</sub> : Bpy:H <sub>2</sub> O  0.096:0.076:0.05:15 (g, mL) HCl = 0.1 mL	175/72	Slow cooling at approximate rate of -10 °C per hour	Multicoloured product. No crystals.
<b>Bipyridyl Chromium Tungstate</b>  CrWO <sub>4</sub> -(bpy) <sub>0.5</sub>	WO <sub>3</sub> :CrO <sub>3</sub> : Bpy:H <sub>2</sub> O  0.06:0.06:0.05:15 (g, mL)	170/72	Slow cooling at approximate rate of -10 °C per hour	Orange crystals. Asymmetric unit cell: Cr <sub>2</sub> O <sub>6</sub> -bpy

Bipyridyl Chromium Tungstate  $\text{CrWO}_4\text{-(bpy)}_{0.5}$	$\text{WO}_3\text{:CrO}_3\text{:Bpy:H}_2\text{O}$  0.12:0.06:0.05:15 (g, mL)	170/72	Slow cooling at approximate rate of -10 $^\circ\text{C}$ per hour	Yellow crystalline product. Crystals not good enough for full data collection.
Bipyridyl Chromium Tungstate  $\text{CrWO}_4\text{-(bpy)}_{0.5}$	$\text{WO}_3\text{:CrO}_3\text{:Bpy:H}_2\text{O}$  0.096:0.042:0.05:15 (g, mL)	170/72	Slow cooling at approximate rate of -10 $^\circ\text{C}$ per hour	Yellow crystalline product. Crystals not good enough for full data collection.
<b>Bipyridyl</b> <b>Molybdenum</b> <b>Tungstate</b>  <b><math>\text{MoWO}_4\text{-(bpy)}_{0.5}</math></b>	$\text{Na}_2\text{WO}_4\cdot 2\text{H}_2\text{O}:\text{MoO}_3\text{:}$ $\text{Bpy:H}_2\text{O}$  0.06:0.06:0.05:15 (g, mL)	170/72	Slow cooling at approximate rate of -10 $^\circ\text{C}$ per hour	Yellow coloured crystalline product. Asymmetric unit cell: $\text{W}_{12}\text{O}_{36}(\text{bpy})_5$
Bipyridyl Molybdenum Tungstate  $\text{MoWO}_4\text{-(bpy)}_{0.5}$	$\text{Na}_2\text{WO}_4\cdot 2\text{H}_2\text{O}:\text{MoO}_3\text{:}$ $\text{Bpy:H}_2\text{O}$  0.06:0.06:0.05:15 (g, mL)	170/72	Slow cooling at approximate rate of -10 $^\circ\text{C}$ per hour	Yellow coloured crystalline product. Asymmetric unit cell: $\text{W}_{12}\text{O}_{36}(\text{bpy})_5$
<b>Bipyridyl</b> <b>Manganese</b> <b>Tungstate</b>  $\text{MnWO}_4\text{-(bpy)}_{0.5}$	$\text{Na}_2\text{WO}_4\cdot 2\text{H}_2\text{O}:\text{MnCl}_2\cdot$ $4\text{H}_2\text{O}:\text{Bpy:H}_2\text{O}$  0.137:0.083:0.05:15 (g, mL)	170/72	Slow cooling at approximate rate of -10 $^\circ\text{C}$ per hour	Multicoloured product. No crystals.

Bipyridyl Manganese Tungstate  MnWO <sub>4</sub> -(bpy) <sub>0.5</sub>	Na <sub>2</sub> WO <sub>4</sub> .2H <sub>2</sub> O:MnCl <sub>2</sub> . 4H <sub>2</sub> O: Bpy:H <sub>2</sub> O  0.137:0.083:0.05:15 (g, mL)	170/121	Slow cooling at approximate rate of -10 °C per hour	Light orange product. No crystals.
Bipyridyl Manganese Tungstate  MnWO <sub>4</sub> -(bpy) <sub>0.5</sub>	Na <sub>2</sub> WO <sub>4</sub> .2H <sub>2</sub> O:MnCl <sub>2</sub> . 4H <sub>2</sub> O: Bpy:H <sub>2</sub> O  0.137:0.083:0.05:15 (g, mL)	170/240	Slow cooling at approximate rate of -10 °C per hour	Light orange product. No crystals.
Bipyridyl Manganese Tungstate  MnWO <sub>4</sub> -(bpy) <sub>0.5</sub>	WO <sub>3</sub> :MnO <sub>2</sub> : Bpy:H <sub>2</sub> O  0.096:0.036:0.05:15 (g, ml)	170/72	Slow cooling at approximate rate of -10 °C per hour	Multicoloured product. No crystals.
Bipyridyl Manganese Tungstate  MnWO <sub>4</sub> -(bpy) <sub>0.5</sub>	WO <sub>3</sub> :MnO <sub>2</sub> : Bpy:H <sub>2</sub> O  0.096:0.036:0.05:15 (g, mL)	170/121	Slow cooling at approximate rate of -10 °C per hour	Green powder. No crystals.
Bipyridyl Manganese Tungstate  MnWO <sub>4</sub> -(bpy) <sub>0.5</sub>	WO <sub>3</sub> :MnO <sub>2</sub> : Bpy:H <sub>2</sub> O  0.096:0.036:0.05:15 (g, mL) HCl = 0.1 mL	170/121	Slow cooling at approximate rate of -10 °C per hour	Green powder. No crystals.
Bipyridyl Manganese Tungstate  MnWO <sub>4</sub> -(bpy) <sub>0.5</sub>	WO <sub>3</sub> :MnO <sub>2</sub> : Bpy:H <sub>2</sub> O  0.06:0.06:0.06:15 (g, mL)	170/120	Slow cooling at approximate rate of -10 °C per hour	Black crystalline product. Crystals not good enough for full data collection.

Bipyridyl Manganese Tungstate  MnWO <sub>4</sub> -(bpy) <sub>0.5</sub>	WO <sub>3</sub> :MnO <sub>2</sub> : Bpy:H <sub>2</sub> O  0.06:0.06:0.06:15 (g, mL) NaOH = 1 mL	170/120	Slow cooling at approximate rate of -10 °C per hour	Black crystalline product. Crystals not good enough for full data collection.
Bipyridyl Manganese Tungstate  MnWO <sub>4</sub> -(bpy) <sub>0.5</sub>	WO <sub>3</sub> :MnO <sub>2</sub> : Bpy:H <sub>2</sub> O  0.06:0.06:0.06:15 (g, mL) NaOH = 2 mL	170/120	Slow cooling at approximate rate of -10 °C per hour	Black crystalline product. Crystals not good enough for full data collection.
Bipyridyl Manganese Tungstate  MnWO <sub>4</sub> -(bpy) <sub>0.5</sub>	WO <sub>3</sub> :MnO <sub>2</sub> : Bpy:H <sub>2</sub> O  0.096:0.072:0.05:15 (g, mL) NaOH = 1 mL	220/240	Slow cooling at approximate rate of -10 °C per hour	Black crystalline product. Crystals not good enough for full data collection.

\*T = Heating temperature measured in degree celsius

\*<sup>1</sup>D = Duration for cooling measured in hours

## Appendix C

### X-ray Crystal Structure Data

A CD attached with this thesis contains X-ray structure files (*cif* and *checkcif*) of the compounds reported in this study.

## References

- (1) Tokura, Y. *Physics Today* **2003**, 56, 50.
- (2) Cox, P. *Transition metal oxides: An Introduction to their electronic structure and properties*; Clarendon Press: Oxford, 1992.
- (3) O'Brien, M. C. M.; Chancey, C. *Am. J. Phys.* **1993**, 61, 688.
- (4) Mott, N.; Peierls, R. *Proceedings of the Physical Society* **1937**, 49, 72.
- (5) Tokura, Y.; Nagaosa, N. *Science* **2000**, 288, 462.
- (6) Ramirez, A. *J. Phys.: Condens. Matter* **1997**, 9, 8171.
- (7) Onnes, H. K. *Commun. Phys. Lab. Univ. Leiden* **1911**, 12, 1.
- (8) Geim, A.; Dubonos, S.; Lok, J.; Henini, M.; Maan, J. *Nature* **1998**, 396, 144.
- (9) Landau, L. D.; Ter Haar, D. *Collected papers of LD Landau*; Pergamon Press Oxford, 1965.
- (10) Bardeen, J.; Cooper, L.; Schrieffer, J. *Phys. Rev.* **1957**, 108, 1175.
- (11) Cooper, L. *Phys. Rev.* **1956**, 104, 1189.
- (12) Bednorz, J. G.; Muller, K. A. *Z. Phys. B. Con. Mat.* **1986**, 64, 189.
- (13) Choy, J.; Kwon, S.; Park, G. *Science (New York, NY)* **1998**, 280, 1589.
- (14) Orenstein, J.; Millis, A. *Science* **2000**, 288, 468.
- (15) Wheatley, J.; Hsu, T.; Anderson, P. *Nature* **1988**, 333, 121.
- (16) Tallon, J. L.; Bernhard, C.; Niedermayer, C. *Supercond. Sci. Technol.* **1997**, 10, A38.
- (17) Choy, J.; Kwon, S.; Hwang, S.; Kim, Y.; Jang, E. *Int. J. Inorg. Mater.* **2001**, 3, 253.
- (18) Schilling, A.; Cantoni, M.; Guo, J.; Ott, H. *Nature* **1993**, 363, 56.
- (19) Chu, C.; Gao, L.; Chen, F.; Huang, Z.; Meng, R.; Xue, Y. **1993**.
- (20) Rotter, M.; Tegel, M.; Johrendt, D. *Phys. Rev. Lett.* **2008**, 101, 107006.
- (21) Aliev, A. E. *Supercond. Sci. Technol.* **2008**, 21, 115022.
- (22) Kwon, S.-J.; Choy, J.-H. *Inorg. Chem.* **2003**, 42, 8134.
- (23) KICKELBICK, G. *Hybrid materials: synthesis, characterization, and applications*; Wiley-VCH, Weinheim, 2007.
- (24) Hubert-pfalzgraf, L. G. *New J. Chem.* **1987**, 11, 663.
- (25) Judeinstein, P.; Sanchez, C. *J. Mater. Chem.* **1996**, 6, 511.
- (26) Schubert, U.; Husing, N.; Lorenz, A. *Chem. Mater* **1995**, 7.
- (27) Folch, B.; Larionova, J.; Guari, Y.; Datas, L.; Guérin, C. *J. Mater. Chem.* **2006**, 16, 4435.
- (28) Sanchez, C.; Ribot, F. *New J. Chem.* **1994**, 18, 1007.
- (29) Golding, F. *The Manufacture of Boots and Shoes: Being a Modern Treatise of All the Processes of Making and Manufacturing Footgear*; Jackson Press, 2008.
- (30) Sanchez, C.; Julián, B.; Belleville, P.; Popall, M. *J. Mater. Chem.* **2005**, 15, 3559.
- (31) Sanchez, C.; Arribart, H.; Guille, M. *Nat Mater* **2005**, 4, 277.
- (32) Gomez-Romero, P. *Adv. Mater.* **2001**, 13, 163.
- (33) Gallegos, A. K. C. *Organic/Inorganic Hybrid Materials based on Conducting Organic Polymers as Electrodes for Energy Storage Devices*, Universitat Autònoma de Barcelona, 2003.
- (34) Gómez-Romero, P.; Sánchez, C. *Functional hybrid materials*; Wiley-Vch Verlag GmbH & Co. KGaA: Weinheim, 2004.
- (35) Sanchez, C.; Lebeau, B.; Chaput, F.; Boilot, J. P. *Adv. Mater.* **2003**, 15, 1969.

- (36) Coronado, E.; Day, P. *Chem. Rev.* **2004**, *104*, 5419.
- (37) Choy, J. *J. Phys. Chem. Solids* **2004**, *65*, 373.
- (38) Choy, J.; Hwang, S.; Park, N. *J. Am. Chem. Soc.* **1997**, *119*, 1624.
- (39) Yamanaka, S.; Hotehama, K.; Kawaji, H. *Nature* **1998**, *392*, 580.
- (40) Gamble, F.; DiSalvo, F.; Klemm, R.; Geballe, T. *Science* **1970**, *168*, 568.
- (41) Reisfeld, R. *Opt. Mater.* **2001**, *16*, 1.
- (42) Crano, J.; Guglielmetti, R. *Organic Photochromic and Thermochromic Compounds: Main Photochromic Families*; Plenum Publishing Corporation, 1999.
- (43) Schaudel, B.; Guermeur, C.; Sanchez, C.; Nakatani, K.; Delaire, J. *J. Mater. Chem.* **1997**, *7*, 61.
- (44) Avnir, D.; Levy, D.; Reisfeld, R. *J. Phys. Chem.* **1984**, *88*, 5956.
- (45) Rottman, C.; Grader, G.; De Hazan, Y.; Melchior, S.; Avnir, D. *J. Am. Chem. Soc.* **1999**, *121*, 8533.
- (46) Rottman, C.; Grader, G.; Avnir, D. *Chem. Mater* **2001**, *13*, 3631.
- (47) Schottner, G. *Chem. Mater* **2001**, *13*, 3422.
- (48) [www.sol-gel.com](http://www.sol-gel.com).
- (49) Tadanaga, K.; Kitamuro, K.; Matsuda, A.; Minami, T. *J. Sol-Gel Sci. Technol.* **2000**, *26*, 705.
- (50) Itou, T.; Matsuda, H. *Key Eng. Mater.* **1998**, *150*, 67.
- (51) Houbertz, R.; Domann, G.; Schulz, J.; Olsowski, B.; Fröhlich, L.; Kim, W. *Appl. Phys. Lett.* **2004**, *84*, 1105.
- (52) Popall, M.; Dabek, A.; Robertsson, M.; Valizadeh, S.; Hagel, O.; Buestrich, R.; Nagel, R.; Cergel, L.; Lambert, D.; Schaub, M. *Mol. Cryst. and Liq. Cryst.* **2000**, *354*, 123.
- (53) Robertson, M.; Gustafsson, G.; Hagel, O.; Popall, M. *IEEE PEP* **1997**, 203.
- (54) Ingham, B. *Low-Dimensional Physics of Organic-Inorganic Multilayers*, Victoria University of Wellington, 2005.
- (55) Cheetham, A.; Brinker, C.; Mecartney, M.; Sanchez, C. *Better ceramics through chemistry VI*, 1994.
- (56) Schmidt, H. In *Chemistry, Spectroscopy and Applications of Sol-Gel Glasses*; Reisfeld, R., Jorgensen, C. K., Eds.; Springer-Verlag: Berlin, 1991.
- (57) Shea, K.; Loy, D.; Webster, O. *J. Am. Chem. Soc.* **1992**, *114*, 6700.
- (58) Kissick, J.; Cowley, A.; Chippindale, A. *J. Solid State Chem.* **2002**, *167*, 17.
- (59) Fernandez, S.; Pizarro, J.; Mesa, J.; Lezama, L.; Arriortua, M.; Olazcuaga, R.; Rojo, T. *Inorg. Chem.* **2001**, *40*, 3476.
- (60) Sarkar, K.; Yokoi, T.; Tatsumi, T.; Bhaumik, A. *Microporous Mesoporous Mater.* **2008**, *110*, 405.
- (61) <http://homepage3.nifty.com/mnakayama/index-e.htm>.
- (62) Jacobson, A.; Johnson, J.; Lewandowski, J. *Inorg. Chem.* **1985**, *24*, 3727.
- (63) Kudo, M.; Ohkawa, H.; Sugimoto, W.; Kumada, N.; Liu, Z.; Terasaki, O.; Sugahara, Y. *Inorg. Chem.* **2003**, *42*, 4479.
- (64) Wells, A. *Structural Inorganic Chemistry*, v. 2; Moskow, 1987.
- (65) Wells, A. F. *Structural Inorganic Chemistry*, Clarendon; Oxford, 1984.
- (66) Ingham, B.; Hendy, S.; Chong, S.; Tallon, J. *Phys. Rev. B* **2005**, *72*, 75109.
- (67) Nanba, T.; Yasui, I. *J. Solid State Chem.* **1989**, *83*, 304.
- (68) Jones, F. H.; Rawlings, K.; Dixon, R. A.; Fishlock, T. W.; Egdell, R. G. *Surf. Sci.* **2000**, *460*, 277.
- (69) Hagrman, P. J.; Hagrman, D.; Zubieta, J. *Angew. Chem. Int. Ed.* **1999**, *38*, 2638.
- (70) Hagrman, P.; LaDuca Jr, R.; Koo, H.; Rarig Jr, R.; Haushalter, R.; Whangbo, M.; Zubieta, J. *Inorg. Chem* **2000**, *39*, 4311.

- (71) Yan, B.; Xu, Y.; Goh, N.; Chia, L. *Chem. Commun.* **2000**, 2000, 2169.
- (72) Twu, J.; Fang, T.; Hsu, C.; Yu, Y.; Wang, G.; Tang, C.; Chen, K.; Lii, K. *J. Mater. Chem.* **1998**, 8, 2181.
- (73) Islah-u-din; Chong, S. V.; Telfer, S. G.; Kennedy, J.; Jameson, G. B.; Waterland, M. R.; Tallon, J. L. pH Directed Synthesis of Tungsten and Molybdenum Oxide Based Organic-Inorganic Hybrid Materials, 2011.
- (74) Ingham, B.; Chong, S. V.; Tallon, J. L. *J. Phys. Chem. B* **2005**, 109, 4936.
- (75) Evans, H. T.; Weakley, T. J. R.; Jameson, G. B. *J. Chem. Soc., Dalton Trans.* **1996**, 2537.
- (76) Liu, C.; Luo, F.; Liu, N.; Cui, Y.; Wang, X.; Wang, E.; Chen, J. *Cryst. Growth Des.* **2006**, 6, 2658.
- (77) Fu, H.; Chen, W.; Wang, E.; Liu, J.; Chang, S. *Inorg. Chim. Acta* **2009**, 362, 1412.
- (78) Zhang, Y.; Zapf, P. J.; Meyer, L. M.; Haushalter, R. C.; Zubieta, J. *Inorg. Chem.* **1997**, 36, 2159.
- (79) Hagrman, D.; Zubeita, C.; Rose, D. J.; Zubieta, J.; Haushalter, R. C. *Angew. Chem. Int. Ed. Engl.* **1997**, 36, 873.
- (80) Hagrman, D.; Sangregorio, C.; O'Connell, C. J.; Zubieta, J. *Journal of the Chemical Society, Dalton Transactions* **1998**, 3707.
- (81) Hagrman, D.; Warren, C. J.; Haushalter, R. C.; Seip, C.; O'Connor, C. J.; Rarig, R. S.; Johnson, K. M.; LaDuca, R. L.; Zubieta, J. *Chem. Mater.* **1998**, 10, 3294.
- (82) Shanks, H. R. *Solid State Commun.* **1974**, 15, 753.
- (83) Reich, S.; Tsabba, Y. *Eur. Phys. J. B.* **1999**, 9, 1.
- (84) Chong, S. V.; Tallon, J. L. *J. Phys. Chem. Solids* **2010**, 71, 303.
- (85) Laudise, R. A. *50 Years Progress In Crystal Growth: A Reprint Collection* **2004**, 185.
- (86) Zheng, Z. Synthesis and modifications of metal oxide nanostructures and their applications, Queensland University of Technology, 2009.
- (87) Spezzia, G. *Accad. Sci. Torino Atti* **1905**, 40, 254.
- (88) Iwasaki, F.; Iwasaki, H. *J. Cryst. Growth* **2002**, 237, 820.
- (89) Frank, F.; Doremus, R.; Roberts, B.; Turnbull, D. *Wiley, New York* **1958**, 411.
- (90) Islah-u-din; Fox, M. R.; Martin, H.; Gainsford, G. J.; Kennedy, J.; Markwitz, A.; Telfer, S. G.; Jameson, G. B.; Tallon, J. L. *Chem. Commun.* **2010**, 46, 4261.
- (91) Islah-u-din; Chong, S. V.; Telfer, S. G.; Kennedy, J.; Jameson, G. B.; Waterland, M. R.; Tallon, J. L. *J. Phys. Chem. C* **2012**, 116, 3787.
- (92) Piticescu, R. M.; Piticescu, R.; Vasile, E. *submitted to Journal de Physique IV*.
- (93) Rao, T.; Karthikeyan, T. *Int. J. Adv. Manuf. Tech.* **1998**, 14, 153.
- (94) Townsend, P. *Contemp. Phys.* **1986**, 27, 241.
- (95) Kennedy, J. V.; Trompeter, W.; Markwitz, A. *Elemental analysis of ion implanted nanomaterials*; Institute of Geological & Nuclear Sciences, 2005.
- (96) Franssila, S. *Introduction to microfabrication*, 2nd ed.; Wiley Online Library, 2004.
- (97) <http://www.spirecorp.com/spire-biomedical/surface-treatment/technology-overview/ion-implantation.php>, 2010; Vol. 2010.
- (98) Lindhard, J.; Scharff, M.; Schiøtt, H. E. *Kgl. Danske Videnskab. Selskab. Mat. Fys. Medd.* **1963**, 33.
- (99) Ziegler, J. F.; Ziegler, M.; Biersack, J. *Nuclear Instruments and Methods in Physical Research Section B: Beam Interactions with Materials and Atoms*, 268, 1818.
- (100) Ziegler, J. *www.srim.org* **2003**.
- (101) Large, L. *Contemp. Phys.* **1969**, 10, 277.

- (102) Wegmann, L. *Nucl. Instrum. Methods* **1981**, 189, 1.
- (103) Rose, P. H. *Nucl. Instrum. Meth. B* **1985**, 6, 1.
- (104) Shannon, J. *Electron. Lett* **1969**, 5, 181.
- (105) Sze, S. *VLSI Technology, McGraw-Hill* **1983**, 372.
- (106) Donnelly, J.; Ferrante, G. *Solid-State Electronics* **1980**, 23, 1151.
- (107) Stephens, K. *Nucl. Instrum. Methods* **1983**, 209, 589.
- (108) Hofsass, H.; Ronning, C.; Muller, S.; Zhang, K.; Zutz, H. Formation of ferro-, para-, and superparamagnetic nanostructures by ion beam treatment of materials. In *Ion Beam Applications in Surface and Bulk Modification of Insulators*, 2008; pp 27.
- (109) Bharuth-Ram, K. Formation of magnetic nanoclusters and complexes by ion implantation of Fe into suitable insulators. In *Ion Beam Applications in Surface and Bulk Modification of Insulators*, 2008; pp 35.
- (110) Ekimov, E.; Sidorov, V.; Bauer, E.; Mel'Nik, N.; Curro, N.; Thompson, J.; Stishov, S. *Nature* **2004**, 428, 542.
- (111) Tan, J. C.; Cheetham, A. K. *Chem. Soc. Rev.* **2011**, 40, 1059.
- (112) Takano, Y.; Takenouchi, T.; Ishii, S.; Ueda, S.; Okutsu, T.; Sakaguchi, I.; Umezawa, H.; Kawarada, H.; Tachiki, M. *Diamond Relat. Mater.* **2007**, 16, 911.
- (113) Ren, Z. A.; Kato, J.; Muranaka, T.; Akimitsu, J.; Kriener, M.; Maeno, Y. *J. Phys. Soc. Jpn.* **2007**, 76.
- (114) Chong, S.; Tallon, J.; Fang, F.; Kennedy, J.; Kadowaki, K.; Williams, G. *Europhys. Lett.* **2011**, 94, 37009.
- (115) Stout, G. H.; Jensen, L. H. *John Wiley and Sons, Inc.(United States)*, **1989**, 453.
- (116) Phillips, F. C. *An introduction to crystallography*; Wiley, 1972.
- (117) Lipson, H. *The study of metals and alloys by X-ray powder diffraction methods*; University College Cardiff Press, 1984.
- (118) Paynter, R. W. *Techniques of biocompatibility testing* **1986**, 2, 49.
- (119) Innes, P. *Proceedings of the Royal Society of London. Series A* **1907**, 79, 442.
- (120) Robinson, H.; Rawlinson, W. *The London, Edinburgh, and Dublin Philosophical Magazine and Journal of Science* **1914**, 28, 277.
- (121) Moseley, H. G. J. *The London, Edinburgh, and Dublin Philosophical Magazine and Journal of Science* **1913**, 26, 1024.
- (122) Siegbahn, K.; Edvarson, K. *Nuclear Physics* **1956**, 1, 137.
- (123) Paynter, R. W. *XPS Theory* Varennes, Quebec, 2000.
- (124) Smith, E.; Dent, G.; Wiley, J. *Modern Raman spectroscopy: a practical approach*; J. Wiley Hoboken, NJ, 2005.
- (125) Raman, C. V.; Krishnan, K. *Nature* **1928**, 121, 501.
- (126) Long, D. A.; Long, D. *Raman spectroscopy*; McGraw-Hill New York, 1977; Vol. 206.
- (127) Colthup, N.; Daly, L.; Wiberley, S. **1990**.
- (128) Heller, E.; Sundberg, R.; Tannor, D. *The Journal of Physical Chemistry* **1982**, 86, 1822.
- (129) Iwaki, M.; Watanabe, H. *Nucl. Instrum. Meth. B* **1998**, 141, 206.
- (130) Seguin, L.; Figlarz, M.; Cavagnat, R.; Lassègues, J. C. *Spectrochim. Acta A* **1995**, 51, 1323.
- (131) Daniel, M.; Desbat, B. *J. Solid State Chem.* **1987**, 67, 235.
- (132) Zawada, K.; Bukowska, J. *J. Mol. Struct.* **2000**, 555, 425.
- (133) Fischer, D.; Pospiech, D.; Scheler, U.; Navarro, R.; Messori, M.; Fabbri, P. "Monitoring of the Sol-Gel Synthesis of Organic-inorganic Hybrids by FTIR Transmission, FTIR/ATR, NIR and Raman Spectroscopy", 2008.

- (134) Gnyba, M.; Keranen, M.; Kozanecki, M.; Bogdanowicz, R.; Kosmowski, B.; Wroczynski, P. *Opto-Electron Rev.* **2002**, 137.
- (135) Suetaka, W.; Yates, J. *Surface infrared and Raman spectroscopy: methods and applications*; Springer, 1995.
- (136) Moskovits, M.; Suh, J. *The Journal of Physical Chemistry* **1984**, 88, 5526.
- (137) Range, S. K. NASA, Available online: [\*http://einstein.stanford.edu/content/education/GP-BT-Guide4-2008.pdf\(PD\)\*](http://einstein.stanford.edu/content/education/GP-BT-Guide4-2008.pdf(PD)) **2004**, 6, 7.
- (138) Anderson, P.; Rowell, J. M. *Phys. Rev. Lett.* **1963**, 10, 230.
- (139) Jaklevic, R.; Lambe, J.; Silver, A.; Mercereau, J. *Phys. Rev. Lett.* **1964**, 12, 159.
- (140) Clarke, J.; Braginski, A. I. *The SQUID handbook*; Wiley Online Library, 2006; Vol. 1.
- (141) Clarke, J.; Goubau, W.; Ketchen, M. *J. Low Temp. Phys.* **1976**, 25, 99.
- (142) Yang, H.; Chen, J.; Wang, S.; Chen, C.; Jeng, J.; Chen, J.; Wu, C.; Liao, S.; Hornig, H. *Tamkang Journal of Science and Engineering* **2003**, 6, 9.
- (143) Kleiner, R.; Koelle, D.; Ludwig, F.; Clarke, J. *Proceedings of the IEEE* **2004**, 92, 1534.
- (144) McElfresh, M. *Quantum Design* **1994**, 11578.
- (145) Ingham, B. Organic-Inorganic Layered Hybrid Materials. In *Soft Condensed Matter: New Research* Dillon, K. I., Ed.; Nova Science: New York, 2007.
- (146) Zhai, Q. G.; Hu, M. C.; Li, S. N.; Jiang, Y. C. *Inorg. Chem. Commun.* **2008**, 11, 1147.
- (147) Figlarz, M. *Prog. Solid State Chem.* **1989**, 19, 1.
- (148) Biersack, J. P. *Nucl. Instrum. Meth. B* **1987**, 19-20, 32.
- (149) Zhong, Q.; Wessel, S. A.; Heinrich, B.; Colbow, K. *Solar Energ Mater* **1990**, 20, 289.
- (150) Macrae, C.; Edgington, P.; McCabe, P.; Pidcock, E.; Shields, G.; Taylor, R.; Towler, M.; Streek, J. *J. Appl. Crystallogr.* **2006**, 39, 453.
- (151) ViewerPro, D. S. Accelrys Inc: San Diego; CA, 2002.
- (152) Spek, A. *J. Appl. Crystallogr.* **2003**, 36, 7.
- (153) Cason, C. J. POV-RAY; Persistence of Vision Raytracer Pty Ltd: Victoria, 2003.
- (154) Moissette, A.; Batonneau, Y.; Bremard, C. *J. Am. Chem. Soc.* **2001**, 123, 12325.
- (155) Nonaka, K.; Takase, A.; Miyakawa, K. *J. Mater. Sci. Lett.* **1993**, 12, 274.
- (156) O'Connor, G. *Global NEST J.* **2009**, 11, 308.
- (157) Lu, T.; Cotton, T. M.; Birke, R. L.; Lombardi, J. R. *Langmuir* **1989**, 5, 406.
- (158) Topacli, A.; Akyüz, S. *Spectrochim. Acta A* **1995**, 51, 633.
- (159) Horsley, J.; Wachs, I.; Brown, J.; Via, G.; Hardcastle, F. *J. Phys. Chem-US* **1987**, 91, 4014.
- (160) Deb, S. *Appl. Opt.* **1969**, 8, 192.
- (161) Deb, S. K. *Sol. Energy Mater. Sol. Cells* **1992**, 25, 327.
- (162) Azens, A.; Kitenbergs, M.; Kanders, U. *Vacuum* **1995**, 46, 745.
- (163) Klein, J.; Yen, A. "Crystal phase effects in electrochromic WO<sub>3</sub>"; Solid State Ionics III, 1993, Boston, Massachusetts, USA
- (164) Ashrit, P. V.; Bader, G.; Truong, V.-V. *Thin Solid Films* **1998**, 320, 324.
- (165) Granqvist, C. G. *Sol. Energy Mater. Sol. Cells* **2000**, 60, 201.

- (166) Witham, H.; Chindaudom, P.; An, I.; Collins, R.; Messier, R.; Vedam, K. *J. Vac. Sci. Technol. A* **1993**, *11*, 1881.
- (167) Gottsche, J.; Hinsch, A.; Wittwer, V. *Sol. Energy Mater. Sol. Cells* **1993**, *31*, 415.
- (168) Kikuchi, E.; Iida, K.; Fujishima, A.; Itoh, K. *J. Electroanal. Chem.* **1993**, *351*, 105.
- (169) Chen, Z.; Yang, Y.; Qiu, J.; Yao, J. *Langmuir* **2000**, *16*, 722.
- (170) Moon, J.; Shin, J.; Kim, S.; Park, J. *Langmuir* **1996**, *12*, 4621.
- (171) Cronin, J. P.; Tarico, D. J.; Agrawal, A.; Zhang, R. L. *U.S. Patent 5277986 Jan. 11, 1994*.
- (172) Sungpanich, J.; Thongtem, T.; Thongtem, S. *Ceram. Int.* **2012**, *38*, 1051.
- (173) Azturk, O.; Turkan, U.; Eroglu, A. E. *Surf. Coat. Technol.* **2006**, *200*, 5687.
- (174) Siokou, A.; Leftheriotis, G.; Papaefthimiou, S.; Yianoulis, P. *Surf. Sci.* **2001**, *482*, 294.
- (175) Leftheriotis, G.; Papaefthimiou, S.; Yianoulis, P.; Siokou, A. *Thin Solid Films* **2001**, *384*, 298.
- (176) Leftheriotis, G.; Papaefthimiou, S.; Yianoulis, P.; Siokou, A.; Kefalas, D. *Appl. Surf. Sci.* **2003**, *218*, 276.
- (177) Gross, T.; Kahn, G.; Unger, W. E. S. *Surf. Interface Anal.* **2009**, *41*, 445.
- (178) McCafferty, E.; Wightman, J. *Surf. Interface Anal.* **1998**, *26*, 549.
- (179) Sarno, D. M.; Jiang, B.; Grosfeld, D.; Afriyie, J. O.; Matienzo, L. J.; Jones Jr, W. E. *Langmuir* **2000**, *16*, 6191.
- (180) Chernyshova, I.; Rao, K. H.; Vidyadhar, A.; Shchukarev, A. *Langmuir* **2000**, *16*, 8071.
- (181) Katrib, A.; Hemming, F.; Wehrer, P.; Hilaire, L.; Maire, G. *J. Electron Spectrosc.* **1995**, *76*, 195.
- (182) Mueller, D.; Shih, A.; Roman, E.; Madey, T.; Kurtz, R.; Stockbauer, R. *J. Vac. Sci. Technol. A* **1988**, *6*, 1067.
- (183) Reich, S.; Leitus, G.; Popovitz-Biro, R.; Goldbourt, A.; Vega, S. *J. Supercond. Nov. Magn.* **2009**, *22*, 343.
- (184) Chong, S.; Ingham, B.; Tallon, J. *Curr. Appl. Phys.* **2004**, *4*, 197.
- (185) Sanchez, C.; Belleville, P.; Popall, M.; Nicole, L. *Chem. Soc. Rev.*, *40*, 696.
- (186) Irfan; Ding, H.; Gao, Y.; Kim, D. Y.; Subbiah, J.; So, F. *Appl. Phys. Lett.* **2010**, *96*, 073304.
- (187) Borissevitch, A.; Yanovskaya, M.; Kessler, V.; Nikonorova, N. *J. Sol-Gel Sci. Technol.* **1998**, *12*, 111.
- (188) Ingham, B.; Chong, S.; Tallon, J. *Curr. Appl. Phys.* **2004**, *4*, 202.
- (189) Hirohama, T.; Kuranuki, Y.; Ebina, E.; Sugizaki, T.; Arii, H.; Chikira, M.; Tamil Selvi, P.; Palaniandavar, M. *J. Inorg. Biochem.* **2005**, *99*, 1205.
- (190) Accorsi, G.; Listorti, A.; Yoosaf, K.; Armaroli, N. *Chem. Soc. Rev.* **2009**, *38*, 1690.
- (191) Rarig, R. S.; Lam, R.; Zavalij, P. Y.; Ngala, J. K.; LaDuca, R. L.; Greedan, J. E.; Zubieta, J. *Inorg. Chem.* **2002**, *41*, 2124.
- (192) Pan, L.; Huang, X.; Li, J. *Mater. Res. Soc. Symp.* **2000**, *658*, GG6.17.1.
- (193) Hagrman, D.; Sangregorio, C.; J. O'Connor, C.; Zubieta, J. *J. Chem. Soc., Dalton Trans.* **1998**, 3707.
- (194) Stephens, J.; Cruickshank, D. *Acta Crystallographica Section B: Structural Crystallography and Crystal Chemistry* **1970**, *26*, 222.
- (195) Muniz-Miranda, M.; Pergolese, B.; Bigotto, A. *Phys. Chem. Chem. Phys.*, *12*, 1145.

- (196) Reiher, M.; Brehm, G.; Schneider, S. *J. Phys. Chem. A* **2004**, *108*, 734.
- (197) Dennington, R.; Keith, T.; Millam, J. "GaussView, Version 5"; *Semichem Inc*: Shawnee Mission, Kansas, 2009.
- (198) Briand, L. E.; Hirt, A. M.; Wachs, I. E. *J. Catal.* **2001**, *202*, 268.
- (199) Biradha, K.; Hongo, Y.; Fujita, M. *Angew. Chem.* **2000**, *112*, 4001.
- (200) Wang, Z. Y.; Zha, Z.; Zhang, J. H.; Wu, J. H. *Chin. Chem. Lett.* **2003**, *14*, 13.
- (201) Uddin, J.; Morales, C. M.; Maynard, J. H.; Landis, C. R. *Organometallics* **2006**, *25*, 5566.
- (202) Mitzi, D. *Chem. Mater* **2001**, *13*, 3283.
- (203) Yoon, K. H.; Han, K. S.; Sung, M. M. *Nanoscale Res. Lett.* **2012**, *7*, 71.
- (204) Yoon, B.; O'Patchen, J.; Seghete, D.; Cavanagh, A.; George, S. *Chem. Vap. Deposition* **2009**.
- (205) Brown, I.; Altermatt, D. *Acta Crystallogr., Sect. B: Struct. Sci* **1985**, *41*, 244.